Modelling of Zr-O and U-Zr-O Melts Oxidation and New Crucible Tests

M. S. Veshchunov, J. Stuckert,
A. V. Berdyshev

Institut für Materialforschung
Programm Nukleare Sicherheitsforschung

Forschungszentrum Karlsruhe
in der Helmholtz-Gemeinschaft

Modelling of Zr-O and U-Zr-O melts oxidation and new crucible tests

M. S. Veshchunov*, J. Stuckert, A. V. Berdyshev**

Institut für Materialforschung
Programm Nukleare Sicherheitsforschung

* JRC, Petten
** IBRAE, Moscow

Abstract

This report summarises the results of task WP7.2 of the European COLOSS Project conducted within the 5th Framework Programme on "Nuclear Fission Safety". The objective of this multi-partner task is the development of models regarding the oxidation of U-O-Zr mixtures, in particular:

- Models that can adequately simulate the oxidation of U-O-Zr mixtures and related H_2 production during the core degradation phase of a severe accident.

- Models that can be integrated in SA codes.

In order to modelling of Zr-O and U-Zr-O melts oxidation, it was agreed to use available FZK data on post-test examinations of molten materials oxidation in the CORA and QUENCH bundle tests, as well as new FZK tests (described in the Part I) on ZrO_2 crucible dissolution by molten Zry. These single effect tests were specially designed for the investigation of long-term behaviour during the melt oxidation stage. On this base, a new model (Part II of the report) for oxidation of molten Zr-O and U-Zr-O mixtures in steam was developed, in order to analyse and explain the H_2 peak production during the quenching of degraded rods.

Modellieren der Zr-O und U-Zr-O Schmelzeoxidation und neue Tiegeltests

Zusammenfassung

Dieser Report fasst die Ergebnisse der Aufgabe WP7.2 des europäischen COLOSS-Projektes zusammen, die innerhalb des 5. Rahmenprogramms bearbeitet wurden. Das Ziel dieser Multipartneraufgabe ist die Entwicklung der Modelle für die Oxidation der U-O-Zr Mischungen, insbesondere:

- Modelle, die die Oxidation der U-O-Zr Mischungen und der in Verbindung stehenden H_2-Freisetzung während der Kernschmelzphase eines schweren Reaktorstörfalles ausreichend simulieren können.

- Modelle, die in Störfallprogramme integriert werden können.

Das Ziel der Modellierung der Oxidation Zr-O- und U-Zr-O-Schmelzen war es, vorhandene FZK-Daten aus den Nachuntersuchungen der Schmelze, die in den CORA- und QUENCH-Bündelexperimenten aufgetreten ist, zu verwenden. Ferner sollten die Ergebnisse der neuen FZK-Versuche zur Auflösung von ZrO_2-Tiegel durch flüssiges Zircaloy (beschrieben im Teil I) modelliert werden. Diese Einzelversuche wurden besonders konzipiert für die Untersuchung des langfristigen Verhaltens während des Schmelzoxidationsstadiums. Auf dieser Basis wurde ein neues Modell (Teil II des Berichtes) der Dampfoxidation von flüssigen Zr-O- und U-Zr-O-Mischungen entwickelt, um die intensive Wasserstofffreisetzung während des Abschreckens beschädigter Stäbe zu analysieren und zu erklären.

Content

List of Tables

List of Figures

4

6

Part I. ZrO$_2$ Dissolution by Molten Zircaloy. Results of the Crucible Tests

J. Stuckert

1. Experimental objectives

Isothermal heating experiments at 2100 °C and 2200 °C and with annealing times up to 290 min were performed to study the dissolution of Y$_2$O$_3$-stabilised zirconia crucibles by molten Zircaloy-4 (Zry). The experiments should simulate the dissolution of steam-oxidised cladding surface layers by the molten Zry located between the ZrO$_2$ layer and the fuel pellet during a high-temperature transient of a severe fuel damage accident.

2. Materials

The tests were performed with crucibles of Y$_2$O$_3$-stabilised zirconia containing charges of as-received (oxygen-free) Zry-4 (Table 1). The crucibles were identical to those used in the AECL (Canada) tests [1]: the crucibles contain yttria and wax binder contents of 7.9 wt% and 4.5 wt%, respectively. Table 1 includes also the crucible parameters for the tests FA1-FA3, which were performed within the former FZK tests series [2].

The tests were performed with two different values of surface to volume (*S/V*) ratio (V - the melt volume, S - the ZrO$_2$ surface in contact with the melt). The initial weight of the Zry charge (cylindrical pellet of 6.2 mm diameter) was ~1.3 g for the test with S/V=770 m^{-1} and ~1.9 g for the test with S/V=720 m^{-1}.

3. Test procedure

The specimens were inductively heated by means of a tungsten susceptor in the LAVA facility (Fig. I-1). In each test the furnace was evacuated several times and backfilled with high–purity argon. Then the specimen was slowly heated up (~ 1 K/s) to about 1650°C and kept at this temperature for about 3 min for thermal equilibrium. The specimen was then further heated to the desired test temperature with a heating rate of about 15 K/s. After the pre-determined annealing time the high–frequency generator was switched off and the specimen was rapidly cooled down.

The crucible temperatures were continuously recorded by a monochrome pyrometer and a W/Re thermocouple. The pyrometer, focused on the bottom of the tungsten susceptor through a quartz window in the furnace bottom, was also used as feedback device to a high frequency generator. As value for the tungsten emissivity ε=0.4 was used. The sheathed W/Re thermocouple was used for monitoring only. The distance between thermocouple and the upper edge of the crucible was about 10 mm. The thermocouple mainly heats because of radiation from the susceptor sidewall, therefore the thermocouple reading corresponds to the temperature of the outer side of the crucible wall.

The overpressure in the furnace was measured with a pressure transducer. The outputs of the temperature and pressure transducers as well as the generator power indication signal were fed into the computer-based data acquisition system DATASCAN and recorded at 0.3 s intervals. Plots of a corresponding measurement are shown in Figs. I-2 - I-13. The test conditions are summarised in Table 2. One can see from this table and the corresponding plots, that the temperature distribution in the furnace was inhomogeneous: the outer surface of the sidewall of the crucible

was, for most tests, hotter than the crucible bottom. The inhomogeneity is due to the temperature gradient between the crucible wall and the melt loosing heat by intensive heat radiation from the melt surface.

4. Test results

The post-test crucibles were completely intact. A typical view of the crucible is shown in Fig. I-14. One can observe the thin metallic coating on the outer surface of the crucible sidewall. The detailed SEM-EDX investigation (Figs. I-15 – I-16) shows the presence of many tungsten particles on the crucible surface - the result of the susceptor sublimation with the subsequent tungsten adsorption on the crucible surface.

A post-test metallography was performed. The typical zones across the crucible cross-section are shown in Fig. I-17. There are three characteristic zones: (a) the crucible wall with the α-Zr(O) precipitates on the grain boundaries, (b) the corrosion transition layer ZrO_{2-x} and (c) the refrozen melt. The α-Zr(O) precipitates along the grain boundaries indicates that oxygen diffuses to the melt mainly along the grain boundaries of ZrO_2. The transition layer between the melt and the wall crucible is formed after the cessation of the short-term wall dissolution phase and is the result of the boundary melt corrosion by the oxygen diffused from the crucible wall.

Figs. I-18 – I-20 show the cross-sections of all crucibles used with the measured values of the transition layer thickness. The tests can be divided into three characteristic groups: tests at 2100°C, tests at 2200°C with S/V=770 m^{-1} and tests at 2200°C with S/V=720 m^{-1}. The results of the AECL test series was added to the Fig. I-20 (2200°C with S/V=720 m^{-1}) for a complete illustration of the process evolution. The group of tests at 2200°C with S/V=720 m^{-1} includes the tests with a long time of annealing. The test FA10 of this group has a maximum test duration (with the isothermal period of 290 min.) and is characterised by the completely dissolved corrosion layer. Some cross-sections show the presence of relatively large voids in the melt (FA2, AECL21, FA10). These voids can be interpreted as gas bubbles that formed at temperature with the oxygen not dissolved in the melt.

The quantitative image analysis of the melt region (described in [2]) was performed in order to determine the oxygen content in the melt. The corresponding results of this analysis as well as other post-test measurement results are summarised in Table 3. The individual measurement results with the corresponding photographs of the melt structure are shown in Figs. I-21 – I-23. The order of photographs in these figures corresponds to the order of the cross-sections given in Figs. I-18 – I-20.

The comparison of the calculated oxygen content in the melt with the points of the liquidus line (Fig. I-24) shows that the test data of all performed tests lie at the annealing temperatures in the two-phase region of the Zr-O phase diagram (melt with ZrO_{2-x} precipitates). With the oxygen gradient between solid state and melt the oxygen content in the melt increases continuously and can reach the concentration, that corresponds to a total melt oxidation.

Conclusions

- Twelve experiments on the dissolution of yttria-stabilised zirconia crucibles by molten Zircaloy have been performed

- Three stages of the process were observed: the short-term phase of the crucible wall dissolution, the phase of the corrosion layer formation at the boundary between the crucible wall and the melt, and the long-term phase of the repeated wall dissolution

- Two oxygen sources for the melt oxidation can be distinguished: the oxygen from the dissolved part of the crucible in the first dissolution phase and the oxygen continuously transported to the melt by diffusion from the surface of the grains of the ZrO_2 crucible matrix

- The kinetics of the process was affected by an inhomogeneous and uncontrollable temperature distribution in the system, i.e. the crucible walls were hotter than the crucible bottom and the melt

- For all performed tests the oxygen content in the melt at the annealing temperatures used corresponds to the two-phase region (liquid + ZrO_{2-x} precipitates) of the Zr-O phase diagram

- Some tests show the formation of gas bubbles in the melt. The formation of these bubbles was interpreted by the release of the oxygen, which could not be dissolved in the melt

Acknowledgements

References

1. P.J. Hayward and I. M. George, "Dissolution of ZrO_2 in Molten Zry-4", J.Nucl.Mater., 265 (1999) 69

2. P. Hofmann, J. Stuckert, A. Miassoedov, M. S. Veshchunov, A. V. Berdyshev, A. V. Boldyrev. "ZrO_2 Dissolution by Molten Zircaloy and Cladding Oxide Shell Failure. New Experimental Results and Modelling", FZKA 6383, Forschungszentrum Karlsruhe, 1999

Test No.	Crucible						Zry-charge		Mass ratio	S/V
	O.D. mm	I.D. mm	Height mm	Depth mm	Weight g	Density g/cm³	Zry weight, g	Init. melt level, mm		
FA1	13.70	6.45	16.65	13.3	11.839	5.85	1.301	6.82	9.1	767
FA2	13.80	6.40	16.50	13.4	11.737	5.75	1.339	7.18	8.8	764
FA3	13.80	6.40	16.35	13.3	11.737	5.81	1.339	7.18	8.8	764
FA4	13.80	6.40	16.38	13.4	11.678	5.78	1.293	6.93	9.0	769
FA5	13.80	6.40	16.38	13.3	11.601	5.74	1.277	6.85	9.1	771
FA6	13.72	6.40	16.38	13.3	11.687	5.86	1.280	6.86	9.1	771
FA7	13.77	6.40	16.38	13.3	11.719	5.83	1.284	6.88	9.1	770
FA8	13.72	6.42	16.48	14.5	11.496	5.84	1.283	6.83	9.0	769
FA9	13.80	6.40	16.56	13.5	11.871	5.81	1.282	6.87	9.3	770
FA 10	13.82	6.42	16.22	13.3	11.591	5.79	1.967	10.48	5.9	718
FA 11	13.80	6.42	16.38	13.3	11.711	5.80	1.947	10.37	6.0	719
FA 12	13.80	6.42	16.43	13.4	11.703	5.78	1.919	10.22	6.1	721

Table 1. Pre-test material dimensions and weights

Test No.	Pyrometer temperature °C	TC temperature °C	Initial Ar overpressure mbar (at 20 °C)	Melt duration s	Isothermal time s
FA1	2100	2100		1820	1600
FA2	2100	2100		620	560
FA3	2200	2100		1222	1137
Fa4	2200	failure	524	1505	1468
Fa5	2200	2270	515	614	555
Fa6	2200	2290	507	1514	1445
Fa7	2100	2270	505	1812	1768
Fa8	2100	2100	520	903	873
Fa9	2200	2290	507	910	857
Fa10	2200	2350	294	17411	17346
Fa11	2200	failure	520	4510	4435
Fa12	2200	2200	320	12007	11916

Table 2. Test conditions

Test No.	Pyr °C	TC °C	Time min	Probe weight change mg	Crucible wall disso- lution, mm	Transition oxide layer mm	Image analysis of the melt					
							Ceramic %	Metall %	Pores %	Ceramic without pores, %	Oxygen wt %	Oxygen at %
FA2	2100	2100	10		0.22	0.97	38.9	49.5	11.6	44.0	14.5	49.1
FA8	2100	2100	15	-1	0.17	1.49	55.3	34.9	9.8	61.3	17.7	55.1
FA7	2100	2270	30	2	0.37	2.00	84.4	13.0	2.6	86.7	22.4	62.2
FA1	2100	2100	33		0.04	1.84	62.9	28.0	8.0	69.2	19.2	57.5
FA5	2200	2270	10	-4	0.32	0.99	70.2	21.1	8.7	76.9	20.6	58.3
FA9	2200	2290	15	-4	0.30	1.26	81.2	15.8	3.0	83.7	21.9	61.5
FA3	2200	2150	20		0.22	1.50	63.4	19.8	16.8	76.2	20.5	59.5
FA6	2200	2290	25	-2	0.24	1.01	86.8	5.7	7.5	93.8	23.7	63.4
FA4	2200	?	25	17	0.34	1.12	91.5	4.2	4.3	95.6	24.1	63.5
FA11	2200	?	75		0	1.69	81.0	11.2	7.8	87.9	22.6	62.5
FA12	2200	2200	200	-6	0.06	1.39	69.6	8.0	22.4	89.7	23.0	63.0
FA10	2200	2350	290	-37	0.71	0	85.9	2.1	12.0	97.6	24.4	63.1

FA1 - FA9:   S/V ~ 770 m^{-1}
FA10 - FA12: S/V ~ 720 m^{-1}

Table 3. Results of the post-test analyses

ZrO$_2$ fiber board insulation

quartz tube

Al$_2$O$_3$ heat shielding

water cooled induction coil (f = 700 kHz)

32 mm

Zry-4 melt specimen

ZrO$_2$ crucible

Tungsten susceptor, wall thickness 0.9 mm, [depth of skin layer(700 kHz, 2300 °C) = 0.5 mm]

TC

163 mm

77 mm

55 mm

40 mm

39 mm

26 mm

16.4 mm

3.2 mm

0 mm

-12 mm

monochrome infrared pyrometer ε=0.4

Computer

Analog/digital converter

T$_{max}$ = 2400 °C; p$_{max}$ = 3 bar; argon

Fig. I-1. Schematic of the high-temperature melting LAVA apparatus
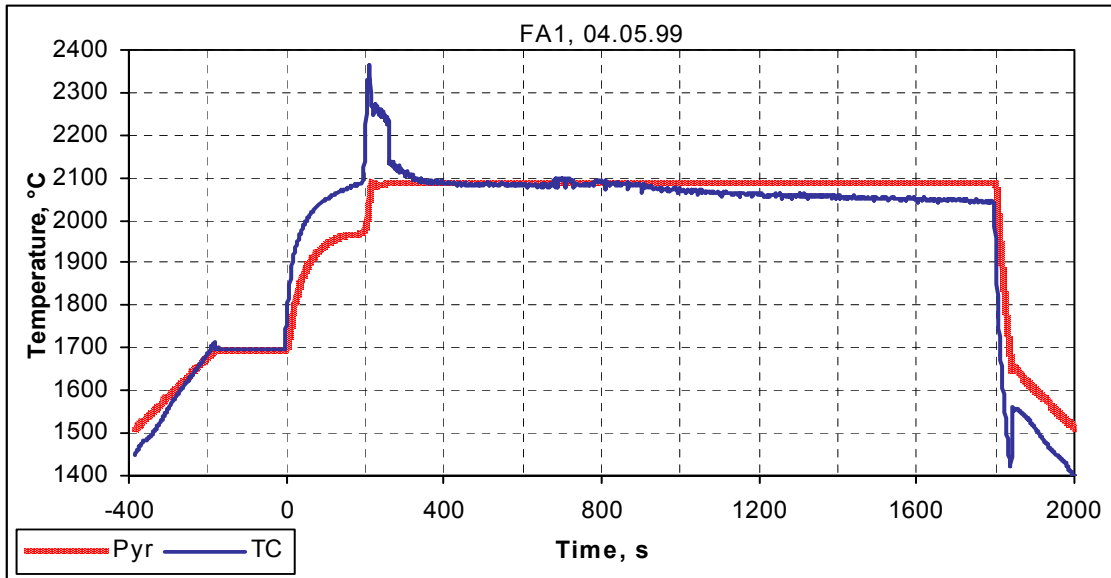
Fig. I-2. Temperature vs. time of test FA1
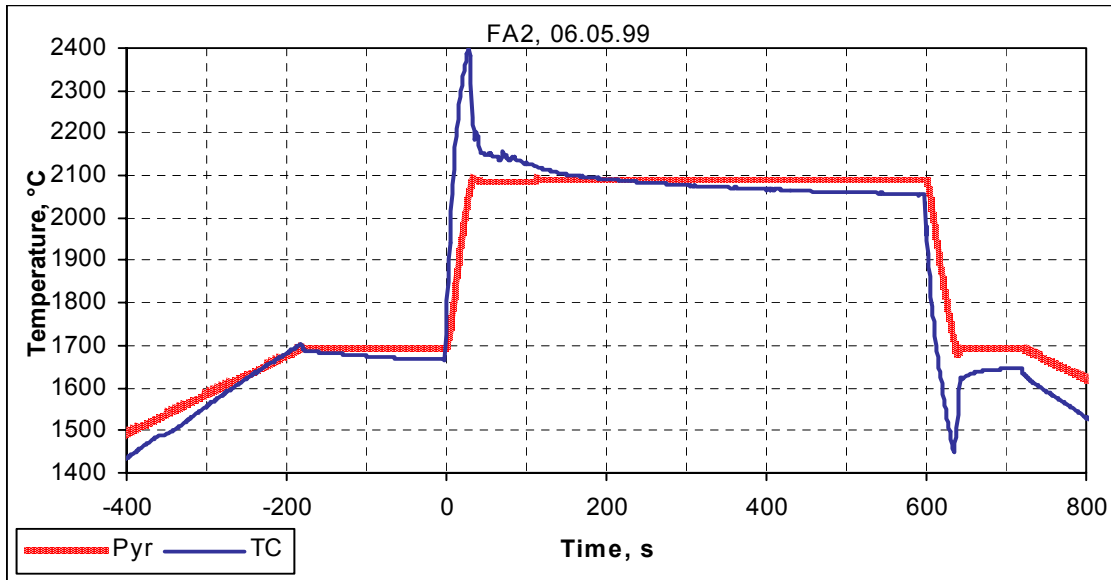
Fig. I-3. Temperature vs. time of test FA2
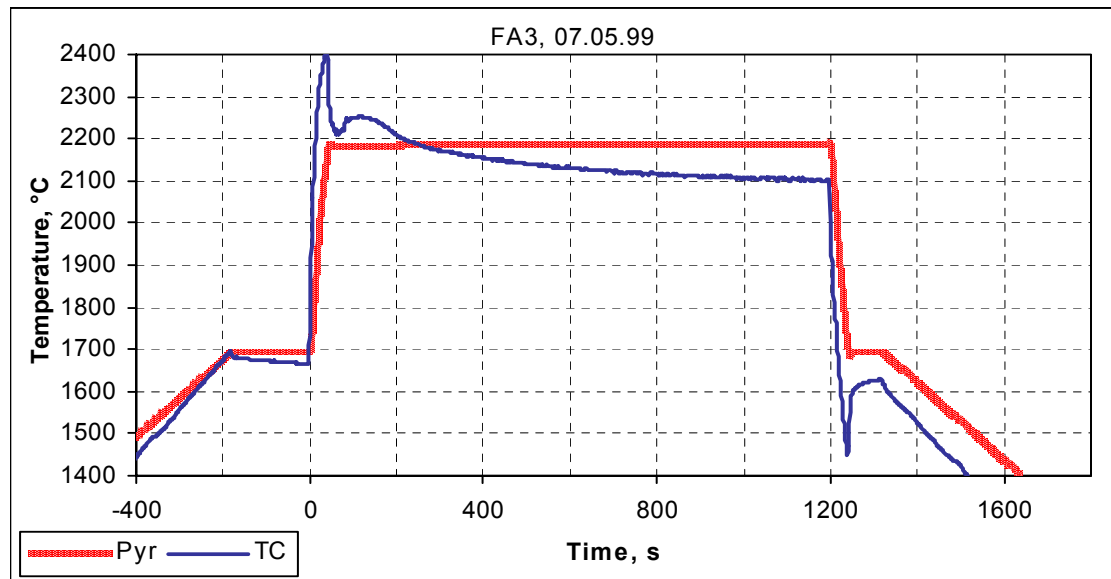
Fig. I-4: Temperature vs. time of test FA3
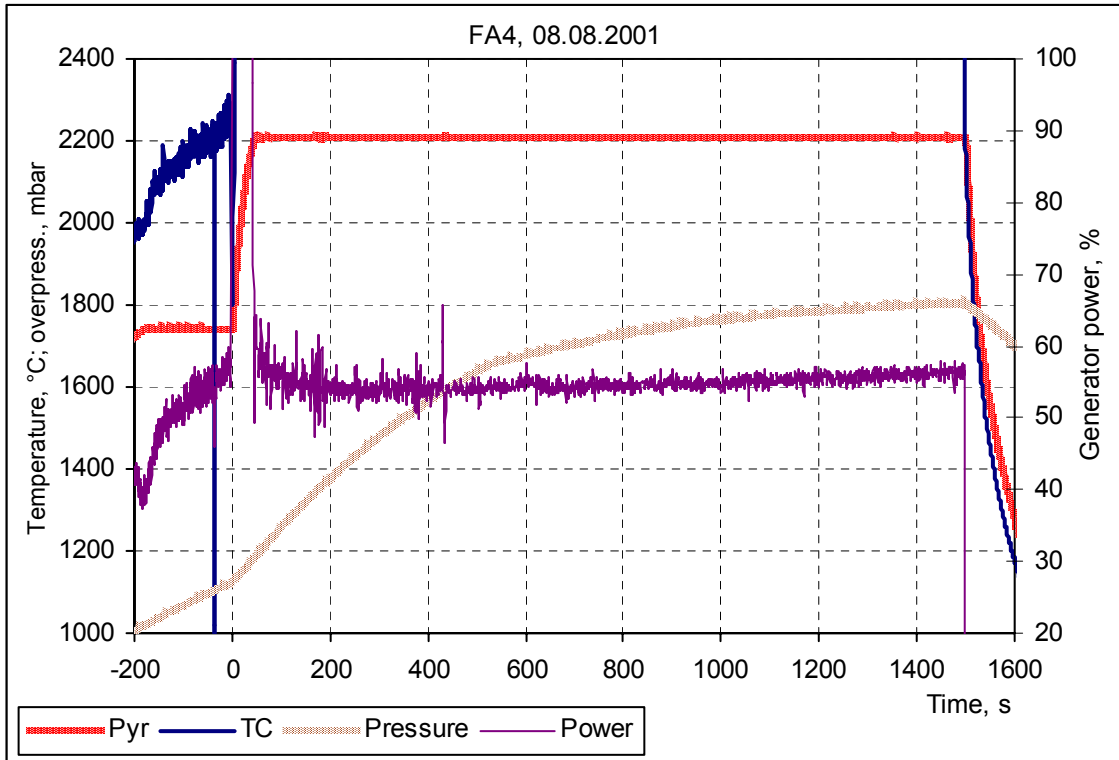
Fig. I-5: Data of test FA4
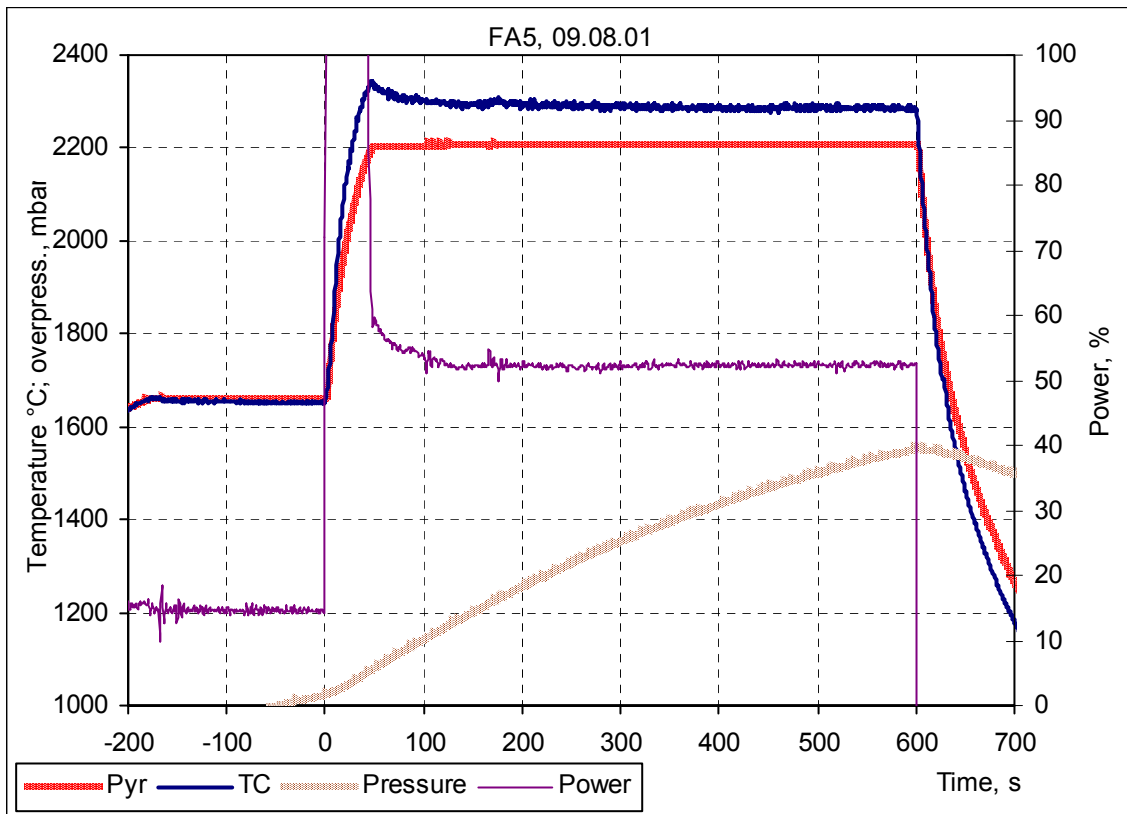
Fig. I-6: Data of test FA5

14
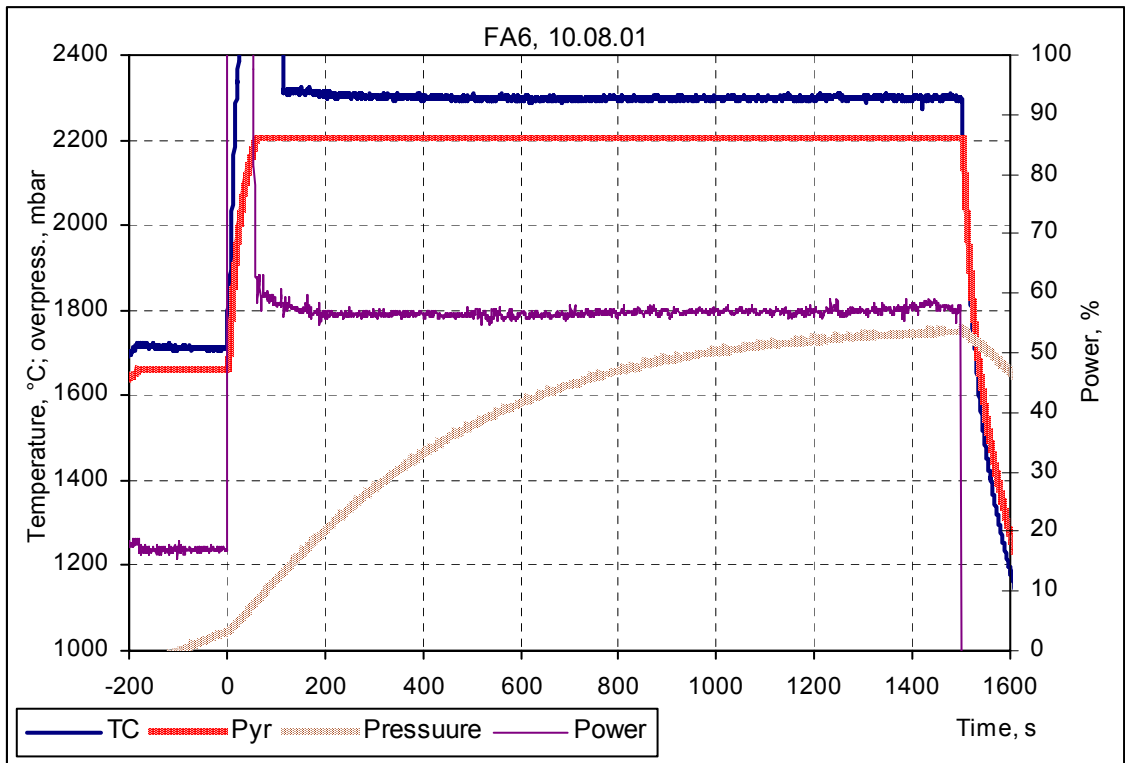
Fig. I-7: Data of test FA6
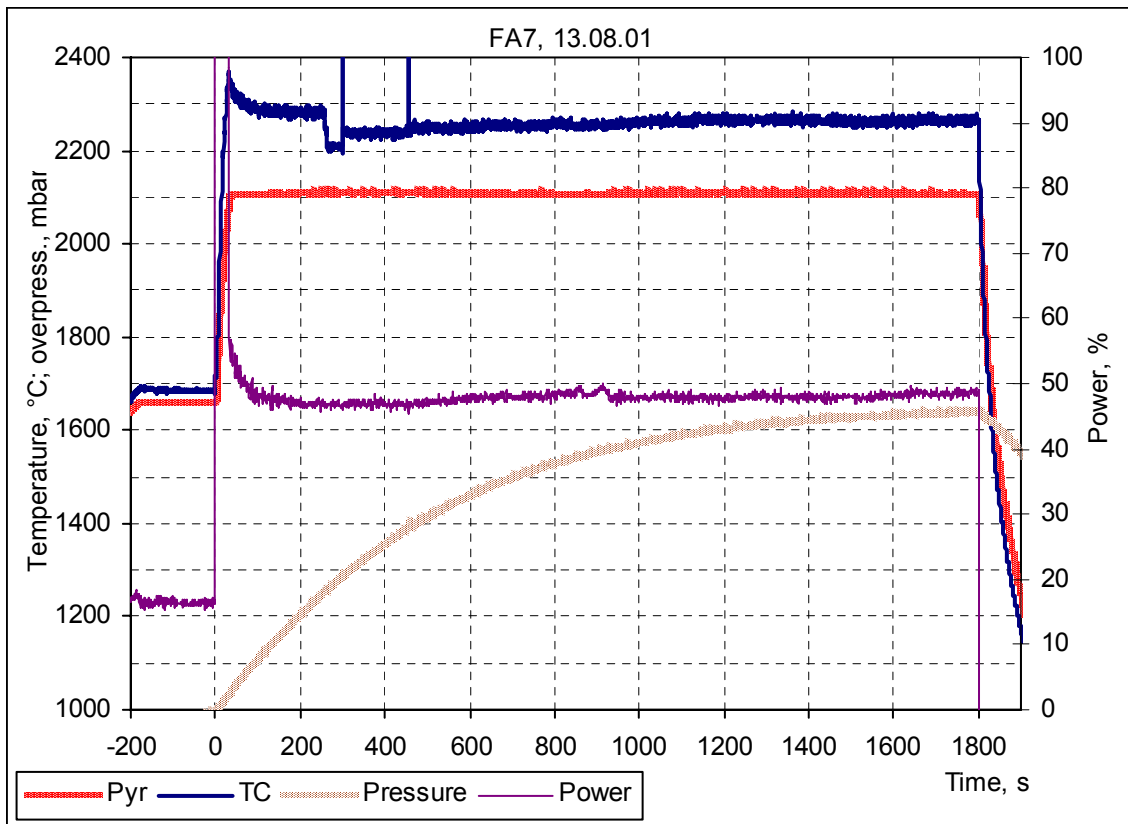
Fig. I-8: Data of test FA7
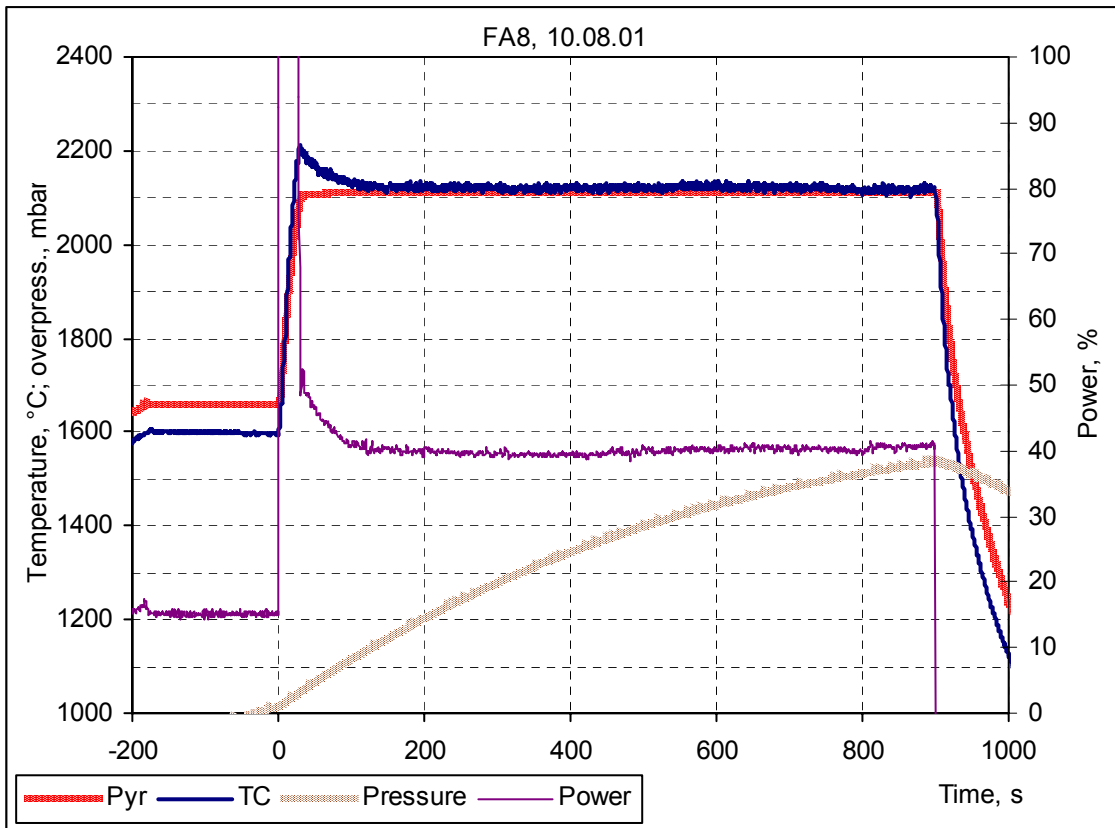
Fig. I-9: Data of test FA8
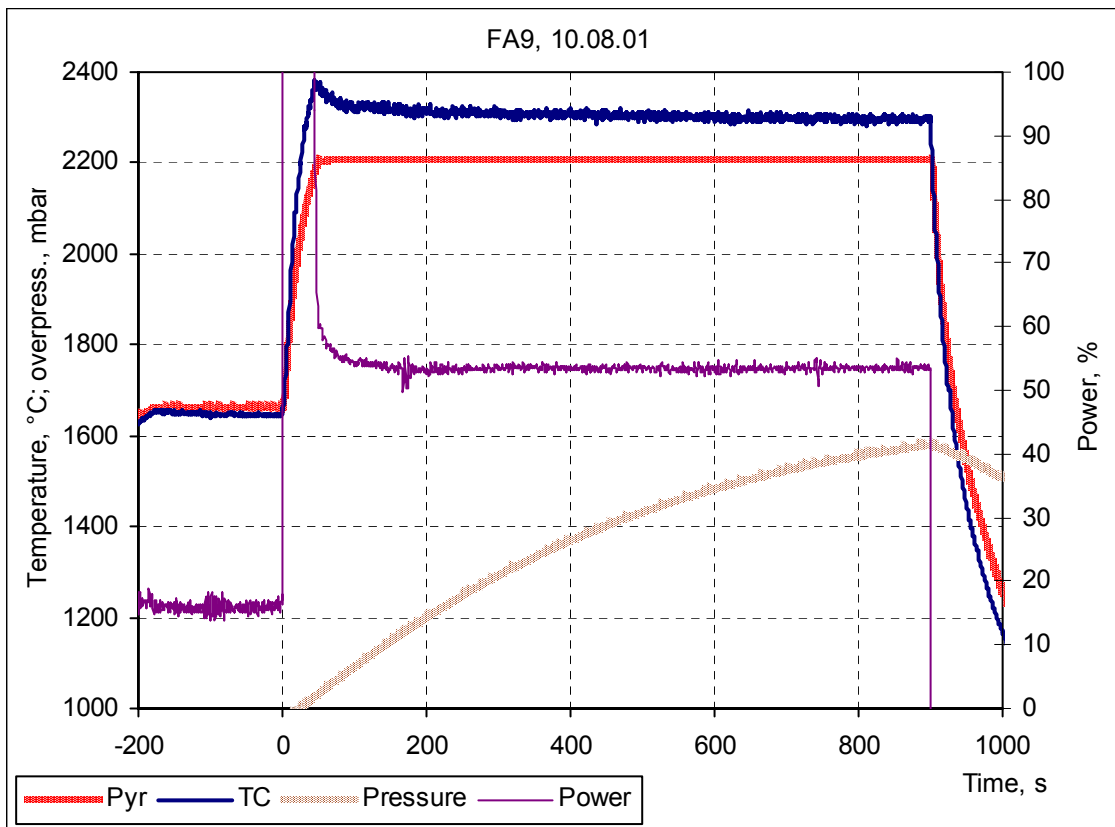
Fig. I-10: Data of test FA9
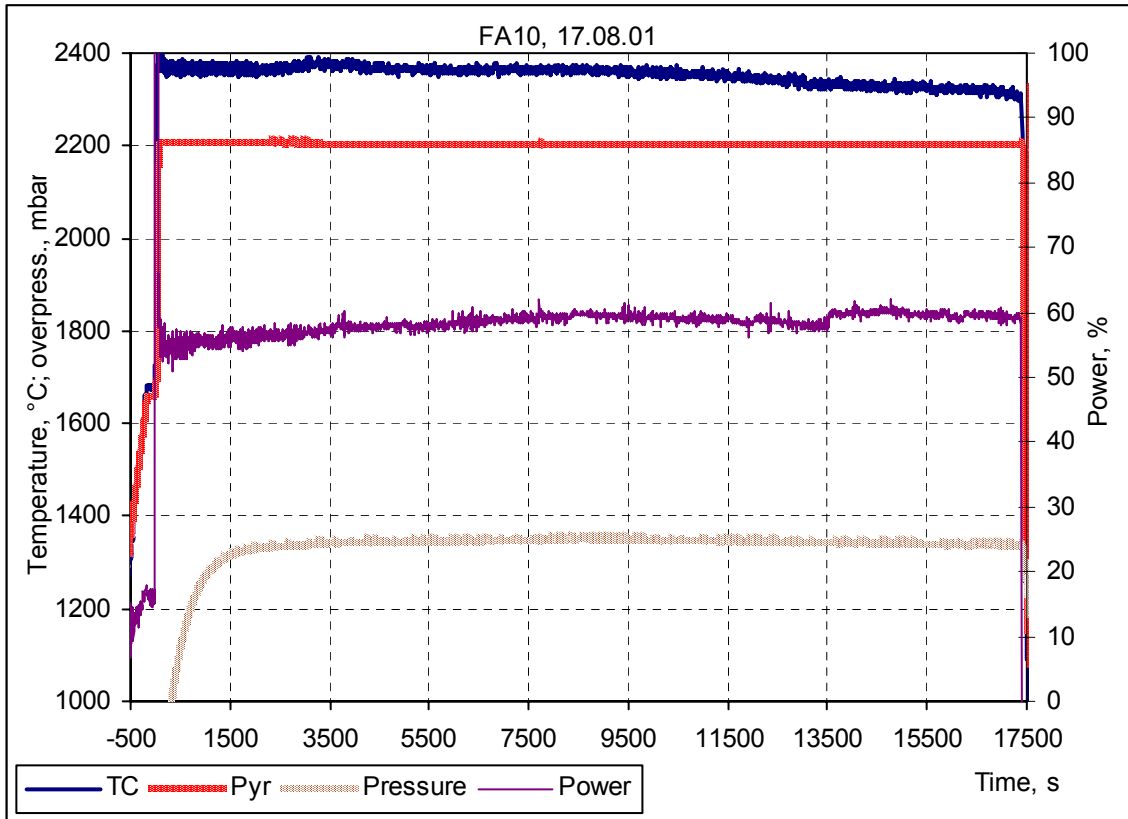
Fig. I-11: Data of test FA10
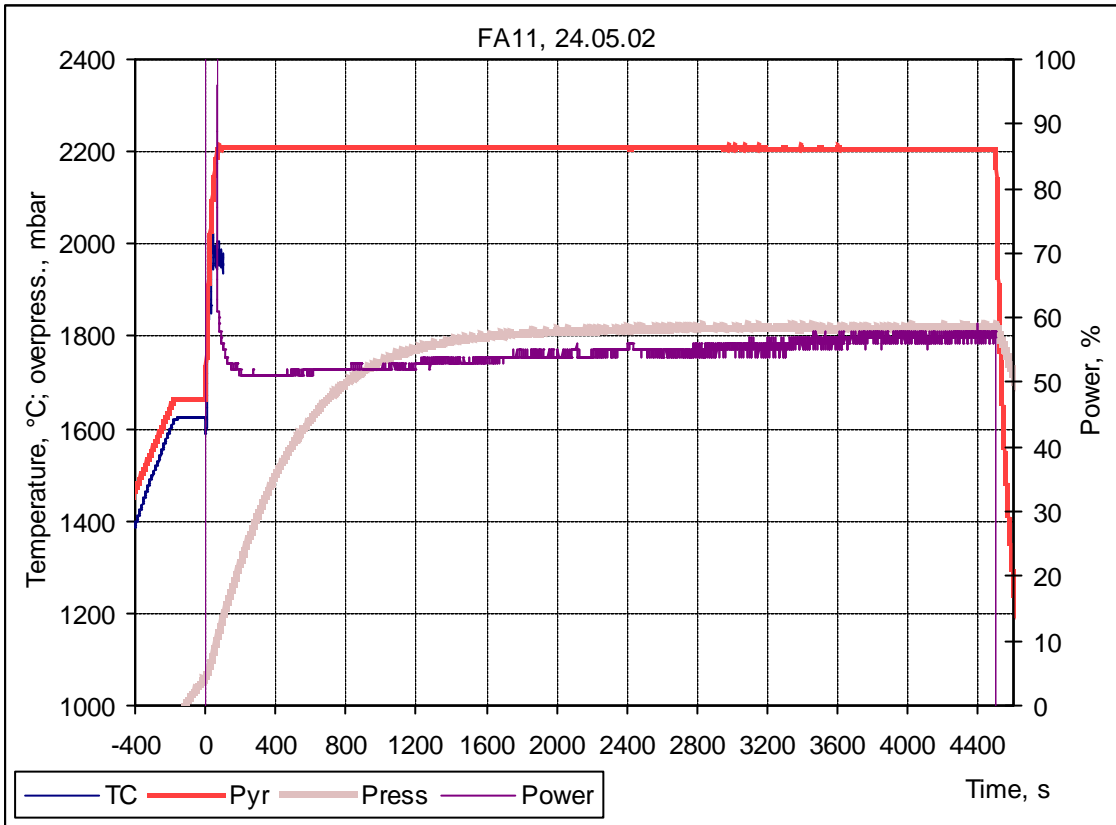
Fig. I-12: Data of test FA11

Fig. I-13: Data of test FA12

metallic coating

Zry-pearl (occurred only in test FA12, analysed by EDX)

Side view

Top view
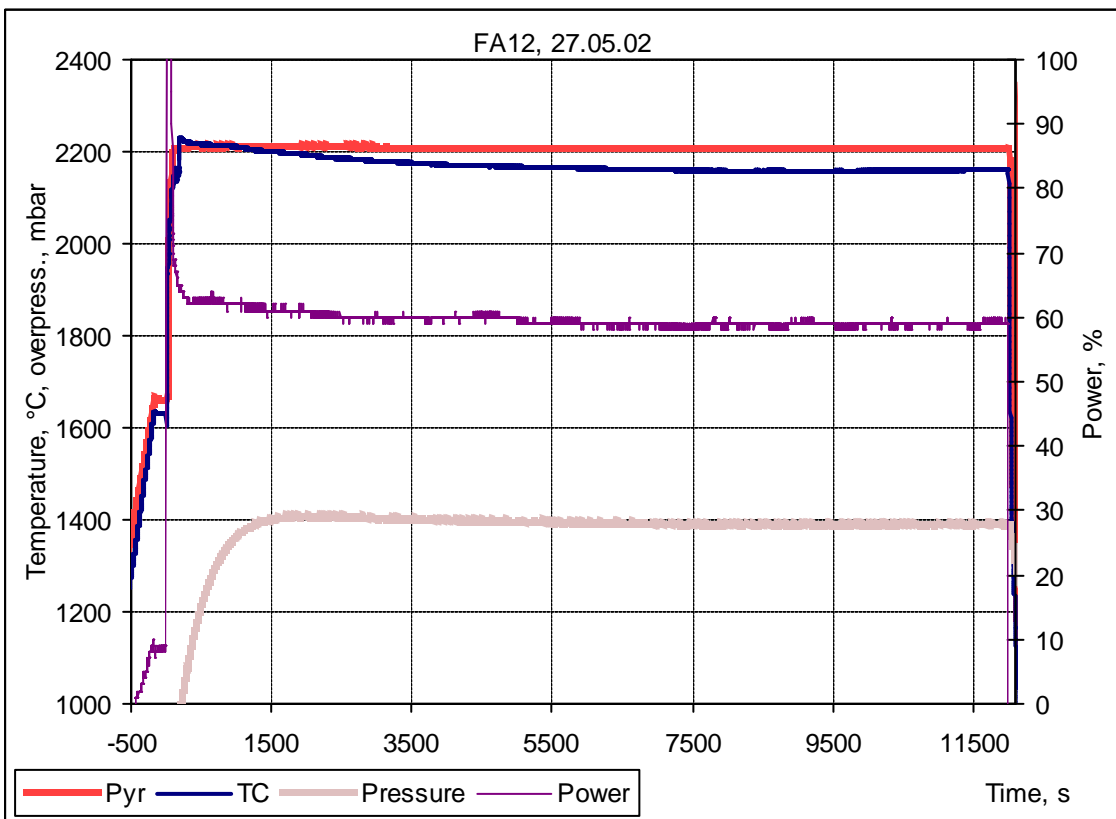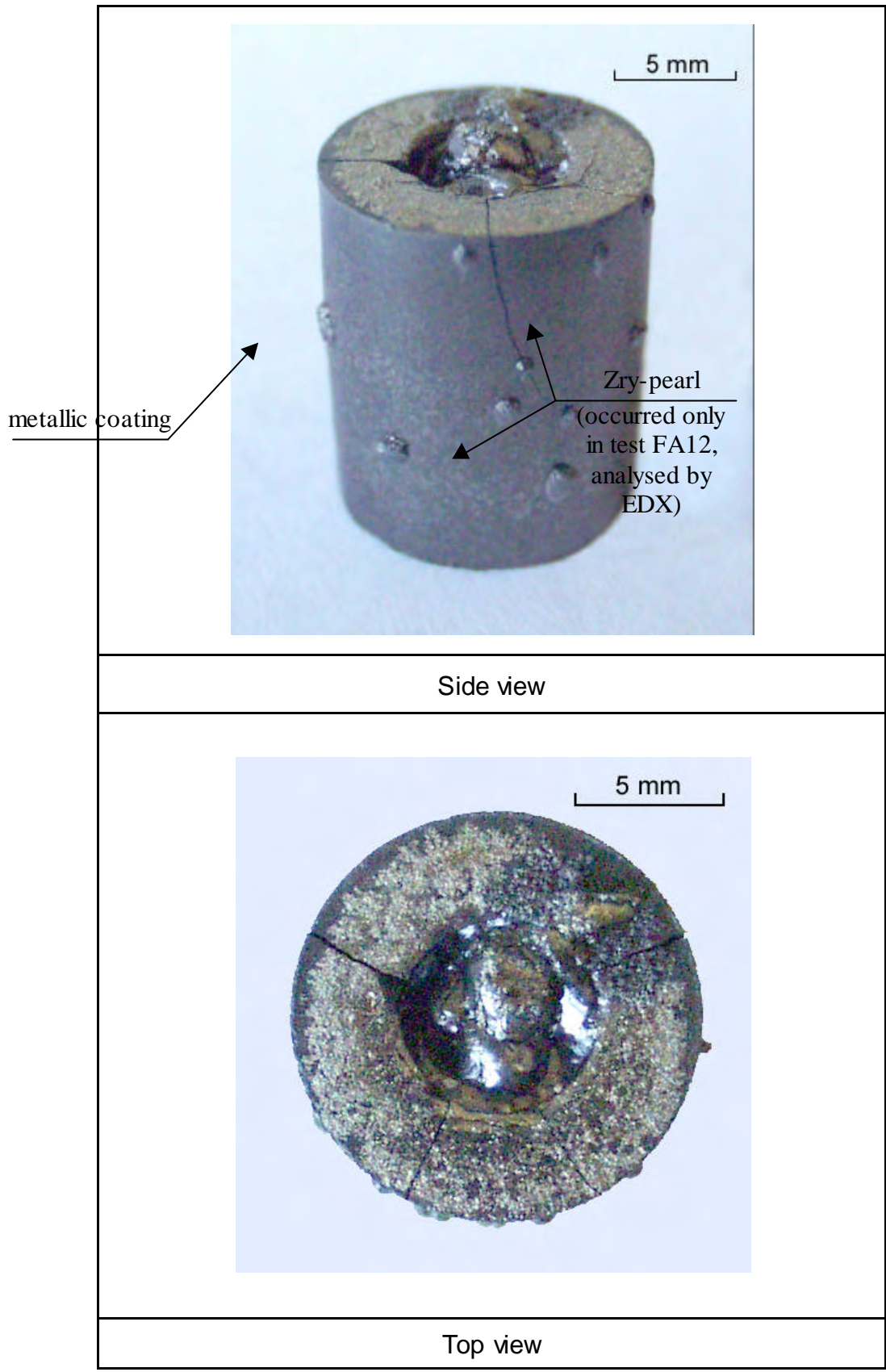
Fig. I-14: View of the FA12 sample after the test at 2200 °C during 200 min
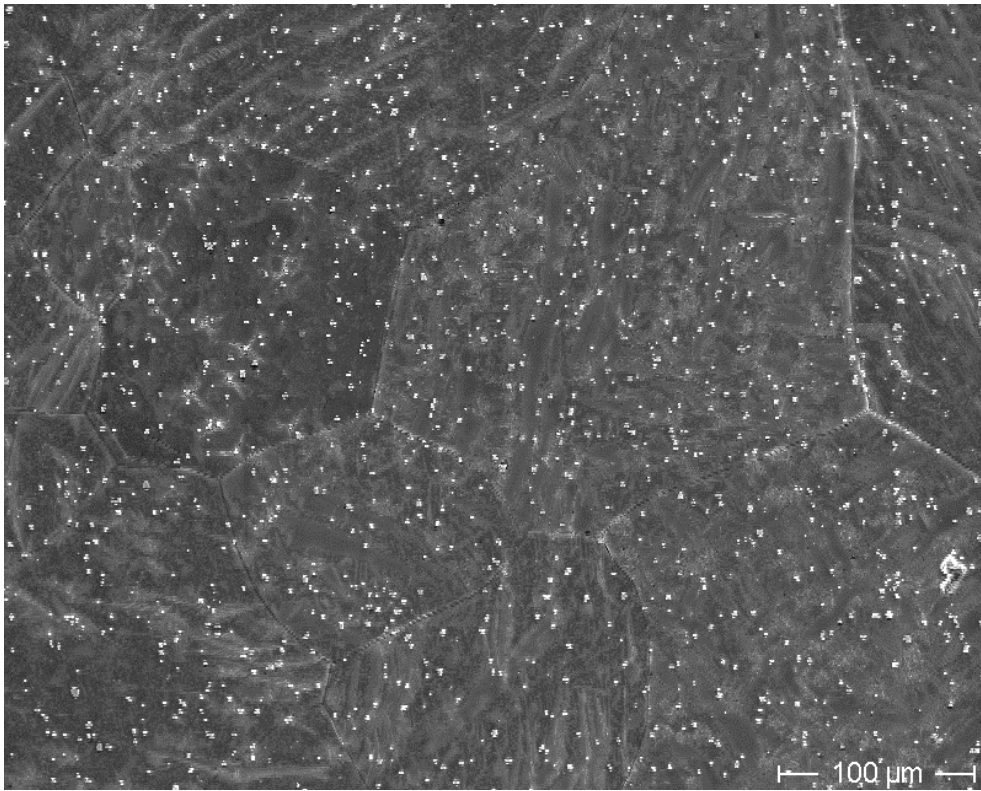
Outer surface of crucible

W-particle (EDX)
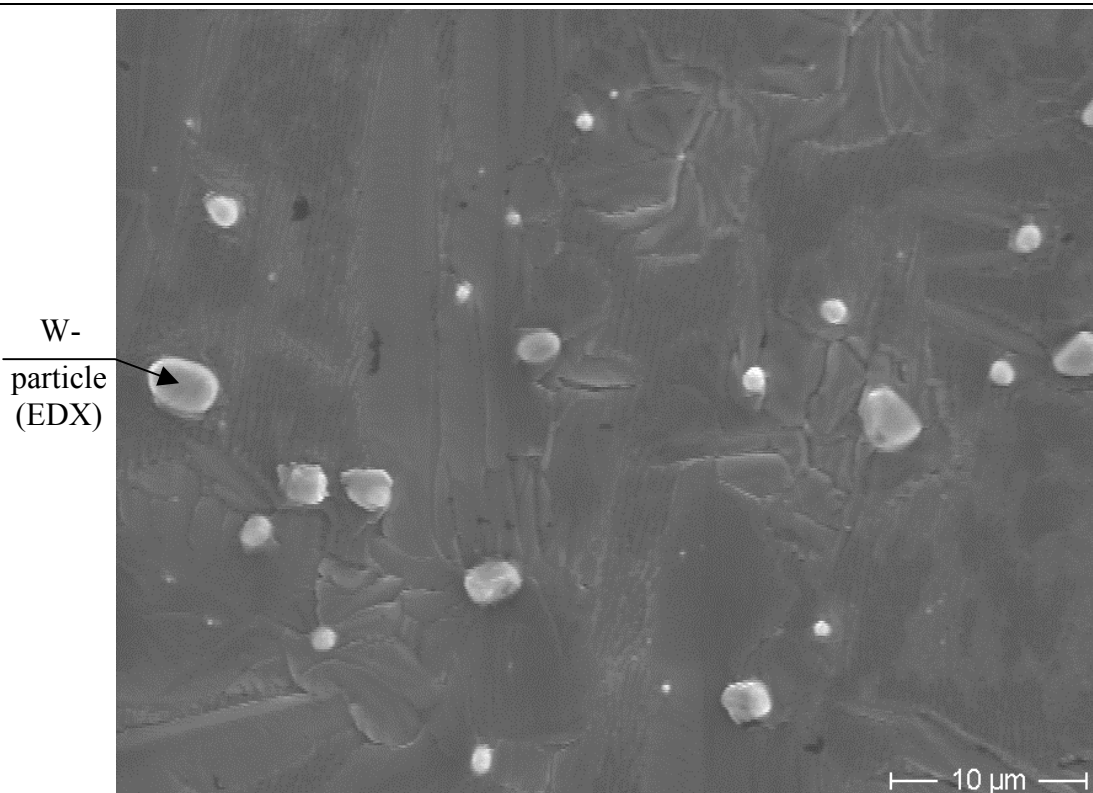
Tungsten particles are present on the outer surfaces of all crucibles

Fig. I-15: Electronic microscope photos of the outer surface of FA4 probe after the test

20

Area EDX-scan of the outer surface of the crucible

Point EDX-scan of the metallic particle on the outer surface
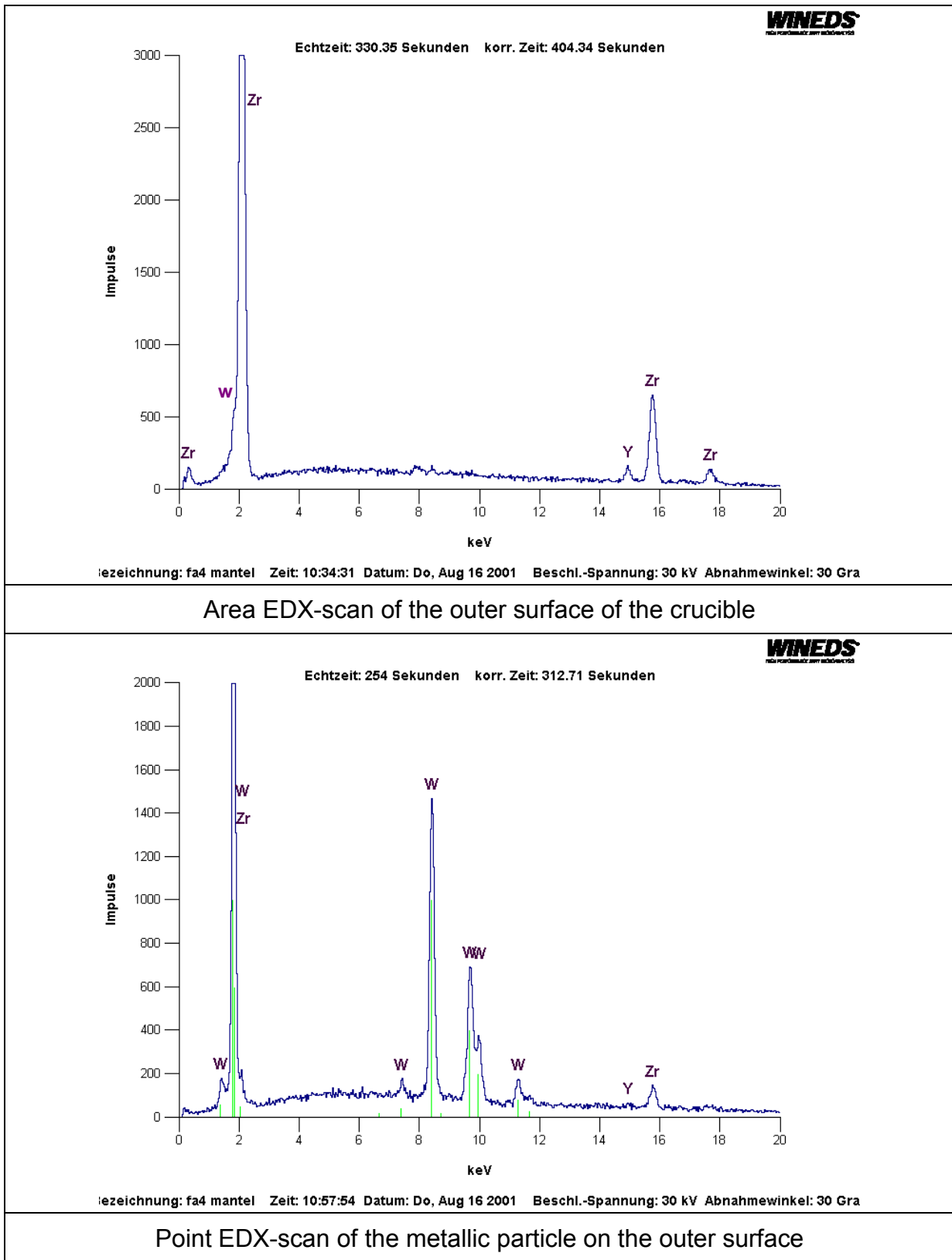
Fig. I-16: EDX analysis of the outer surface of the FA4 crucible after the test
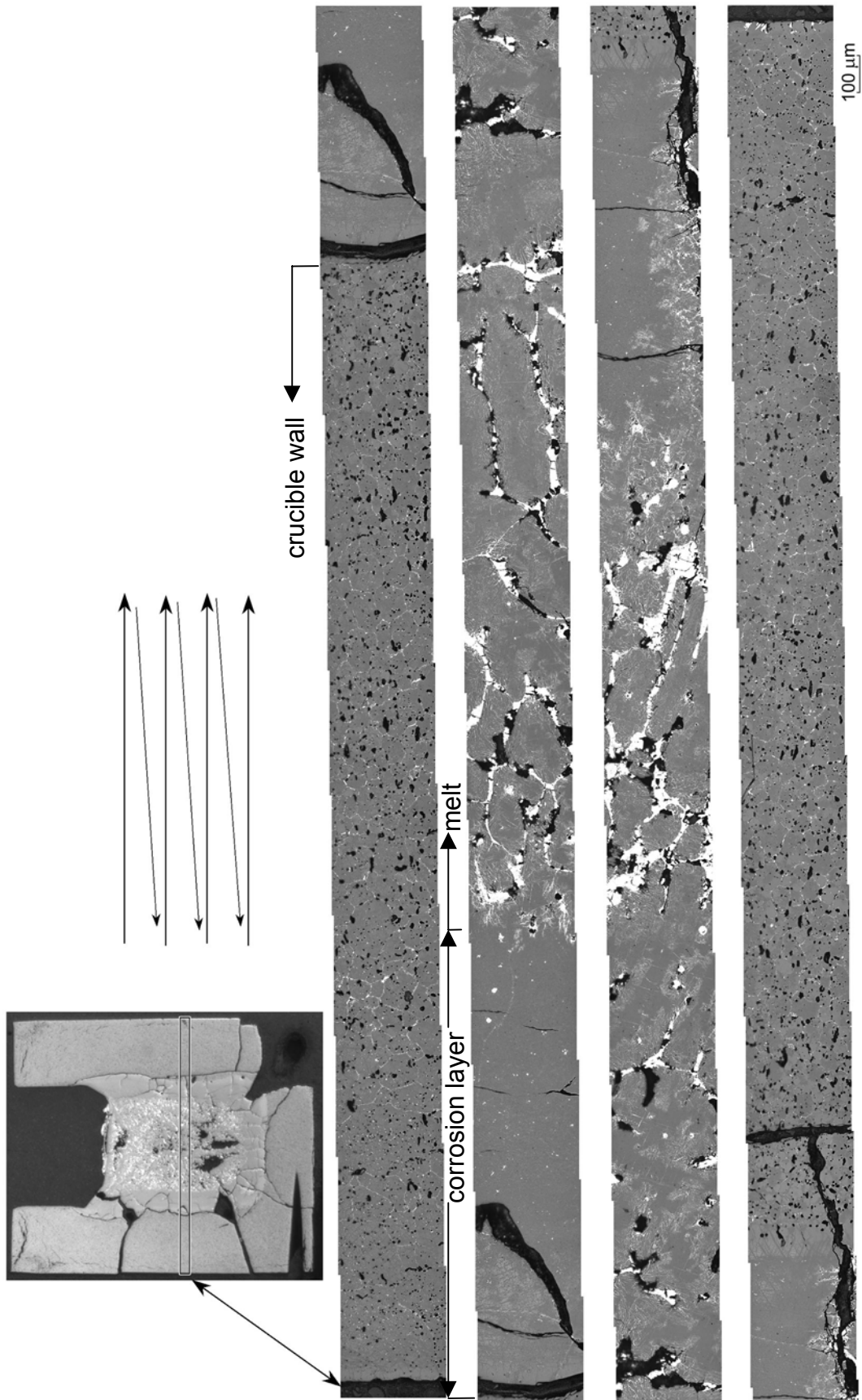
Fig. I-17: Optical scanning of the FA4 cross-section (2200°C, 25 min.)
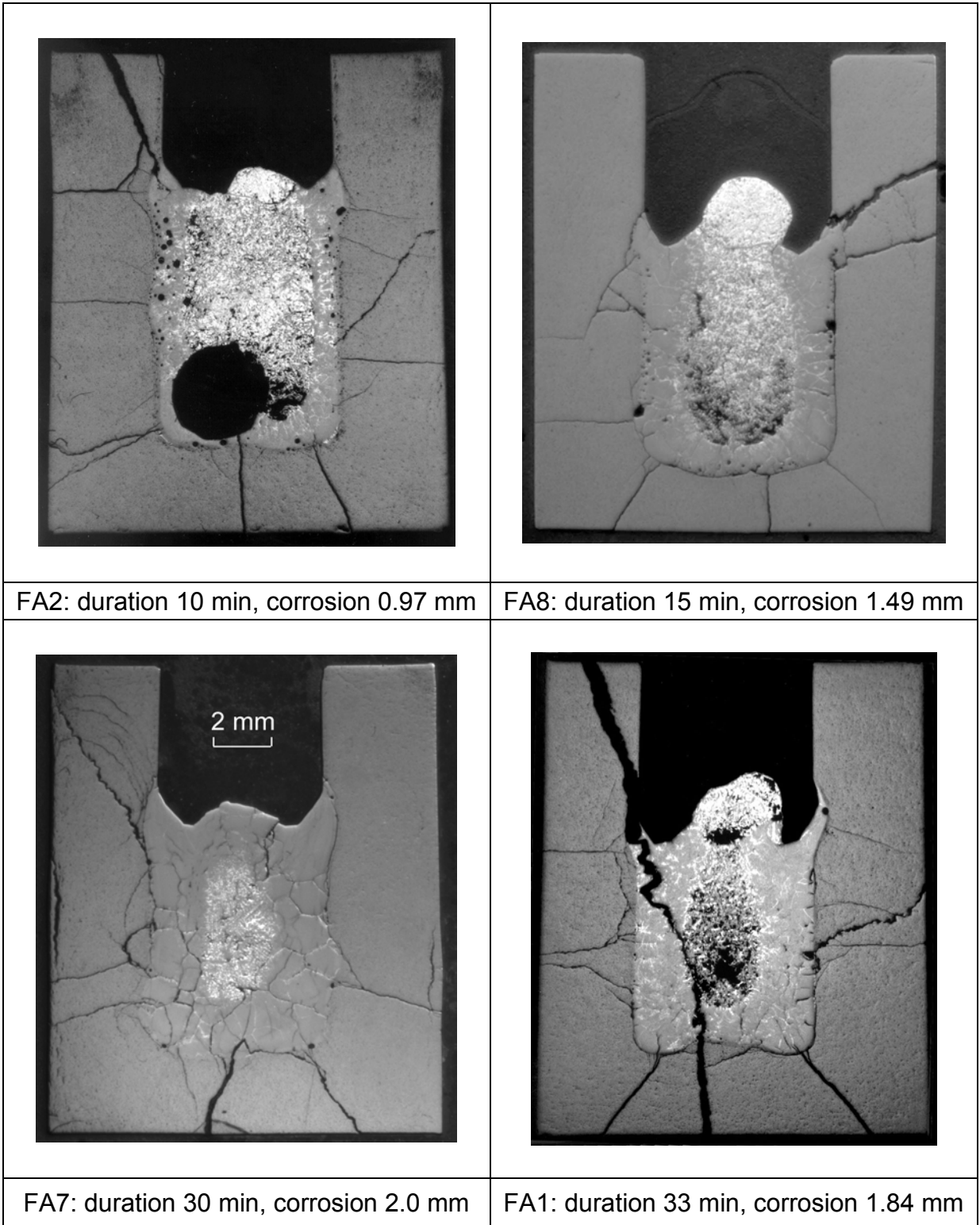
Fig. I-18: Crucible cross-sections after the dissolution tests at ~2100°C (crucible bottom temperature). Interaction surface to initial melt volume ratio: S/V~770 m^{-1}

FA5: duration 10 min, corrosion 0.99 mm	FA9: duration 15 min, corrosion 1.26 mm

FA3: duration 20 min, corrosion 1.5 mm

FA6: duration 25 min, corrosion 1.01 mm	FA4: duration 25 min, corrosion 1.12 mm
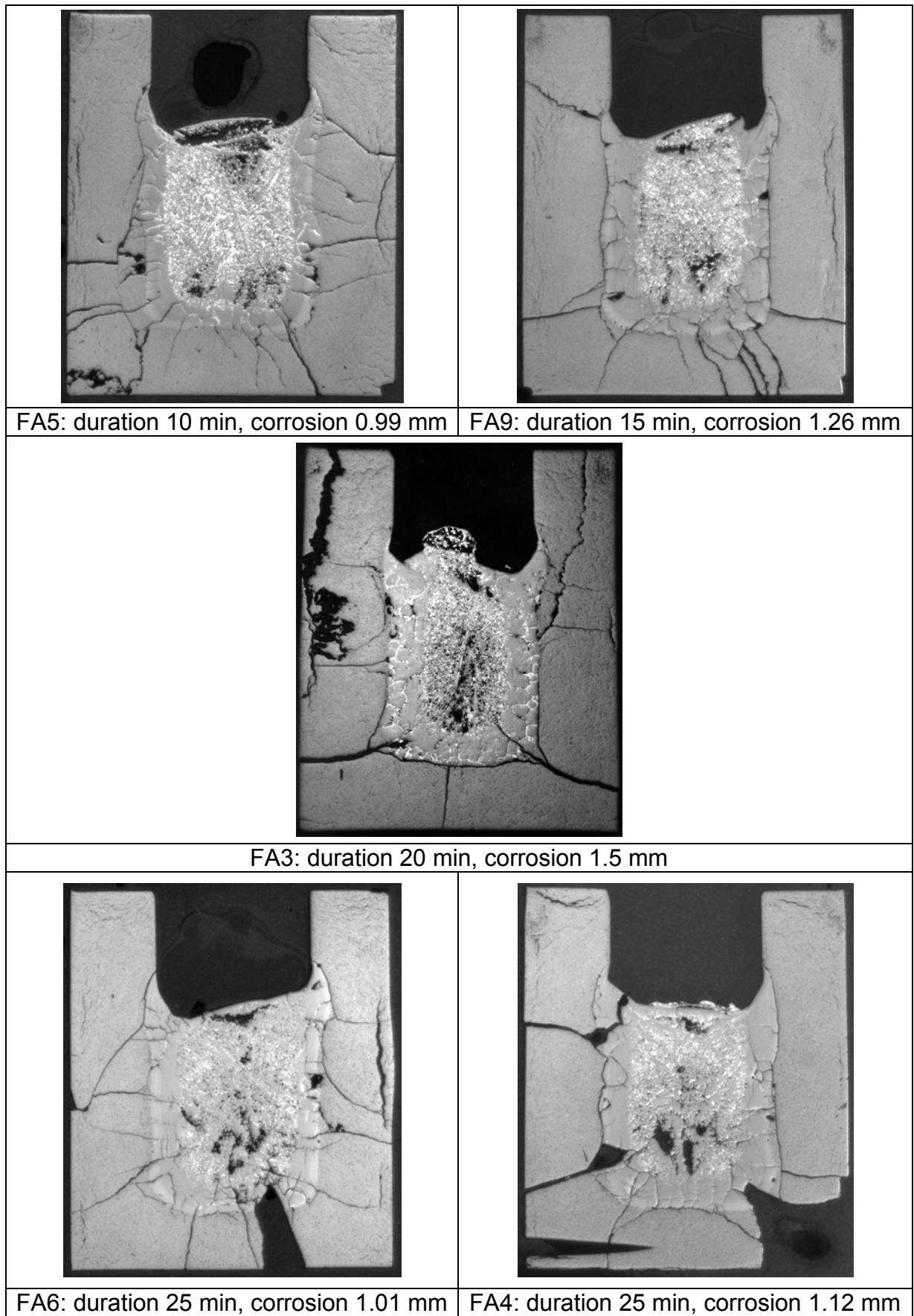
Fig. I-19: Crucible cross-sections after the dissolution tests at ~2200°C (crucible bottom temperature). Interaction surface to initial melt volume ratio: S/V~770 m^{-1}

AECL11: duration 10 min, corrosion 0.69 mm	FA11: duration 75 min, corrosion 1.69 mm
AECL12: duration 20 min, corrosion 1.00 mm	FA12: duration 200 min, corrosion 1.39 mm
AECL21: duration 30 min, corrosion 1.13 mm	FA10: duration 290 min, corrosion: 0 mm

2 mm
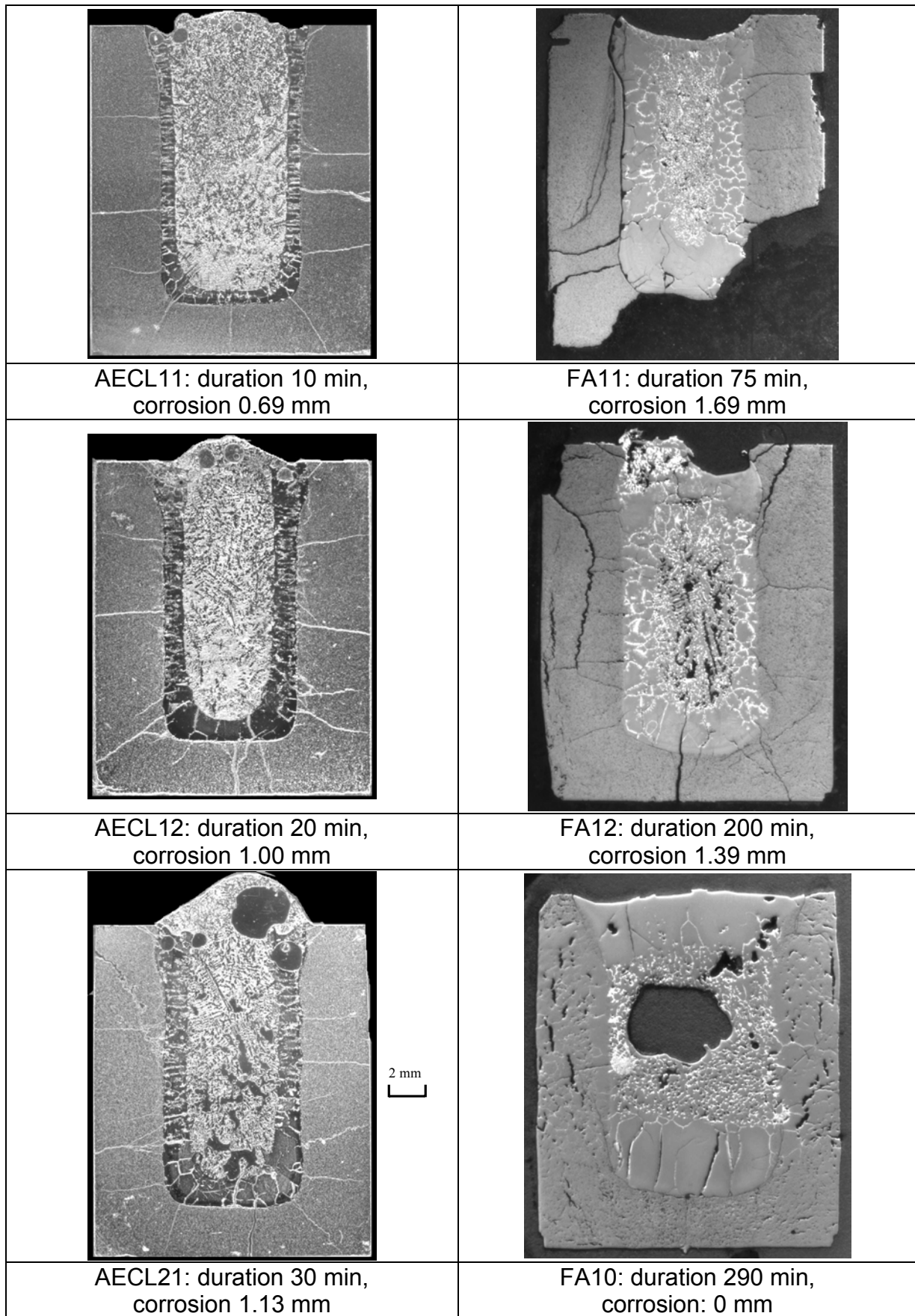
Fig. I-20: Crucible cross-sections after interaction at ~2200°C (melt surface temperature for the AECL tests and crucible bottom temperature for the FZK tests). Interaction surface to initial volume ratio: for AECL crucibles S/V=695 m^{-1}; for FZK crucibles S/V=720 m^{-1}
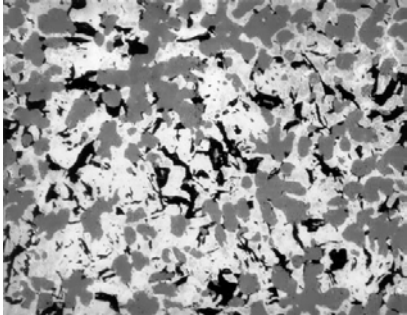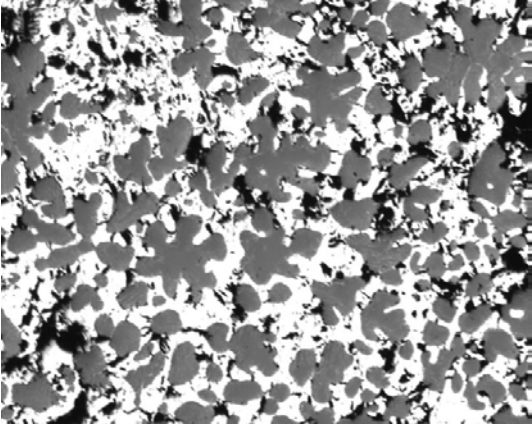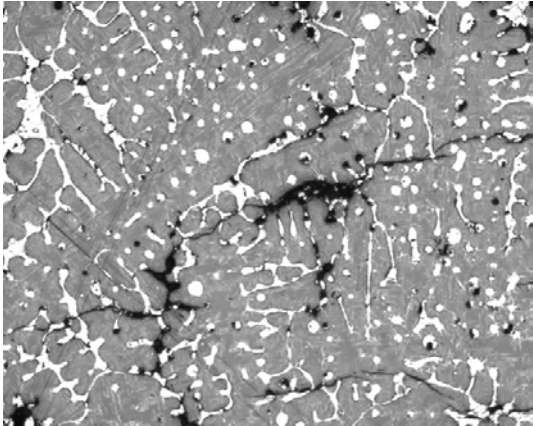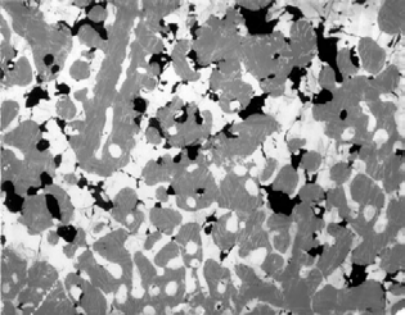
FA2 (10 min): oxygen 49.1 at%	FA8 (15 min): oxygen 55.1 at%
FA7 (30 min): oxygen 62.2 at%	FA1 (33 min): oxygen 57.5 at%

Fig. I-21: Formation of precipitates in the melt at 2100 °C; results of image analysis for the oxygen content in the melt

FA5 (10 min): oxygen 58.3 at%	FA9 (15 min): oxygen 61.5 at%
FA3 (20 min), oxygen 59.5 at%	
FA6 (25 min): oxygen 63.4 at%	FA4 (25 min): oxygen 63.5 at%
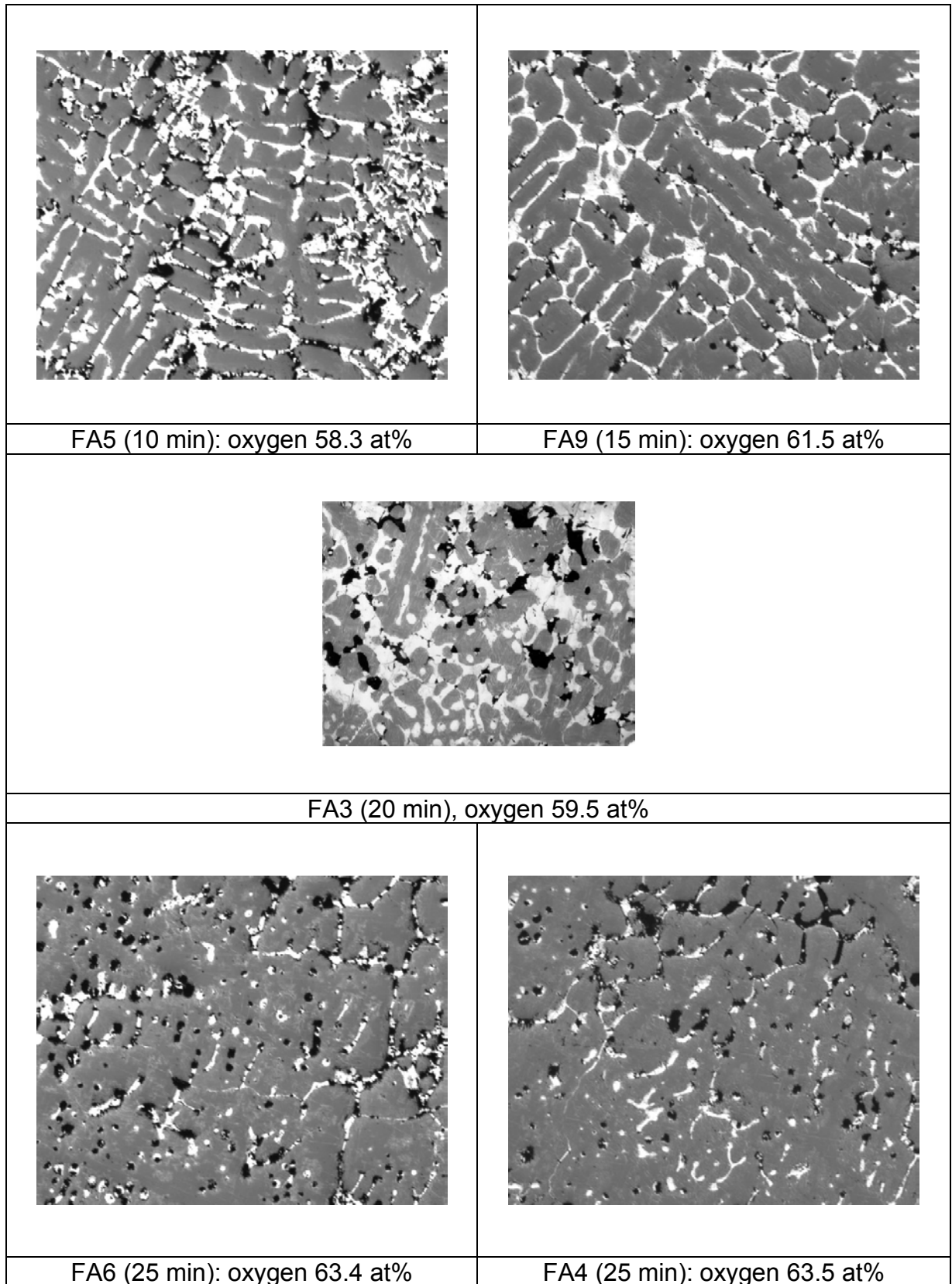
Fig. I-22: Formation of precipitates in the melt at 2200 °C (for the tests with the S/V~770 m^{-1}); results of image analysis for the oxygen content in the melt

200 μm
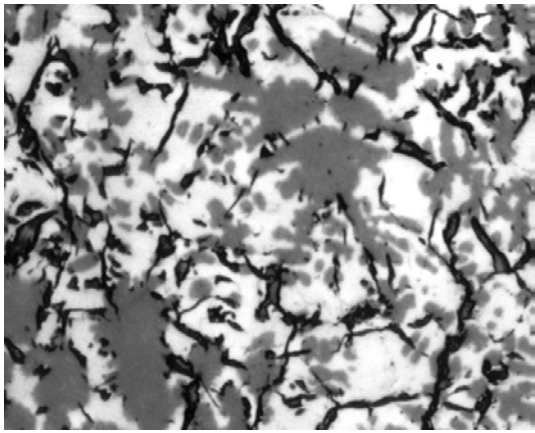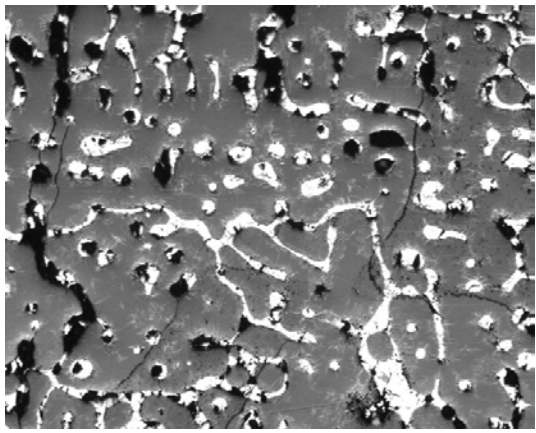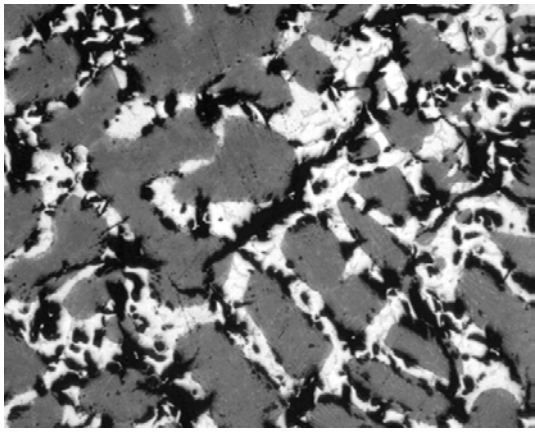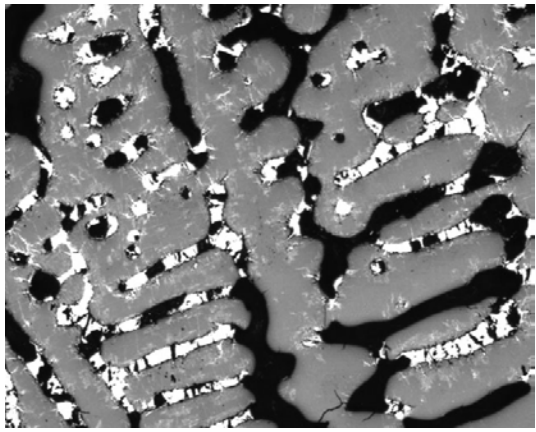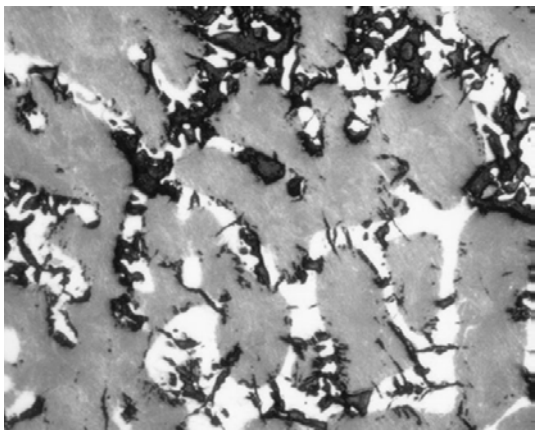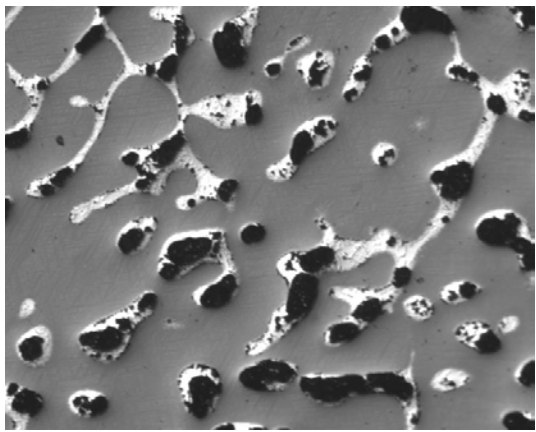
AECL11 (10 min), oxygen 50 at%	FA11 (75 min), oxygen 62.5 at%
AECL12 (20 min), oxygen 55 at%	FA12 (200 min), oxygen 63.0 at%
AECL21 (30 min), oxygen 59 at%	FA10 (290 min), oxygen 63.1 at%

Fig. I-23: Formation of precipitates in the melt at 2200 °C (for the AECL tests with the S/V~700 m^{-1} and for the FZK tests with the S/V~720 m^{-1}); results of image analysis for the oxygen content in the melt
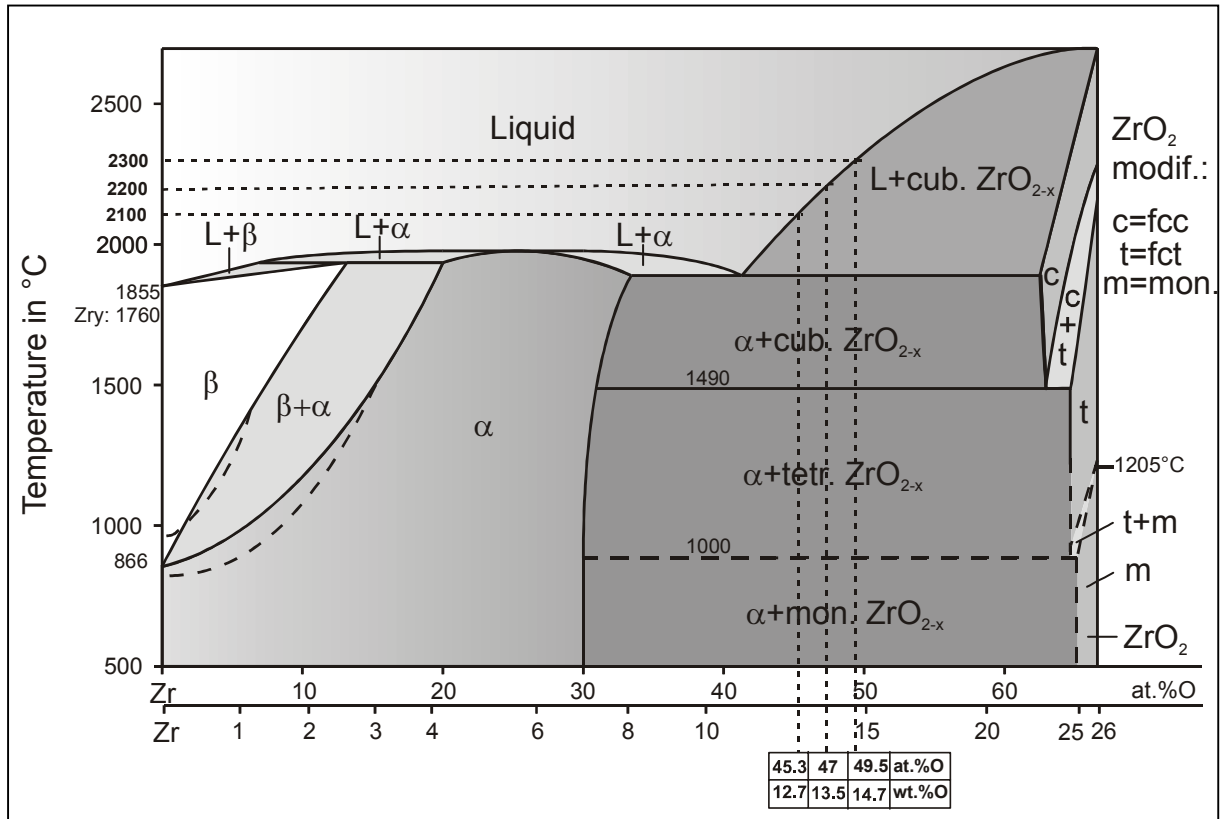
Fig. I-24: Zirconium-oxygen phase diagram. Liquidus points at 2100, 2200, 2300 °C

Part II. Modelling of Zr-O and U-Zr-O melts oxidation

M. S. Veshchunov and A. V. Berdyshev

Preface

The objective of the multi-partner task WP7.2 of the COLOSS Project is the development of models regarding the oxidation of U-O-Zr mixtures, in particular:

- Models that can adequately simulate the oxidation of U-O-Zr mixtures and related H_2 production during the core degradation phase of a severe accident.
- Models that can be integrated in SA codes.

In order to model oxidation of Zr-O and U-Zr-O melts, it was agreed to use available FZK data on post-test examinations of molten materials oxidation in the CORA and QUENCH bundle tests, as well as new FZK tests on ZrO_2 crucible dissolution by molten Zry, specially designed for investigation of long-term behaviour during the melt oxidation stage. On this base, a new model on oxidation of molten Zr-O and U-Zr-O mixtures in steam was developed, in order to analyse and explain the H_2 peak production during the quenching of degraded rods.

The first stage of the new analytical model development was presented in the Interim Report [1]. Final formulation of the analytical model, development of the numerical model and its validation against FZK test data as well as demonstration of the model applicability to the analysis of integral tests, are presented in the current Report.

1. Introduction

Oxidation of U-Zr-O and Zr-O melts in steam under high-temperature conditions of severe accidents at PWR and BWR NPP is an important phenomenon, since it determines heat and hydrogen generation after melting of Zry cladding and partial dissolution of UO_2 fuel rods. This phenomenon was observed in the out-of-pile bundle tests at the FZK facilities CORA and QUENCH where extremely high amounts of hydrogen were generated after temperature escalation above 2000°C. Post-test calculations with integral SA codes generally underpredict hydrogen generation in this stage of the tests, since there are no specific models for the corium melt oxidation, and the process is mainly described by the standard models for solid cladding oxidation formally extended to high temperatures (above the Zry melting point). However, detailed analysis of post-test micrographs of melt appearance in the tests shows that the (ordinary) growth of the peripheral oxide layer could be accompanied by extensive precipitation of ceramic particles in the bulk of the melt. This may lead to enhanced oxidation kinetics in comparison with the standard mechanism and thus may explain the reason for the observed enhancement of hydrogen generation, for instance, during the quenching of degraded rods.

In order to describe this important phenomenon, a new analytical model for the corium melts oxidation was proposed in the Interim Report [1]. This model is based on the qualitative results of post-test observations in the bundle tests CORA and QUENCH and quantitative kinetic data of the oxidation stage in the FZK crucible dissolution tests. Final formulation of the analytical model, development of the numerical model and its validation against FZK test data, are presented in the current Report.

The new model can be also applied for interpretation of post-test observations of melt appearance in Phebus FPT0 test and thus for quantitative analysis of melt oxidation also in this test.

2. Analysis of oxidation of Zr-O melts in QUENCH tests

A visual analysis of FZK micrographs of the bundle cross-sections shows that extended areas of the well-mixed molten material were formed in the QUENCH-02 and 03 tests [2,3] at different elevations.

For the quantitative analysis of these images one should keep in mind that in accordance with the equilibrium binary Zr-O phase diagram (Fig. II-1) the melt decomposes on cool-down into two phases: oxygen stabilised metallic α-Zr(O) phase and ceramic ZrO_{2-x} phase. In the case of the oversaturated melt that contains ceramic ZrO_2 precipitates already at temperature (i.e. two-phase $L+ZrO_{2-x}$ region in Fig. II-1), it is rather difficult to distinguish these precipitates from ceramic particles formed on cool-down. For this reason, image analysis of the ceramic phase fraction in the post-test micrographs can be performed and compared with reference samples (refrozen Zr-O melts with predetermined compositions). This allows to find out the oxygen content in the melt and thus to identify (from the phase diagram) what part of the observed ceramic precipitates was formed at test temperature [4].

The visual analysis of the post-test melt appearance in the QUENCH-02 test shows that at lower elevations (e.g. 850 mm, Fig. II-2a) where the melt was formed at a late stage of the test (and thus was oxidised for a shorter period of time), such «molten pools» consist mainly of pure metal Zr-O melts with low oxygen contents that decompose on cool-down into mixtures of α-Zr(O) and ZrO_{2-x} phases with a relatively low fraction of dark ceramic phase (see Fig. II-2b). Along the periphery the molten pools are confined by relatively thin (up to 1 mm) and uniform oxide layers, which form some kind of a thin-walled zirconia crucible for each molten pool (Position A in Fig. II-2a).

At higher elevations (e.g. 883 mm, Fig. II-3a) oxidation time of the melt was longer and oxygen content varies at different positions from relatively low (Position A in Fig. II-3b) to relatively high (Position B in Fig. II-3c) as can be recognised by increasing amount of dark ceramic phase.

At the elevation 950 mm (Fig. II-4a) corresponding to the bundle hot zone [2], the melt oxidation time was the largest. For this reason, the non-relocated melt was extensively converted into ceramic ZrO_2 phase (Positions B and C in Fig. II-4b) by progressive growth of bulk ceramic precipitates (compare with relatively "fresh" relocated melt in Position A). A clear separation between a relatively thin peripheral oxide layer and an extended zone formed by bulk ceramic precipitates (of the same ZrO_2 phase) can be distinguished also in Fig. II-5 (elevation 1050 mm).

Similar melt oxidation behaviour can be observed in the QUENCH-03 test. In Fig. II-6 (elevation 750 mm) one can clearly see different stages of melt bulk conversion into ceramic phase (up to complete conversion) in various locations of the melt. A clear separation between the peripheral oxide layer and bulk precipitates in relatively fresh (Fig. II-7a) and heavily oxidised (Fig. II-7b) melts can be also observed in the QUENCH-03 test at elevation 950 mm.

In Fig. II-8 a set of micrographs of the solidified melts from different locations of the QUENCH-02 and 03 bundle cross-sections is combined and quantitatively analysed by FZK experimentalists. From this figure one can clearly see that the amount of ceramic phase in the refrozen melts smoothly varies in a wide range corresponding to different oxygen contents in the melt. Assuming that temperature did not exceed 2200°C in these tests (in accordance with experimental data [2,3]), one can conclude that the majority of the samples matches to the two-phase region in the equilibrium phase diagram, Fig. II-1, i.e. a number of ceramic particles was already formed at

temperature. It is also clear that in the last two micrographs the melt was completely converted into ceramic phase at temperature via formation and growth of the ceramic precipitates in the melt bulk. This bulk oxide zone can be clearly separated from the peripheral oxide layers (Figs. II-4, II-5 and II-7b). Visual evaluation of its volume confirms that the major part of the ceramic ZrO_2 phase was formed in the course of the precipitation rather than of the peripheral oxide layer growth.

Such a behaviour of the melt in the molten pools is qualitatively similar to one observed in the zirconia crucible dissolution tests [4], where growth of the oxide layer in a late period of the "corrosion" stage was accompanied with the bulk ceramic precipitation (see Fig. II-9). This allows validation of the melt oxidation model against kinetic measurements in the crucible tests.

3. Qualitative analysis of the Zr-O melt oxidation kinetics

A preliminary analysis of the oxidation kinetics in the corrosion stage of the ZrO_2 crucible dissolution tests has been already performed in [4].

In order to explain the reasons for the observed ceramic phase precipitation at a late stage of the crucible tests, it was advised to take into account a significant temperature difference between the hot crucible outer walls and the cooler melt in the crucible tests. In accordance with data presented in [4], this difference attained 50–100 K. Simple estimations show that the temperature difference between the inner crucible wall and the melt bulk attained a few degrees in these tests. Similar temperature difference between solid and liquid phases can be readily attained in the bundle tests where thermal sources (simulated decay heat and exothermic heat of Zr oxidation) are located in the solid phases (heated rods and peripheral oxide layers).

Since the melt is well mixed in the crucible tests and thus has a homogeneous temperature and composition distribution in the melt bulk, a thin transition layer exists in the melt near to the interface in which temperature and concentration changes occur. The melt in the transition layer at the interface sustains the thermodynamically equilibrium state with the crucible wall. Owing to the temperature difference between the melt bulk and interface, this state differs from the saturated state in the melt bulk. For this reason, the concentration drop in the transition layer still exists even when the bulk of the melt attains the saturation level (corresponding to reduced temperature as compared to the wall). Thus, oxygen supply from the walls to the melt bulk through the transition layer continues after the melt saturation attainment. In this situation the melt unavoidably becomes oversaturated (and matches to the two-phase region of the phase diagram) and continues to consume oxygen until it completely precipitates into the ceramic phase (see Fig. II-9).

Such a behaviour differs considerably from that under isothermal conditions. Indeed, under isothermal conditions the melt saturation state coincides with the melt/crucible equilibrium state sustained at the interface and, for this reason, oxygen flux to the melt disappears with the saturation approach.

In the preliminary analysis [4] of mass balances it was shown that the ordinary oxidation kinetics equation:

$$\frac{\partial L}{\partial t} = \frac{J^*}{L(t)},$$

(1)

where $L(t)$ is the growing oxide layer thickness, $J^* \propto -D_O^{ZrO_2}\Delta\rho_O$ characterises the solid state diffusion flux due to the oxygen concentration drop $\Delta\rho_O$ across the oxide layer, under conditions of bulk ceramic precipitation will be transformed into the new one:

$$\frac{\partial(W/S)}{\partial t} + \frac{\partial L}{\partial t} = \frac{J^*}{L(t)},$$

(2)

where W is the total volume of the precipitates, S is the area of interface between melt and oxide layer. It is clearly seen from Eq. (2) that the parabolic rate solution of Eq. (1), $L(t) \propto t^{1/2}$ is not anymore valid, since the oxygen flux from oxide is now consumed also by precipitates. This naturally results in a slower growth of the oxide layer thickness $L(t)$ which provides a barrier for the oxygen penetration. In its turn, a slower growth of the barrier leads to subsequent increase (in comparison with the

ordinary case, Eq. (1)) of the total oxygen consumption by the growing ceramic phase (oxide layer + precipitates) and thus, to the increase of the total volume of the ceramic phase ($W + LS$) (in comparison with the ordinary case). In the limiting case of a very slow oxide layer growth, the oxygen flux does not anymore reduce with time leading to a linear rise of the ceramic phase volume with time (instead of the parabolic time law in the ordinary case).

Therefore, an important qualitative conclusion was drawn that the total amount of the ceramic ZrO_2 phase formed under precipitation conditions in the oxidising melt might be significantly higher than that in the ordinary oxidation case. This conclusion can be applied to the interpretation of the oxidation kinetics and hydrogen generation in the QUENCH-02 and -03 tests, where extremely large amounts of hydrogen were produced in the course of molten Zry clad oxidation.

4. Model for Zr-O melt oxidation

The simplest formulation of the one-dimensional model for the Zr-O melt oxidation in plane geometry is presented in the current section. More general formulation including cylindrical geometry will be presented below in section 6 in application to the three component (U-Zr-O) system. As demonstrated in [4,5], one-dimensional models can be readily used either for interpretation of the crucible tests, or for application to the bundle tests. Generalisation to the two-dimensional case is also straightforward [5].

In accordance with the qualitative consideration in the previous section, schematic representation of the considered layered structure along with a segment of the binary Zr-O phase diagram is shown in Fig. II-10. It is assumed that the temperature T_I at the solid/liquid interface is somewhat different from the temperature T_B in the bulk of the melt stirred by the natural convection. In accordance with the phase diagram, the corresponding oxygen concentrations at the interface $c_O(I)$ and in the melt bulk $c_O(B)$ are also different. Temperature and oxygen concentration drops occur in a thin transition layer δ at the interface.

4.1. Saturation stage

In the first ("saturation") stage until saturation in the melt bulk is not attained, the system of equations for the mass transfer has the standard form (compare, for example, with [6]):

- Mass balances

$$-D_O^{ZrO_2}\frac{\partial \rho_O}{\partial x}\bigg|_I - \rho_O(I)\frac{dL}{dt} = \frac{d}{dt}\big[c_O(B)M\big] \,, \tag{3}$$

$$-\rho_{Zr}\frac{dL}{dt} = c_{Zr}\frac{dM}{dt} \,, \tag{4}$$

- Flux matches

$$-D_O^{ZrO_2}\frac{\partial \rho_O}{\partial x}\bigg|_I - \rho_O(I)\frac{dL}{dt} = c_O(I)\left(u - \frac{dL}{dt}\right) + k_O\big(c_O(I) - c_O(B)\big) \,, \tag{5}$$

$$-\rho_{Zr}\frac{dL}{dt} = c_{Zr}\left(u - \frac{dL}{dt}\right). \tag{6}$$

where

      L – thickness of the oxide layer,

      M – thickness of the melt layer,

      $\rho_{O(Zr)}$ – oxygen (zirconium) molar density in the oxide layer,

      $c_{O(Zr)}$ – oxygen (zirconium) molar density in the melt,

      $D_O^{ZrO_2}$ – oxygen diffusion coefficient in the oxide layer,

      k_O – oxygen mass transfer coefficient in the melt,

      u – net velocity of the melt (due to the density difference between liquid Zr and solid ZrO_2 phases).

It is also assumed that the Zr molar density in the melt c_{Zr} is independent of oxygen (like in the solid α-Zr(O) phase) and approximately equal to 0.067 mol/cm^3 .

In the melt stirred by natural convection, mass transfer coefficient k_O is calculated as

$$k_O = \frac{D_O^{liq}}{\delta} ,$$

where δ is the thickness of the transition boundary layer,

$\delta \approx d\,/Sh^{1/4} = d\,\Big/\!\left(0.54 Gr^{1/4} Sc^{1/4}\right)$, if the product of the Grashoff number $Gr = g\left(\Delta\rho/\rho\right)d^3/v^2$ and the Schmidt number $Sc = v/D$ is $Gr{\cdot}Sc > 10^3$,

and d is characteristic dimension of the melt (i.e. in the considered one-dimensional geometry $d = M$).

Similarly to [7], this can be written in the form:

$$k_O = k_O^* \left(c_O(I) - c_O(B)\right)^{1/4} , \tag{7}$$

where $k_O^* \approx 0.54 \left(\dfrac{g\,(D_O^{liq})^3 M_O}{vdc_{Zr} M_{Zr}} \right)^{1/4}$,

D_O^{liq} – oxygen diffusion coefficient in the melt,

v – viscosity of the melt,

$M_{O(Zr)}$ – atomic weight of O (Zr).

In the diffusion regime when $Gr{\cdot}Sc < 10^3$, mass transfer by molecular diffusion in the melt should be considered as described in the Report [1]. For simplicity of numerical calculations in the current report, the convection equations, Eqs. (3)–(6) will be applied to the diffusion regime by formal extension to the limit $Sh \to 1$, i.e. $\delta \approx M$ (also in the following consideration of the precipitation stage).

Solution of the system of Eqs. (3)–(6):

$$\frac{\partial L}{\partial t} = - \frac{D_O^{ZrO_2} \left.\dfrac{\partial \rho_O}{\partial x}\right|_I + k_O\left(c_O(I) - c_O(B)\right)}{\rho_O(I) - c_O(I)\dfrac{\rho_{Zr}}{c_{Zr}}} , \tag{8}$$

describes "erosion" (dissolution) of the oxide layer, if

$$k_O\left(c_O(I) - c_O(B)\right) > -D_O^{ZrO_2} \left.\frac{\partial \rho_O}{\partial x}\right|_I ,$$

and "corrosion" (growth of the oxide layer), otherwise.

During the saturation stage the oxygen concentration in the melt increases in accordance with the equation:

$$L\frac{dc_O(B)}{dt} = \left(c_O(I) - c_O(B)\right)\left(\frac{dL}{dt} + k_O\right) , \tag{9}$$

until the saturation c_O^* value is reached. Since the concentration gradient still exists in the boundary layer due to the temperature difference (as explained in section 3), the oxygen flux to the melt will keep on leading to oversaturation of the melt and onset of precipitation.

4.2. Precipitation stage

In the new ("precipitation") stage of the oxidation process one should incorporate input from the ceramic precipitates in the mass balance equations considering the liquid phase composition as saturated:

- Mass balances

$$-D_O^{ZrO_2} \frac{\partial \rho_O}{\partial x}\bigg|_I - \rho_O(I)\frac{dL}{dt} = \frac{d}{dt}\left[c_O^* M(1-f) + \rho_O^* Mf\right],\qquad(10)$$

$$-\rho_{Zr}\frac{dL}{dt} = \frac{d}{dt}\left[c_{Zr}M(1-f) + \rho_{Zr}Mf\right],\qquad(11)$$

where f is the volume fraction of the ceramic precipitates in the uniformly stirred melt in the bulk region. In the mass balances a thin transition layer is neglected due to its small thickness, $\delta << L, M.$

As to the flux matches, the form of these equations strongly depends upon whether precipitates are formed in the transition layer or not. Lacking the free convection theory for simultaneous heat and mass transfer [8,9], one can generally consider two options. Owing to a large value of the Schmidt number $Sc = \nu/D$ in comparison with the Prandtl number $Pr = \nu/\chi$ for liquids (where ν, χ and D are viscosity, thermal diffusivity and mass diffusion coefficient, respectively), one can conclude (similarly to the forced convection case) that the diffusion boundary layer δ_d is at least not larger than the thermal boundary layer δ_t, i.e. $\delta_d \le \delta_t$.

If it is smaller, $\delta_d << \delta_t$ (as usually occurs in forced convection theory), then the concentration drop from $c_O(I)$ to c_O^* virtually occurs at temperature T_I , that is in the one-phase (Liquid) region of the phase diagram (<u>Fig. II-10</u>). In this case precipitation does not take place in the transition layer (i.e. $f = 0$ in this layer), and the system of equations takes the form:

- Flux matches (case 1)

$$-D_O^{ZrO_2} \frac{\partial \rho_O}{\partial x}\bigg|_I - \rho_O(I)\frac{dL}{dt} = c_O(I)\left(u - \frac{dL}{dt}\right) + \tilde{k}_O\left(c_O(I) - c_O^*\right),\qquad(12)$$

$$-\rho_{Zr}(I)\frac{dL}{dt} = c_{Zr}\left(u - \frac{dL}{dt}\right),\qquad(13)$$

The value of mass transfer coefficient k_O slowly decreases with growth of precipitates in the melt, $k_O \propto Sh \propto \nu^{-1/4}$, due to increase of the apparent viscosity ν of the solid-liquid mixture with the increase of the volume fraction f of solid precipitates. In accordance with recommendation of [10] for corium in the solidification range, the Arrhenius law can be used for the apparent viscosity: $\nu = \nu_{liq}\exp(2.5Cf)$, where ν_{liq} is the liquid phase viscosity, C is an adjustable coefficient in the range 4–4.8. Therefore, a new value

$$\tilde{k}_O = k_O \cdot \exp(-2.5Cf/4) \approx k_O \cdot \exp(-2.5f),\qquad(14)$$

with k_O determined in Eq. (7), is introduced in Eq. (12) to consider increase of viscosity due to precipitation of the ceramic phase in the melt.

In the other case, $\delta_d \approx \delta_t$, the concentration drop occurs in the same boundary layer as the temperature drop. In this case, the two-phase region is formed also in the

boundary layer and a local equilibrium between the liquid and solid phases is sustained in each spatial point. As shown in Appendix, the molecular diffusion in the boundary layer can be approximated by the quasi-stationary solution of the diffusion mass-transfer problem in the two-phase region under temperature gradient $(T_I - T_B)/\delta$. This provides an approximate solution $f \approx$ const., that matches to the bulk value f_B at the interface between the boundary layer and the melt (dotted line in Fig. II-10). Therefore, in this approximation flux matches take the form:

- Flux matches (case 2)

$$-D_O^{ZrO_2}\frac{\partial\rho_O}{\partial x}\bigg|_I - \rho_O(I)\frac{dL}{dt} = [c_O(I)(1-f) + \rho_O(I)f]\cdot\left(u - \frac{dL}{dt}\right)$$

$$+ (1-f)\frac{D_O^{liq}\Delta c_O}{\delta} + f\frac{D_O^{ZrO_2}\Delta\rho_O}{\delta}, \quad (15)$$

$$-\rho_{Zr}(I)\frac{dL}{dt} = [c_{Zr}(I)(1-f) + \rho_{Zr}(I)f]\cdot\left(u - \frac{dL}{dt}\right), \quad (16)$$

where $\Delta c_O = c_O(I) - c_O^*$, $\Delta\rho_O = \rho_O(I) - \rho_O^*$ (see Eqs. (A.5) and (A.6) in Appendix).

In Eq. (15) the last two terms can be compared with each other in the following way. Despite $\Delta c_O/\Delta\rho_O \sim 0.1$ is small (in accordance with the binary phase diagram in Fig. II-1), it is practically compensated by a large ratio $D_O^{ZrO_2}/D_O^{liq}$ which at 2100°C attains one order of magnitude. Indeed, in accordance with experimental data [11] $D_O^{liq} \approx 1\cdot10^{-4}$ cm²/s at 2100°C, whereas $D_O^{ZrO_2}$ at this temperature was evaluated in [12] as $8\cdot10^{-4}$ cm²/s. Lacking exact numerical data for these parameters, one can roughly estimate $\frac{D_O^{liq}\Delta c_O}{\delta} \approx \frac{D_O^{ZrO_2}\Delta\rho_O}{\delta}$, and in this case Eq. (15) practically coincides with Eq. (12).

Further improvement of such an approximation is straightforward and can be performed on the base of more reliable data for the above indicated parameters $\Delta c_O/\Delta\rho_O$ and $D_O^{ZrO_2}/D_O^{liq}$. Nevertheless, now it is clear that the differences between two cases 1 and 2 is not significant and can lead only to some quantitative rather than qualitative difference in the results of calculations (taking into account that also some difference exists between Eqs. (13) and (16)). For this reason, only system of Eqs. (12) and (13) will be studied further in the present report.

Solution of Eqs. (10)–(13) takes the form:

$$\frac{dL}{dt} = -\frac{D_O^{ZrO_2}\frac{\partial\rho_O}{\partial x}\bigg|_I + \tilde{k}_O(c_O(I) - c_O^*)}{\rho_O(I) - c_O(I)\frac{\rho_{Zr}}{c_{Zr}}}, \quad (17)$$

and, in the first order approximation with respect to a small value $c_O(I) - c_O^* \ll \rho_O - c_O^*\rho_{Zr}/c_{Zr}$,

$$\frac{\partial M}{\partial t} = \frac{\dfrac{\rho_{Zr}}{c_{Zr}} D_O^{ZrO_2} \dfrac{\partial \rho_O}{\partial x}\bigg|_I + \tilde{k}_O (c_O(I) - c_O^*)}{\rho_O(I) - c_O(I) \dfrac{\rho_{Zr}}{c_{Zr}}}, \tag{18}$$

$$\frac{\partial (Mf)}{\partial t} = \frac{\tilde{k}_O (c_O(I) - c_O^*)}{\rho_O(I) - c_O(I) \dfrac{\rho_{Zr}}{c_{Zr}}} + \frac{\dfrac{\rho_{Zr}}{c_{Zr}} D_O^{ZrO_2} \dfrac{\partial \rho_O}{\partial x}\bigg|_I (c_O(I) - c_O^*)}{\left(\rho_O(I) - c_O(I) \dfrac{\rho_{Zr}}{c_{Zr}} \right) \left(\rho_O^* - c_O^* \dfrac{\rho_{Zr}}{c_{Zr}} \right)}. \tag{19}$$

Hereafter, for simplicity we shall neglect the difference between $\rho_O(I)$ and ρ_O^* and designate $\rho_O(I) \approx \rho_O^* \equiv \rho_O$ taking into account a steep slope of the solidus line in the real phase diagram, Fig. II-1.

From Eqs. (8) and (18) one can deduce that in the precipitation stage (i.e. when $c_O(B) = c_O^*$) various regimes are possible:

- growth of oxide layer (corrosion) and of precipitates, if

$$-\frac{\dfrac{\rho_{Zr}}{c_{Zr}} D_O^{ZrO_2} \dfrac{\partial \rho_O}{\partial x}\bigg|_I (c_O(I) - c_O^*)}{\left(\rho_O - c_O^* \dfrac{\rho_{Zr}}{c_{Zr}} \right)} < \tilde{k}_O (c_O(I) - c_O^*) < -D_O^{ZrO_2} \dfrac{\partial \rho_O}{\partial x}\bigg|_I, \tag{20}$$

- growth of oxide layer (corrosion) and dissolution of precipitates, if

$$\tilde{k}_O < -\frac{\dfrac{\rho_{Zr}}{c_{Zr}} D_O^{ZrO_2} \dfrac{\partial \rho_O}{\partial x}\bigg|_I}{\left(\rho_O - c_O^* \dfrac{\rho_{Zr}}{c_{Zr}} \right)}, \tag{21}$$

- dissolution of oxide layer (erosion) and growth of precipitates, if

$$\tilde{k}_O (c_O(I) - c_O^*) > -D_O^{ZrO_2} \dfrac{\partial \rho_O}{\partial x}\bigg|_I. \tag{22}$$

Analysis of Eqs. (17)–(19) can be done separately for the two above-mentioned situations: melt oxidation in steam and in zirconia crucibles at the corrosion stage.

4.2.1. Melt oxidation in steam

In this case diffusion flux through the oxide layer with a thickness $L(t)$ under normal oxidation conditions (i.e. without starvation) can be approximated by a linear flux $D_O^{ZrO_2} \dfrac{\partial \rho_O}{\partial x}\bigg|_I \approx -D_O^{ZrO_2} \dfrac{\Delta \rho_O^{st}}{L}$, where $\Delta \rho_O^{st} = \rho_O^{(st)} - \rho_O(I)$ is the oxygen concentration drop across the layer, corresponding to the substoichiometry interval in the phase diagram at oxide temperature, Fig. II-10. Therefore, Eq. (17) can be represented in the form:

$$\frac{dL}{dt} = \frac{A}{L} - B, \tag{23}$$

where

$$A = \frac{D_O^{ZrO_2} \Delta \rho_O^{st}}{\rho_O - c_O(I) \dfrac{\rho_{Zr}}{c_{Zr}}}, \quad B = \frac{\tilde{k}_O \Delta c_O}{\rho_O - c_O(I) \dfrac{\rho_{Zr}}{c_{Zr}}}, \quad \Delta c_O = c_O(I) - c_O^{*}. \tag{24}$$

Neglecting dependence of $\tilde{k}_O$ on viscosity variation due to precipitation of ceramic particles in the melt, one can consider Eq. (24) in a quasi-stationary approximation (with respect to time variation of this parameter). Solution of this equation determines the growth of the oxide layer up to a stable value:

$$L^{*} = \frac{A}{B} = \frac{D_O^{ZrO_2} \Delta \rho_O^{st}}{\tilde{k}_O \Delta c_O}, \tag{25}$$

in accordance with a time dependence at $t \gg t^{*} = A/B^2$:

$$L = L^{*} \left[1 - C \exp\left(-\frac{t - t_{sat}}{t^{*}} \right) \right], \tag{26}$$

where $\quad C = \exp\left[-1 + \dfrac{L_{sat}}{L^{*}} + \ln\left(1 - \dfrac{L_{sat}}{L^{*}} \right) \right], \quad$ and $\quad L_{sat}$ is oxide thickness in the end of the saturation stage at $t = t_{sat}$.

As the stable oxide thickness L^{*} is approached, the oxygen flux through this layer approaches a constant and thus provides a linear time dependence for the growth of the total volume (Mf) of ceramic precipitates:

$$\frac{\partial(Mf)}{\partial t} \approx B, \quad \text{or} \quad Mf \approx \frac{\tilde{k}_O \Delta c_O}{\rho_O - c_O(I) \dfrac{\rho_{Zr}}{c_{Zr}}} t, \tag{27}$$

at $t \gg t^{*}$.

Therefore, the total volume ($L+Mf$) of the ZrO$_2$ ceramic phase (oxide layer + precipitates) increases linearly with time at a late stage of the Zr-O melt oxidation (i.e. oxidation kinetics is linear).

Taking into account decrease of $\tilde{k}_O$ due to precipitation of ceramic particles in the melt, $\tilde{k}_O \propto v^{-1/4}$, (see Eq. (14)), one can show that oxidation kinetics becomes slower than linear, but still significantly faster than parabolic. To illustrate this, calculations of Zr melt oxidation with the new numerical model (which will be additionally analysed below in section 4.3) are presented in Fig. II-11. Calculations were performed for the melt in cylindrical geometry with radius 6 mm at melt temperature 2473 K and temperature drop in the transition boundary layer at the solid/melt interface 10 K. From this figure one can see that in neglect of viscosity dependence on precipitates, linear oxidation kinetics manifested by constant oxide layer thickness along with a linear growth of precipitates takes place after some transient period ≈ 400 s, in accordance with the analytical predictions, Eq. (27). Complete conversion of the melt in the ceramic phase (oxide layer + precipitates) occurs after ≈ 1300 s. In a more realistic case, when increase of viscosity due to precipitation and $\tilde{k}_O \propto v^{-1/4}$ are taken into account, complete solidification of the melt predicted by the new model occurs after ≈ 2200 s, whereas the standard parabolic model (i.e. curve $\Delta T = 0$) predicts nearly a half of the melt solidification (conversion to the oxide layer) during this time period.

40

4.2.2. Melt oxidation in crucible tests

In this case diffusion flux in the crucible walls can be roughly approximated by a quasi-stationary solution with a slow boundary movement:

$$D_O^{ZrO_2} \frac{\partial \rho_O}{\partial x}\bigg|_I \approx -D_O^{ZrO_2} \frac{\Delta \rho_O}{\sqrt{\pi D_O^{ZrO_2} t}}$$. Substitution in Eq. (17) yields:

$$\frac{dL}{dt} = \frac{A}{\sqrt{\pi D_O^{ZrO_2} t}} - B ,$$

(28)

with constants A and B from Eq. (24).

Solution of Eq. (28) has form:

$$L - L_{sat} = 2\frac{A}{\sqrt{\pi D_O^{ZrO_2}}}\left(\sqrt{t} - \sqrt{t_{sat}}\right) - B\left(t - t_{sat}\right),$$

(29)

and, in accordance with more general predictions, Eqs. (20) and (22), controls the oxide layer growth (corrosion) at $t < t_{max}$ and dissolution (erosion) at $t > t_{max}$, where $t_{max} = A^2 / \pi D_O^{ZrO_2} B^2$. Since this time t_{max} is inversely proportional to a small value $\Delta c_O = c_O(I) - c_O^*$, it might be too large to be attained in the relatively short-term tests [4]. In order to check this model prediction (i.e. transformation of corrosion to erosion at a late stage of interactions), additional long-term tests were recommended in [1] for implementation in FZK.

4.3. Numerical calculations

Validation of the one-dimensional numerical model in the cylindrical geometry formulation was performed against various ZrO_2 crucible dissolution test series, including previous AECL and FZK short-term (up to 30 minutes) tests as well as new FZK long-term (up to 290 minutes) tests that were specially designed for verification of the new model predictions, Eq. (29), concerning "renewed" dissolution behaviour during the late stage of interactions.

4.3.1. AECL tests

For the analysis of the previous AECL test series' [4], the erosion/corrosion model based on Eqs. (8) and (9), i.e. without consideration of precipitation mechanism, was applied in [4]. As a result, being compared with the experimental data the model calculations demonstrated a very good agreement with the measurements in the first ≈ 500 s of the interactions; however, at a later stage of the corrosion period the model overpredicted the corrosion layer thickness. Deviations of the calculated kinetic curves from the experimental points occurred practically simultaneously with the onset of the experimentally identified melt oversaturation, i.e. when the oxygen melt content exceeded ≈ 14 at.% at 2100°C and ≈ 15 at.% at 2200°C. This additionally confirmed the assumption on the ceramic ZrO_2 phase precipitation in the melt bulk at a late stage of corrosion.

Application of the new numerical model based on Eqs. (10)–(13), to the crucible test geometry allows elimination of the discrepancy between model predictions and measurements. The basic set of model parameters was fixed (at the same values as in the previous calculations [4]), and only temperature difference between the melt and inner crucible walls was varied in the new calculations.

As already mentioned in section 3, the temperature difference between melt and outer crucible walls attained 50-100 K in these tests. Taking into account relatively high ratio of thermal conductivity values in the metallic melt and ZrO_2 walls and relatively small thickness of transition boundary layer in the melt, and matching heat fluxes in the wall and transition boundary layer, one can estimate the temperature drop in the melt (across the boundary layer) as a few degrees. An ambiguity in such an estimation is connected with high uncertainty in temperature difference measurements, uncertain evaluation of thermal conductivity of Zr melt oversaturated with oxygen during precipitation stage of interactions, as well as possible thermal resistance at the melt/solid interface due to incomplete wetting of the solid surface. For these reasons, in the following calculations the temperature drop was varied in the range 0-6 K.

Results of calculations by the new model of the AECL tests are presented in Figs. II-12 and II-13 along with curves ($\Delta T = 0$) calculated by the previous model without consideration of the temperature drop across the boundary layer (i.e. based on Eqs. (3)-(6)). A satisfactory agreement with measurements was attained with a reasonable value of the varied parameter $\Delta T = 6$ K.

4.3.2.   FZK tests

In order to check the predictions of the new analytical model [1] presented in section 4.2.2, additional long-term tests were implemented in FZK at melt temperature 2200°C. Detailed description of these tests is presented in the attached FZK report. These tests qualitatively confirmed the main model predictions concerning transformation of corrosion (growth of oxide layer) to erosion (renewed dissolution of oxide layer) at a late stage of interactions, and were used for further validation of the numerical model.

As in the AECL tests calculations presented in section 4.3.1, only temperature drop across the boundary layer was varied in the new calculations, whereas all other parameters were fixed corresponding to a slightly different geometry of the FZK crucibles (i.e. $S/V = 720$ m^{-1}, instead of 695 m^{-1} in the AECL tests). The best fit for the tests FA11 and FA12 was attained with $\Delta T = 6$ K (see Fig. II-14), whereas for the test FA10 – with $\Delta T = 10$ K (see Fig. II-15). This qualitatively well corresponds to a significantly higher temperature difference between pyrometer and thermocouple measurements in the tests FA10 in comparison with that in the tests FA11 and FA12. A very high precipitation of the ceramic phase in the melt observed experimentally in these long-term tests is also in a qualitative agreement with calculations.

 A series of short-term (up to 33 minutes) FZK tests FA1, FA2, FA7 and FA8 carried out at melt temperature 2100°C in similar crucibles, but with a smaller amount of Zry charge (corresponding to $S/V = 770$ m^{-1}) were fairly well reproduced by the model with the increased temperature difference $\Delta T = 10$ K (see Fig. II-16). Test FA3 at 2200°C with the same crucible parameters was also simulated by the model with the same temperature difference $\Delta T = 10$ K (see Fig. II-17). However, other short-term tests FA5, FA6 and FA9 at 2200°C were satisfactory described by the model only with the artificially increased parameter $\Delta T = 20$ K (see Fig. II-18). To some extent this can be explained by a rather high temperature difference between pyrometer and thermocouple measurements in these tests, however, should be additional clarified.

In general, one can conclude that the new model allows quite reasonable simulation of various tests on ZrO_2 crucible interactions with Zry melt and explanation of the observed high precipitation of ceramic particles in the melts (up to complete

conversion to the ceramic phase) during melt oxidation in the late stage of interactions. On the base of this conclusion, one can attempt to apply the model for interpretation of Zr-O melt oxidation behaviour in the bundle QUENCH tests.

4.3.3. Melt oxidation in QUENCH tests

As described in section 2, post-test analysis of FZK micrographs of the bundle cross-sections shows that extended areas of the well-mixed molten material were formed in the QUENCH-02 and 03 tests [2,3] at different elevations. Keeping in mind that in the hottest zone molten material existed less than 200 seconds before freezing by quenching, one can consider these micrographs as "snap-shots" of a real picture of melt configuration just after cladding melting. Therefore, an important conclusion about melt behaviour at high temperature can be derived from these observations. Namely, one can conclude that after metal cladding melting and oxide shell failure, melt was agglomerated in extended "molten pools" that surrounded groups of fuel rods and were confined along their periphery by oxide layers. Such pools were apparently prevented from quick downward relocation by a supporting crust formed due a rather steep axial temperature gradient in the hot zone (50-80 K/cm [2,3]). For the CORA tests a similar conclusion on a very slow downward relocation ($\sim$ 1 mm/s) of molten slug rather than rapid melt slumping ($\sim$ 50 cm/s) in the form of droplets and rivulets, was derived in [13] on the base of post-test analysis [14] of the CORA tests.

In this situation modelling of molten pool oxidation becomes rather important task, in order to explain either the observed microstructures or high hydrogen generation detected in the tests and generally underpredicted in the standard approach. An attempt to apply the new model to such a description is presented in the current section.

Due to the above-mentioned steep temperature gradient in the rod axial direction, melt in a pool:

- is generally well mixed, as detected in the post-test analysis, and

- in the hot zone can have significantly lower temperature than surrounding ceramic materials (pellets and peripheral oxide layers), due to mixing with a colder fraction of the melt at lower elevations of the pool.

This allows varying the new model parameter ΔT, i.e. temperature difference between solid and melt across the transition boundary layer, in a rather wide interval.

For simulation of melt oxidation behaviour in steam, a molten pool in the cylindrical geometry with the characteristic radii $R \sim 0.5$ cm observed in the post-test micrographs (see section 2), is considered. For the pool with the height comparable with the diameter ($\sim$ 1 cm), in the axial temperature gradient along oxidised cladding surface 50-80 K/s the temperature difference between solid and melt at the hottest elevation of this pool can readily attain $\sim$ 50 K.

In order to analyse oxidation kinetics dependence on ΔT, calculations with two different values of this parameter for fixed geometry of molten pool $R = 6$ mm at maximum QUENCH tests temperature 2200°C, are compared in Fig. II-19. From this figure one can see that the temperature difference $\Delta T = 10$ K is too small to explain significant solidification of the melt during $\approx$ 200 s, that was observed, for example, in Figs. II-3c, II-4a-c and II-6. Increase of the temperature difference up to 50 K significantly improves model predictions concerning partial solidification of the melt (up to $\approx$ 50%) during 200 s. Time to complete solidification can be reduced to 400 s for small molten pools with $R = 2$ mm, as presented in Fig. II-20.

Oxidation of melt at ΔT = 10 K in large and small pools is compared in Fig. II-21. One can see that a relative portion of ceramic precipitates with respect to the total amount of the oxide phase (oxide layer + particles) as well as time to complete solidification of melt, increase for large molten pools owing to a large volume to surface (V/S) ratio. A similar conclusion will be derived also for U-Zr-O melts in section 6.3.

5. Analysis of oxidation of U-Zr-O melts in CORA tests

A visual analysis of FZK micrographs of the bundle cross-sections in CORA-W1 and W2 tests [15,16] can be performed in a similar way to that for QUENCH tests presented in section 2. Analysis of the three-component U-Zr-O melt in the CORA post-test images is more complicated, however, behaviour of the melts on cool-down is qualitatively similar to the binary Zr-O system. Indeed, as one can see from the quasi-binary cross-sections of the ternary U-Zr-O phase diagram (e.g. Fig. II-22), the melt decomposes on cool-down into two phases: oxygen stabilised metallic α-Zr(O) phase and ceramic $(U,Zr)O_2$ phase. In the case of the oversaturated melt that contains ceramic precipitates already at temperature (two-phase $L+(U,Zr)O_2$ region in Fig. II-22), the same problem of distinguishing these precipitates from ceramic particles formed on cool-down also arises. For this reason, image analysis of the ceramic phase fraction in the post-test micrographs can be performed that allows to determine what part of the observed ceramic precipitates was formed at test temperature [5].

The visual analysis of the post-test melt appearance in the CORA-W1 test shows that at low elevations (e.g. 374 mm, Fig. II-23) where the melt was formed (or relocated) at a late stage of the test (and thus was oxidised for a shorter period of time), it consists mainly of pure metal U-Zr-O melts with low oxygen contents that decompose on cool-down into mixtures of U-modified α-Zr(O) and $(U,Zr)O_2$ phases with a relatively low fraction of dark ceramic phase. Along the periphery uniform ZrO_2 oxide (or, possibly, mixed oxide $(U,Zr)O_2$ with a small content of U) layers confine the melts.

At higher elevations (e.g. 605 mm of CORA-W2 test bundle, Fig. II-24) oxidation time of the melt was longer and oxygen content varies at different positions from relatively low (Position 2) to relatively high (Position 3), as can be recognised by an increasing amount of dark ceramic $(U,Zr)O_2$ phase. As in Fig. II-23, the peripheral oxide layer consists of the ZrO_2 phase (Position 1).

At the elevations 845 mm (Fig. II-25) and 950 mm (Fig. II-26) of CORA-W2 test bundle corresponding to the bundle hot zone [16], the melt oxidation time was the largest and for this reason, the non-relocated melt was extensively converted into ceramic $(U,Zr)O_2$ phase which forms at these elevations a relatively uniform zones (Positions 1 and 2 in Fig. II-25 and Position 2 in Fig. II-26). A clear separation between a peripheral ZrO_2 layer and $(U,Zr)O_2$ zone formed by progressive growth of the bulk ceramic precipitates, can be distinguished in Figs. II-25 and II-26.

More detailed (EDX) data on the chemical composition of the $(U,Zr)O_2$ ceramic zones additionally analysed in [6] give evidence that the U/Zr ratio is quite uniform across the precipitation zone. This confirms that convective stirring of the melt took place in the melts as was observed also in the UO_2 crucible tests [5].

Therefore, on the basis of these CORA tests observations a conclusion may be derived that the peripheral oxide layer and bulk $(U,Zr)O_2$ precipitates (converting into uniform ceramic zone at a late stage) are the main oxidation products of the convectively stirred U-Zr-O melts.

6. Model for U-Zr-O melt oxidation

The one-dimensional model for the Zr-O melt oxidation presented in section 4, is generalised for the ternary U-Zr-O system in the current section.

Schematic representation of the layered structure in Fig. II-10 can be applied also to the present case with additional consideration of the new (U) component. It is assumed that the temperature T_I at the solid/liquid interface is different from the temperature T_B in the bulk of the melt stirred by the natural convection. In accordance with the ternary phase diagram (schematically presented in Fig. II-27), the corresponding concentrations at the interface: $c_O(I)$, $c_{Zr}(I)$ and $c_U(I)$, and in the melt bulk $c_O(B)$, $c_{Zr}(B)$ and $c_U(B)$, are different, also after attainment of bulk saturation. Temperature and concentration drops occur in a thin transition layer δ at the interface.

The interface concentrations in the melt belong to the liquidus line and thus obey an additional relationship:

$$F_{liq}\left(c_O(I), c_U(I), c_{Zr}(I)\right) = F_{liq}\left(c_O^*, c_U^*, c_{Zr}^*\right) = 0. \tag{30}$$

In the simplest approximation this equation can be linearised:

$$c_O(I) = g_1 + g_2 c_U(I), \tag{31}$$

where temperature dependent parameters $g_1(T_I)$ and $g_2(T_I)$ determine position of a straight (liquidus) line in the ternary phase diagram, Fig. II-27.

The molar density of the melt is assumed independent of the dissolved oxygen and is denoted by $c_M \approx 0.068$ mol/cm^3 on an oxygen-free basis [17]:

$$c_U + c_{Zr} = c_M. \tag{32}$$

The solidus line:

$$F_{sol}\left(\rho_O^*, \rho_U^*, \rho_{Zr}^*\right) = 0, \tag{33}$$

can be represented with a good accuracy as a straight line parallel to the U-Zr axis [6] in the ternary phase diagram (Fig. II-27), and thus can be described by the relationships:

$$\rho_U^* + \rho_{Zr}^* = \rho_S = const., \qquad \rho_O^* = const., \tag{34}$$

where ρ_S and ρ_O^* coincide with the corresponding values ρ_{Zr} and $\rho_O(I)$ in pure ZrO$_{2-x}$ phase.

The equilibrium tie-lines in the phase diagram connect points in the liquidus and solidus lines, therefore, they relate also the interface concentrations in the melt and solid phase. This means that composition of the solid ceramic phase near the interface can be different from pure ZrO$_{2-x}$ and contains an admixture of U cations, i.e. corresponds to the mixed ceramic phase (U,Zr)O$_{2-x}$.

It is straightforward to show that in the case of the oxide layer dissolution, the thickness of the interface boundary layer in the solid phase with the mixed composition (U,Zr)O$_{2-x}$ is extremely small (owing to a rather small diffusivity of cations in the ceramic phase which prevent them from deep penetration in the solid bulk), and therefore can be neglected in the mass balance and flux matching equations. In

this case an "effective" boundary concentration $\widetilde{\rho}_{Zr}$ equal to the bulk solid layer composition, i.e. pure ZrO$_2$ phase, should be used: $\widetilde{\rho}_{Zr} = \rho_S$.

However, in the case of oxide layer growth this boundary layer is not anymore small, since the oxide layer grows with the mixed composition (U,Zr)O$_{2-x}$ that is in equilibrium with the U containing melt at the interface. In this case the real boundary concentration, which is determined by intersection of the equilibrium tie-line with the solidus line, should be used in the mass transfer equations: $\widetilde{\rho}_{Zr} = \rho^*_{Zr}$.

The tie-lines that connect equilibrium concentrations at the interface, for simplicity, can be considered as straight lines starting from the O apex in the ternary phase diagram, as shown in Fig. II-27 by dotted lines, i.e.

$$\frac{\rho^*_{Zr}}{\rho_S} = \frac{c^*_{Zr}}{c_m}. \tag{35}$$

Such a simplification can be easily avoided if more accurate equations for the tie-lines are available.

6.1. Saturation stage

In this approximation for the tie-lines, the system of equations for the mass transfer in the first, saturation stage in a more general formulation (applicable either to plane, $L = 1$, or to cylindrical, $L = 2$, geometry) takes the form:

- Mass balances

$$D_O^{ZrO_2} \left.\frac{\partial \rho_o}{\partial r}\right|_I r_1^{L-1} - \rho_O(I)\left[r_2^{L-1}\frac{dr_2}{dt} - r_1^{L-1}\frac{dr_1}{dt} \right] = \frac{1}{L}\frac{d}{dt}\left[c_O(B)r_1^L \right], \tag{36}$$

$$-\widetilde{\rho}_{Zr}\left[r_2^{L-1}\frac{dr_2}{dt} - r_1^{L-1}\frac{dr_1}{dt} \right] = \frac{1}{L}\frac{d}{dt}\left[c_{Zr}(B)r_1^L \right], \tag{37}$$

$$-\rho_S\left[r_2^{L-1}\frac{dr_2}{dt} - r_1^{L-1}\frac{dr_1}{dt} \right] = \frac{c_M}{L}\frac{dr_1^L}{dt}. \tag{38}$$

where r_1 and r_2 are positions of the inner and outer boundaries of the solid ZrO$_2$ layer as schematically shown in <u>Fig. II-28</u>.

In accordance with the above presented explanation, the "effective" boundary concentration $\widetilde{\rho}_{Zr}$ of Zr in the solid phase is different for various regimes and can be represented in the form:

$$\widetilde{\rho}_{Zr} = \rho_S\left[1 - \left(1 - \frac{c_{Zr}(I)}{c_M} \right)\theta\left(\frac{d\left(r_2^L - r_1^L\right)}{dt} \right) \right], \tag{39}$$

which corresponds to $\widetilde{\rho}_{Zr} = \rho_S$ in the case of the oxide layer dissolution, when $\frac{d\left(r_2^L - r_1^L\right)}{dt} < 0$ and $\theta\left(\frac{d\left(r_2^L - r_1^L\right)}{dt} \right) = 0$, and to the mixed composition determined by Eq. (34), $\widetilde{\rho}_{Zr} = \rho_S\frac{c_{Zr}(I)}{c_M}$ in the case of the oxide layer growth, when $\frac{d\left(r_2^L - r_1^L\right)}{dt} > 0$ and $\theta\left(\frac{d\left(r_2^L - r_1^L\right)}{dt} \right) = 1$.

- Flux matches

$$k_O\big(c_O(B) - c_O(I)\big) - c_O(I)\frac{dr_1}{dt} = -D_O^{ZrO_2}\left.\frac{\partial\rho_O}{\partial r}\right|_I + \rho_O(I)\left[\left(\frac{r_2}{r_1}\right)^{L-1}\frac{dr_2}{dt} - \frac{dr_1}{dt}\right],\qquad(40)$$

$$k_{Zr}\big(c_{Zr}(B) - c_{Zr}(I)\big) - c_{Zr}(I)\frac{dr_1}{dt} = \tilde{\rho}_{Zr}\left[\left(\frac{r_2}{r_1}\right)^{L-1}\frac{dr_2}{dt} - \frac{dr_1}{dt}\right],\qquad(41)$$

$$k_U\big(c_U(B) - c_U(I)\big) - c_U(I)\frac{dr_1}{dt} - = \big(\rho_S - \tilde{\rho}_{Zr}\big)\left[\left(\frac{r_2}{r_1}\right)^{L-1}\frac{dr_2}{dt} - \frac{dr_1}{dt}\right],\qquad(42)$$

where k_{Zr} and k_U are convection mass transfer coefficients of Zr and U atoms in the melt that, due to Eq. (32) obey the relationship:

$$k_{Zr}\big(c_{Zr}(I) - c_{Zr}(B)\big) = -k_U\big(c_U(I) - c_U(B)\big).\qquad(43)$$

The system of Eqs. (36)–(42) completely determines melt oxidation in the saturation stage and can be analysed numerically.

6.2. Precipitation stage

The saturation stage of the oxidation process proceeds until saturation of the melt is reached. In the precipitation stage the oxygen flux to the melt continues due to the temperature and concentration drops in the transition layer, leading to oversaturation of the melt and onset of precipitation.

The $(U,Zr)O_2$ precipitates are in a local thermodynamic equilibrium with the surrounding melt, therefore, their composition belongs to the solidus line, Eqs. (34), and relates to the bulk composition of the melt at temperature T_B by the equilibrium tie-line equation, Eq. (35).

In this case the system of governing equations takes the form:

- Mass balances

$$D_O^{ZrO_2}\left.\frac{\partial\rho_O}{\partial r}\right|_I r_1^{L-1} - \rho_O(I)\left[r_2^{L-1}\frac{dr_2}{dt} - r_1^{L-1}\frac{dr_1}{dt}\right] = \frac{1}{L}\frac{d}{dt}\left[\big(c_O^*(1-f) + f\rho_O^*\big)r_1^L\right],\qquad(44)$$

$$-\tilde{\rho}_{Zr}\left[r_2^{L-1}\frac{dr_2}{dt} - r_1^{L-1}\frac{dr_1}{dt}\right] = \frac{1}{L}\frac{d}{dt}\left[c_{Zr}^*\left(1 - f\cdot\left(1 - \frac{\rho_S}{c_M}\right)\right)r_1^L\right],\qquad(45)$$

$$-\rho_S\left[r_2^{L-1}\frac{dr_2}{dt} - r_1^{L-1}\frac{dr_1}{dt}\right] = \frac{1}{L}\frac{d}{dt}\left[\big(c_M(1-f) + f\rho_S\big)r_1^L\right].\qquad(46)$$

- Flux matches

$$k_O\big[c_O^* - c_O(I)\big] - c_O(I)\frac{dr_1}{dt} = -D_O^{ZrO_2}\left.\frac{\partial\rho_O}{\partial r}\right|_I + \rho_O(I)\left[\left(\frac{r_2}{r_1}\right)^{L-1}\frac{dr_2}{dt} - \frac{dr_1}{dt}\right],\qquad(47)$$

$$k_U \left(c_U^* - c_U(I) \right) - c_{Zr}(I) \frac{dr_1}{dt} = \tilde{\rho}_{Zr} \left[\left(\frac{r_2}{r_1} \right)^{L-1} \frac{dr_2}{dt} - \frac{dr_1}{dt} \right],$$ (48)

$$- c_M \frac{dr_1}{dt} = \rho_S \left[\left(\frac{r_2}{r_1} \right)^{L-1} \frac{dr_2}{dt} - \frac{dr_1}{dt} \right].$$ (49)

where the bulk values c_O^*, c_U^*, c_{Zr}^* and ρ_O^*, ρ_U^*, ρ_{Zr}^* obey Eqs. (31), (34) and (35) with parameters $g_1(T_B)$ and $g_2(T_B)$ determined at the melt bulk temperature T_B.

The system of Eqs. (44)–(49) completely determines melt oxidation in the precipitation stage and can be analysed numerically.

In order to apply the new model to the quantitative interpretation of the bundle tests with UO$_2$ pellets, one should combine in a self-consistent manner the new oxidation model with the UO$_2$ dissolution model that is currently under development in the other JRC/IBRAE task (WP7.3) of the COLOSS Project.

Preliminary analysis performed in the Interim Report [1] allowed some qualitative conclusions. An important model prediction deduced for the binary Zr-O system concerning dissolution of the ceramic phase by saturated melts, can also be extended to the case of UO$_2$ dissolution. Similarly to Eq. (22), dissolution of UO$_2$ by the melt can be strongly increased under conditions of different temperatures in the fuel pellet and surrounding U-Zr-O melt. Since fuel dissolution in this case is not anymore restricted by the melt saturation limit and actively proceeds in the oversaturated melt, such a behaviour in the bundle tests can be interpreted as early fuel liquefaction.

In this case, both processes of fuel dissolution and melt oxidation by steam will lead together to the enhanced oversaturation of the melt and to an increased rate of (U,Zr)O$_2$ ceramic phase precipitation.

In the current report some examples of calculations of oxidation of melt, which already contains dissolved U, will be presented. Since the melt saturation due to fuel pellet dissolution and melt oxidation is a relatively quick process (a few hundred seconds at 2100-2200°C), such calculations adequately describe long-term oxidation of the U-Zr-O melts.

6.3. Numerical calculations

In Fig. II-29 calculation results for three different compositions of melts in the same geometry of a large molten pool and with a relatively small temperature difference between solid and melt, are presented. One can see that with increase of U content in the melt the growth of the peripheral oxide layer is practically invariable, whereas precipitation rate noticeably decreases. In all considered cases solidification of melt is not completed within 3000 s.

Time period of complete solidification (mainly due to precipitation of ceramic (U,Zr)O$_{2-x}$ particles) is reduced to ≈ 1500 s, if temperature difference is increased up to 20 K (see Fig. II-30), nevertheless, is still large.

For comparison, preliminary calculations of melt behaviour in the real fuel rod geometry with a thin molten Zry layer (with account for fuel pellet dissolution during the first 250 s until melt saturation is attained) by coupling of the new model with the UO$_2$ dissolution model (under development in task WP7.3), are presented in Fig. II-31. Under similar (to Fig. II-29) temperature conditions (T = 2473 K, ΔT = 6 K)

complete solidification of the melt in this case occurs within ≈ 600 s, due to the oxide layer growth and formation of mixed oxide $(U,Zr)O_{2-x}$ layer as observed in the CORA tests, Figs. II-25 and II-26. This time is much smaller in comparison with the molten pool oxidation time, owing to a much smaller value of the volume to surface (V/S) ratio. This important conclusion will be used for interpretation of the Phebus FPT0 test in the following section.

7. Preliminary analysis of oxidation of U-Zr-O melts in Phebus FPT0 test

Partial analysis of the available post-test images of the re-solidified U-Zr-O melts in the FPT0 test [18] can be performed analogously to the CORA tests (section 5). For this purpose zone 5 (from 75 to 100 cm) of the FPT0 bundle will be considered. In this zone temperatures were apparently lower than in the bundle hottest zone and for this reason, degraded fuel rods partially remained.

From Fig. II-32 one can see that fuel pellets at level +940 mm were strongly attacked by the melt and partially dissolved. Post-test EPMA X-Ray analysis [18] shows that composition of porous structure in Fig. II-32 is rather homogeneous: U (80-82 wt.%), Zr ($\sim$ 5 wt.%), O ($\sim$11 wt.%), and roughly corresponds to the mixed $(U,Zr)O_2$ ceramic phase (with a small admixture of Fe atoms). Since only one phase with the indicated composition was detected in these EPMA observations and no admixture of α-Zr(O) phase in this microstructure was reported in [18] (compare, for example, with the majority of microphotographs in the crucible and bundle tests presented in the current report where coexisting ceramic and α-phase are clearly seen and their composition were directly measured by the same X-Ray analysis method), a conclusion can be derived that the purely ceramic phase forms "foaming corium" in the considered cross-section.

On the other hand, relatively thin (several hundreds μm) oxide layers were detected mainly along the periphery of the bundle, largely open to the central direction. This allows the following interpretation of all these observations, on the base of the developed model consideration.

The U-Zr-O melt (with admixture of Fe atoms from molten stainless steel cladding of absorber rods) formed in the course of Zry cladding melting and UO_2 dissolution, was agglomerated in a large molten pool, extended across the whole bundle cross-section at this elevation and confined by the peripheral oxide layer. A similar behaviour of the melt shortly after its emergence was apparently observed in the "snap-shots" of molten pools in the QUENCH tests presented in section 5. Similarly to the above analysed QUENCH and CORA tests, a steep temperature gradient in the axial direction of fuel rods could lead to crust formation at a cooler bundle elevation that prevented this molten pool from quick downward relocation. In the course of a relatively slow relocation of this molten "slug", the melt was vigorously oxidised by steam and ceramic phase precipitates were formed as a result of simultaneous fuel dissolution and melt oxidation processes. When amount of ceramic phase in the slug exceeded some critical value, the ceramic particles stuck in-between fuel rods and formed some kind of solid debris, observed in Fig. II-32, whereas residual metallic melt continued its downward relocation along fuel rods, and so on. A similar process of ceramic debris formation was probably observed in the CORA tests at intermediate levels of the bundle, and was semi-quantitatively analysed in [13] by consideration of a similar mechanism of the molten slug relocation.

Therefore, it is natural to assume that the melt oxidation and ceramic particles formation can be described by the new oxidation/dissolution mechanism considered in the current report. Since the new melt oxidation model predicts an enhanced oxidation rate of molten materials, one could expect an improved description of oxidation and hydrogen generation as well as of fuel dissolution that are generally under-estimated by code calculations [18].

Besides, this mechanism additionally provides a natural explanation of the observed early fuel destabilisation/relocation of the upper part of the bundle (during the oxidation run-away) at a fuel temperature of about 2600 K [18], without additional assumption on the eutectic ceramic melt formation at such a low temperature. Indeed, as demonstrated in section 6.3, complete solidification of relatively large molten pools can be readily avoided (due to a large *V/S* ratio) during 2-3 thousand seconds between metal cladding melting and onset of relocation (detected at ≈ 2600 K). In this case, depending on the temperature difference between solid and melt, vigorous fuel dissolution and melt oxidation in the pool take place and result in a strong precipitation of ceramic phase and corresponding increase of melt effective viscosity. In its turn, this can explain a rather slow relocation (rather than instantaneous slumping) of the slug formed by heavily oversaturated and precipitated melt, in a qualitative agreement with the analysis of the temperature measurements in the bundle and shroud [18]. In this situation a close analogy with a slow melt relocation revealed in the CORA tests [14] and analysed in [13], can be derived.

8. Conclusions

- Detailed analysis of post-test images of re-solidified Zr-O melts in the QUENCH-02 and 03 tests is performed. A close similarity with the melt appearance in the ZrO_2 crucible dissolution tests where oxide layer growth was accompanied by precipitation of ceramic particles in the corrosion (oxidation) stage of the tests, is confirmed.

- On this basis, the new model for Zr-O melt oxidation under conditions of convection stirring was developed. The model explains the emergence of the ceramic precipitates induced by the temperature difference between solid and liquid materials, and predicts continuous oxidation/precipitation process after attainment of the saturated state of the melt.

- The model was successfully validated against previous AECL and new FZK tests on ZrO_2 crucible dissolution by molten Zry. The new model predictions concerning long-term behaviour in the oxidation stage of the tests (i.e. cessation of the oxide layer growth and commencement of its renewed dissolution) were confirmed by the new FZK test results.

- The model predicts a linear or close to linear time law for the rate of the ZrO_2 ceramic phase (oxide layer + precipitates) growth during Zr melt oxidation that corresponds to a much faster kinetics of Zr oxidation and hydrogen generation in comparison with the standard (parabolic) rate. Numerical calculations of the model allow quantitative interpretation of the vigorous melt oxidation and ZrO_2 phase precipitation observed in the QUENCH tests.

- Post-test images of re-solidified U-Zr-O melts in the CORA-W1 and W2 tests are additionally analysed. A behaviour of the ternary U-Zr-O melts similar to the previous case (i.e. continuous oxidation of oversaturated melts accompanied with precipitation of ceramic $(U,Zr)O_2$ phase) is revealed also in these tests.

- Correspondingly, the new model is generalised for description of the ternary U-Zr-O melt oxidation and analysed. The main qualitative conclusion on the enhanced kinetics of melt oxidation and hydrogen generation is confirmed also for the ternary system. Numerical calculations of the model allows quantitative interpretation of the vigorous melt oxidation and $(U,Zr)O_2$ phase precipitation observed in the CORA tests.

- On the basis of the analysis performed for the binary Zr-O system behaviour (i.e. solid ZrO_2 and Zr-O melt), it is anticipated that dissolution of UO_2 fuel by the U-Zr-O melt is also strongly influenced by the temperature difference between heated fuel pellets and melt. In this case dissolution is no longer restricted by the melt saturation limit and may proceed actively in the oversaturated melt. Such behaviour in the bundle tests can be interpreted as early fuel liquefaction.

- The new mechanism provides a natural qualitative explanation of the early fuel destabilisation/liquefaction and enhanced melt oxidation accompanied with the ceramic phase precipitation, observed in the Phebus FPT0 test. Implementation of this mechanism in the fuel dissolution model (that is currently under development in the other JRC/IBRAE task of the COLOSS Project) for quantitative analysis of the bundle tests observations, is recommended.

Acknowledgements

Appendix

In order to describe diffusion mass transfer through the two-phase mixture (liquid + ceramic precipitates) in the temperature gradient, one can use a general approach of Flemings [19]. This approach is based on an assumption that the two phases are in local thermodynamic equilibrium in each spatial point of the two-phase zone, i.e. concentrations of liquid and solid phases, $c_O(x,t)$ and $\rho_O(x,t)$, are determined by the liquidus $c_{liq}(T)$ and solidus $\rho_{sol}(T)$ lines of the equilibrium phase diagram, respectively:

$$c_O(x,t) = c_{liq}(T(x,t)), \quad \rho_O(x,t) = \rho_{sol}(T(x,t)).$$ (A.1)

This approach can be also applied to description of molecular diffusion through the transition boundary layer with $\delta_d \approx \delta_t = \delta$, i.e. when the temperature and concentration drops occur in the same layer.

In this case mass transfer through the two-phase layer (either in liquid or in solid phases) occurs owing to the concentration gradient induced by the temperature profile.

Correspondingly, the diffusion equation in this layer takes the form:

$$\frac{\partial}{\partial t}\left[c_O(x,t)(1-f(x,t)) + \rho_O(x,t)f(x,t)\right] = \frac{\partial}{\partial x}\left[D_O^{liq}(1-f)\frac{\partial c_O}{\partial x} + D_O^{sol}f\frac{\partial \rho_O}{\partial x}\right],$$ (A.2)

Hence, the system of Eqs. (A.1) and (A.2) governs mass transfer through the two-phase zone in the predetermined temperature field.

This system can be simplified in the linear approximation for the temperature field (i.e. linear variation from T_I to T_B across the two-phase layer thickness δ) and for both liquidus and solidus lines. The last assumption corresponds fairly well to the real phase diagram, Fig. II-1. In this case both concentration fields $c_O(x,t)$ and $\rho_O(x,t)$ are also linear functions of spatial co-ordinate x according to Eq. (A.1):

$$c_O(x,t) \approx c_O(I) - \Delta c_O x, \quad \rho_O(x,t) \approx \rho_O(I) - \Delta \rho_O x,$$ (A.3)

where $\Delta c_O = c_O(I) - c_O^*$, $\Delta \rho_O = \rho_O(I) - \rho_O^*$.

Further simplification of the system can be performed in the steady-state approximation for the diffusion problem. In order to justify this approximation, one should show that the characteristic time $\tau_{dif} \sim \delta^2/D_O^{liq}$ of diffusion mass transfer through the two-phase layer thickness δ, is small in comparison with the characteristic growth times of precipitates and oxide layer, $\tau_{pr} \sim \dfrac{\delta}{\partial(f\delta)/\partial t}$ and

$\tau_{ox} \sim \dfrac{L}{\partial L/\partial t}$. Evaluation of τ_{pr} can be obtained from the conservative estimation

$(\rho_O - \bar{c}_O)\partial(f\delta)/\partial t \le D_O^{liq}(1-f)\Delta c_O/\delta$, where $\bar{c}_O = (c_O(I) + c_O^*)/2$, while τ_{ox} is conservatively evaluated from an inequality $(\rho_O - c_O(I))\partial L/\partial t \le D_O^{ZrO_2}\Delta\rho_O^{st}/L$, where $\Delta\rho_O^{st} = \rho_O^{(st)} - \rho_O(I)$ as defined in Fig. II-10. Substituting these values in the above-presented definitions of τ_{pr} and τ_{ox}, one can promptly acquire that

$$\tau_{dif} \ll \tau_{pr}\,, \qquad\qquad\qquad\qquad\qquad\text{if}$$

$$\frac{\left(\rho_O - \bar{c}_O\right)}{(1-f)\Delta c_O} \gg 1\,,$$

and

$$\tau_{dif} \ll \tau_{ox}\,, \qquad\qquad\qquad\qquad\qquad\text{if}$$

$$\frac{\left(\rho_O - \bar{c}_O\right)}{\Delta \rho_O}\frac{L}{\delta}\frac{D_O^{liq}}{D_O^{ZrO_2}} \gg 1\,.$$

Both inequalities are apparently valid due to the smallness of the values Δc_O, $\Delta \rho_O$ and δ/L. The second inequality can be additionally justified when the oxide layer growth is stabilised as described in section 4.2.1. Therefore, the steady-state approximation can be used searching for the solution of Eq. (A.2).

In this approximation one may equate the l.h.s of Eq. (A.2) to zero, hence, the equation takes the form:

$$\frac{\partial}{\partial x}\left[D_O^{liq}(1-f)\frac{\partial c_O}{\partial x} + D_O^{sol}f\frac{\partial \rho_O}{\partial x}\right] \approx 0\,. \tag{A.4}$$

Substitution of Eq. (A.3) in Eq. (A.4) yields:

$$\frac{\partial f}{\partial x} \approx 0\,, \tag{A.5}$$

i.e. the solid fraction in the layer can be considered as spatially uniform.

Eventually the system of flux matching equations takes the form:

$$-D_O^{ZrO_2}\frac{\partial \rho_O}{\partial x}\bigg|_I - \rho_O(I)\frac{\partial L}{\partial t} = \left[c_O(I)(1-f) + \rho_O(I)f\right]\cdot\left(u - \frac{\partial L}{\partial t}\right)$$

$$+ (1-f)\frac{D_O^{liq}\Delta c_O}{\delta} + f\frac{D_O^{ZrO_2}\Delta \rho_O}{\delta}\,, \tag{A.6}$$

$$-\rho_{Zr}(I)\frac{\partial L}{\partial t} = \left[c_{Zr}(I)(1-f) + \rho_{Zr}(I)f\right]\cdot\left(u - \frac{\partial L}{\partial t}\right) \tag{A.7}$$

References

1. M.S. Veshchunov, "U-O-Zr Oxidation Model", JRC Technical Note P.02.35, SAM-COLOSS-D26, Petten, September 2001.

2. P. Hofmann, L. Horn, W. Leiling, D. Piel, L. Schmidt, L. Sepold, M. Steinbrück, "QUENCH-02. Test Data Report", PSF3303, 1998.

3. P. Hofmann, C. Homann, L. Horn, W. Leiling, A. Miassoedov, D. Piel, L. Schmidt, L. Sepold, M. Steinbrück, "QUENCH-03. Test Data Report", PSF3316, 1999.

4. P. Hofmann, J. Stuckert, A. Miassoedov, M.S. Veshchunov, A.V. Berdyshev, A.V. Boldyrev, "ZrO_2 Dissolution by Molten Zircaloy and Cladding Oxide Shell Failure. New Experimental Results and Modelling", Report FZKA 6383, INV-CIT(98)-P026, Karlsruhe, Germany, 1999.

5. P.J. Hayward, P. Hofmann, J. Stuckert, M.S. Veshchunov, A.V. Berdyshev, "UO_2 Dissolution by Molten Zircaloy. New Experimental Results and Modelling", Report FZKA 6379, INV-CIT(99)-P029, Karlsruhe, Germany, 1999.

6. M.S. Veshchunov, A.V. Berdyshev, "Modeling of chemical interactions of fuel rod materials at high temperatures. Part 1: Simultaneous dissolution of UO_2 and ZrO_2 by molten Zircaloy in an oxidizing atmosphere", J. Nucl. Mater., 1997, v.252, p.98-109.

7. K.T. Kim and D.R. Olander, J. Nucl. Mater., 1988, v.154, p.102-115.

8. E.R. Eckert, R.M. Drake, "Analysis of Heat and Mass Transfer", McGraw-Hill, 1972.

9. W.M. Kays, M.E. Crawford, "Convective Heat and Mass Transfer", Third Edition, McGraw-Hill, 1993.

10. B. Adroguer et al., "Corium Interactions and Thermochemistry (CIT)", FISA 99, EU Research in Reactor Safety, Luxembourg, November 29 – December 1st, 1999

11. K.T. Kim and D.R. Olander, J. Nucl. Mater., 1988, v.154, p.85-101.

12. D.R.Olander, Nucl. Eng. Des., 1994, v.148, p.253.

13. M.S.Veshchunov, A.V.Palagin, "Modeling of chemical interactions of fuel rod materials at high temperatures. Part 2: Investigation of downward relocation of molten materials", J. Nucl. Mater., 1997, v.252, p.110-120.

14. V. Noack, S. Hagen, P. Hofmann, G. Schanz, and L. Sepold, "Material Distribution in LWR-type Bundles Tested Under Severe Accident Conditions," Nuclear Technology, 1997, v.117, p.158-170.

15. S. Hagen, P. Hofmann, V. Noack, G. Schanz, G. Schumacher and L. Sepold, "Test results of experiment CORA W1", KfK 5212, 1994.

16. S. Hagen, P. Hofmann, V. Noack, G. Schanz, G. Schumacher and L. Sepold, "Test results of experiment CORA W2", KfK 5363, 1994.

17. D.R.Olander, "Materials-Chemistry and Transport Modeling for Severe Accident Analysis in Light-Water Reactors", Lawrence Berkeley Laboratory Report LBL-32530 (1992).

18. N. Hanniet-Girault and G. Repetto, "FPT0 Final Report, Final Version", Phebus-PF, December 1998.

19. M.C. Flemings, "Solidification Processing", McGraw-Hill, New York, 1974.
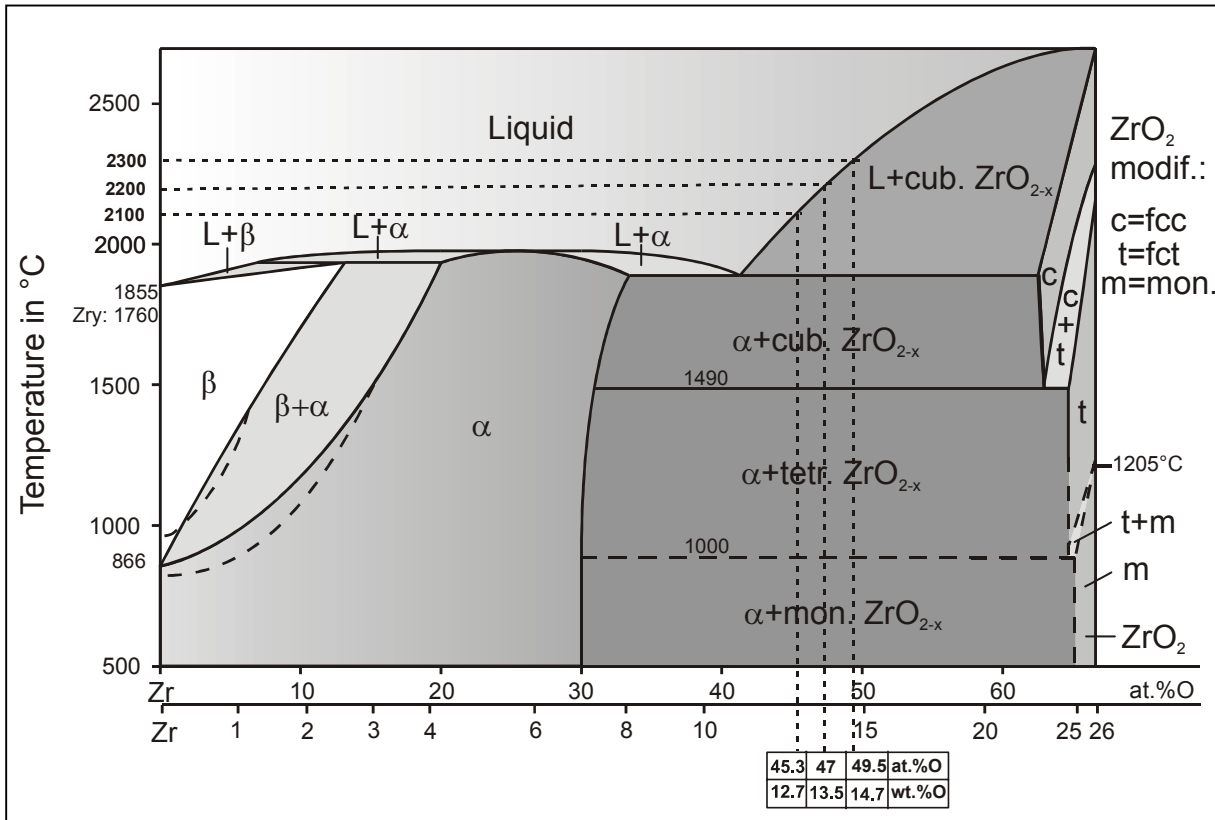
Fig. II-1: Equilibrium binary Zr-O phase diagram
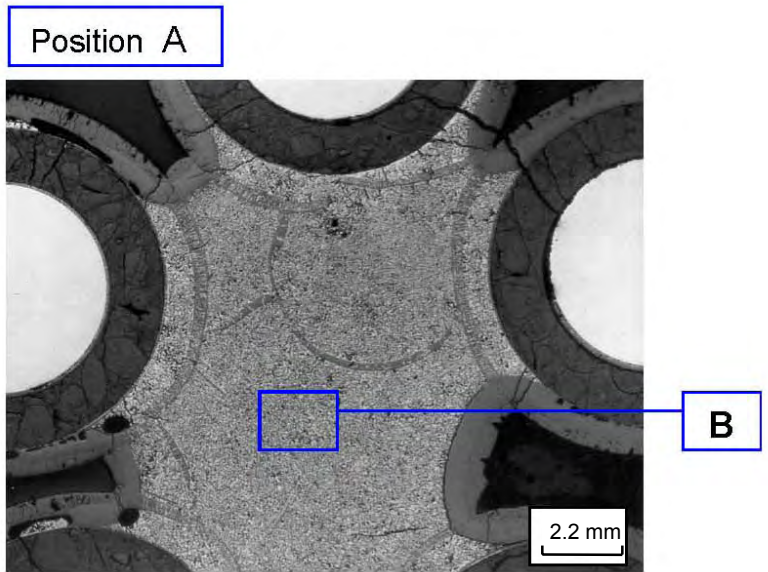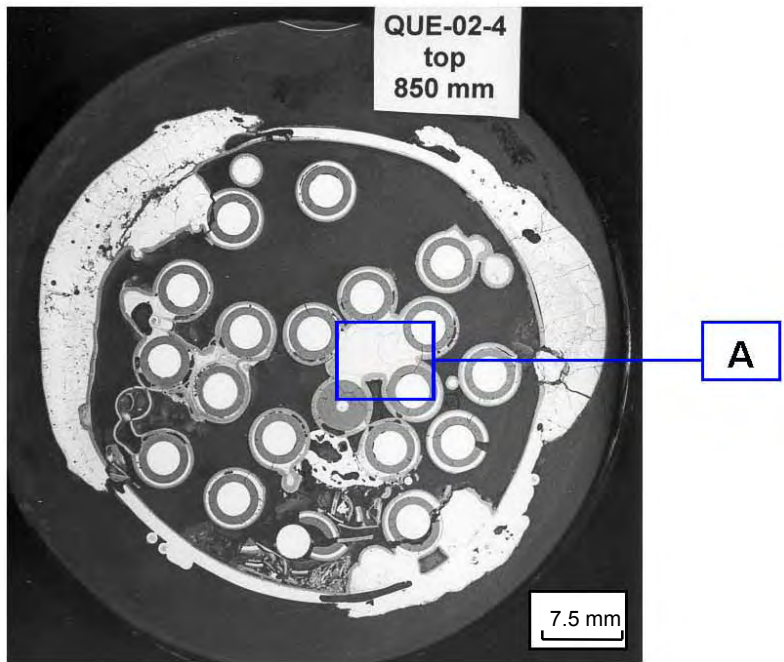
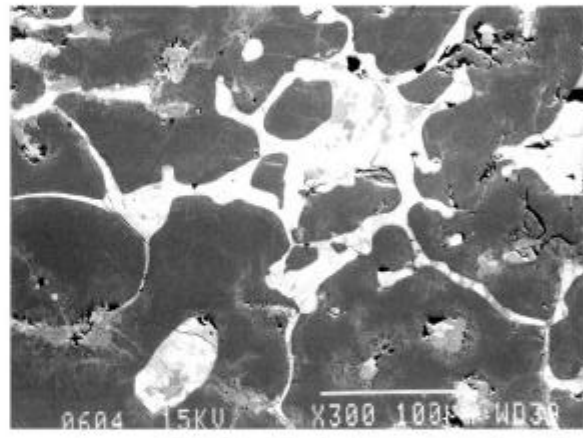**Fig. II-2a: Cross section Q-02-4 of QUENCH-02 test bundle (elevation 850 mm). General view and position A**

Position B

70 µm

C

Position C

25 µm
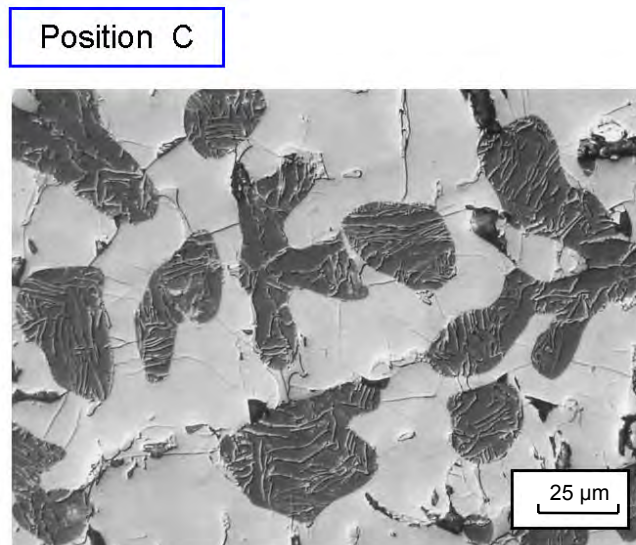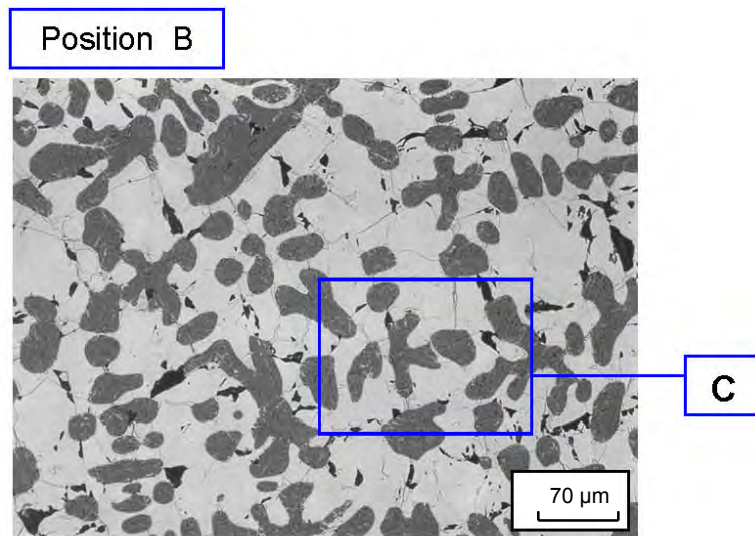
Fig. II-2b: Cross section Q-02-4 of QUENCH-02 test bundle. Positions B and C
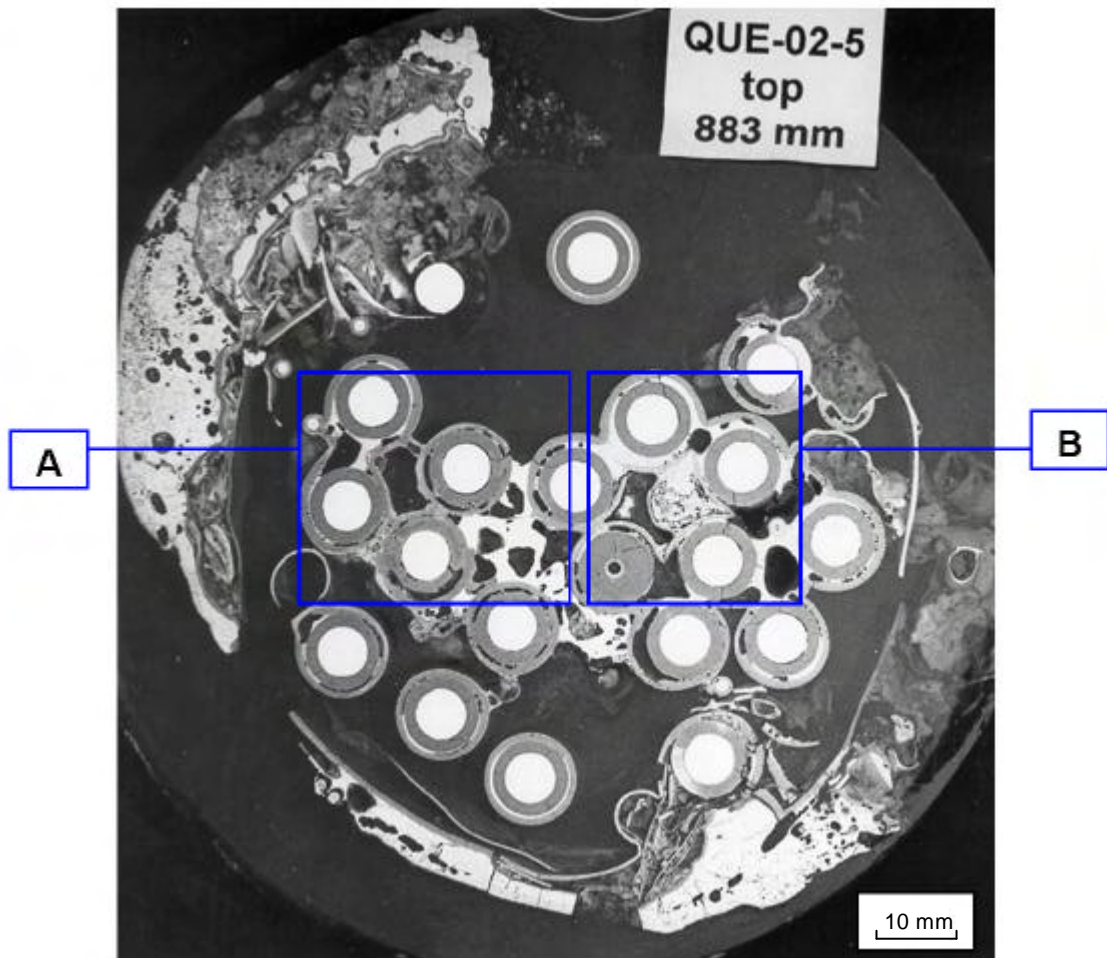
Fig. II-3a: Cross section Q-02-5 of QUENCH-02 test bundle (elevation 883 mm). General view
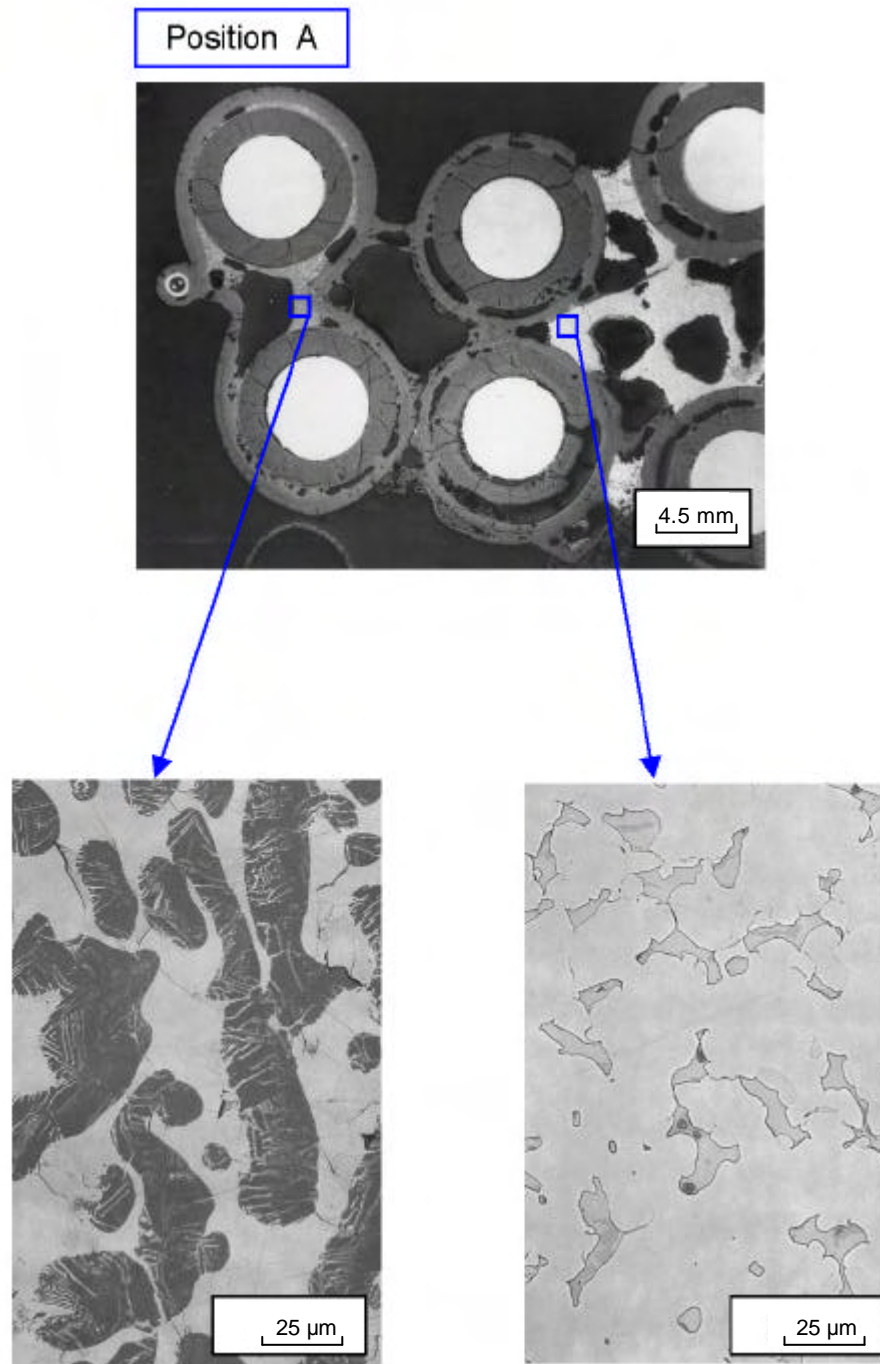
Fig. II-3b: Cross section Q-02-5 of QUENCH-02 test bundle. Position A
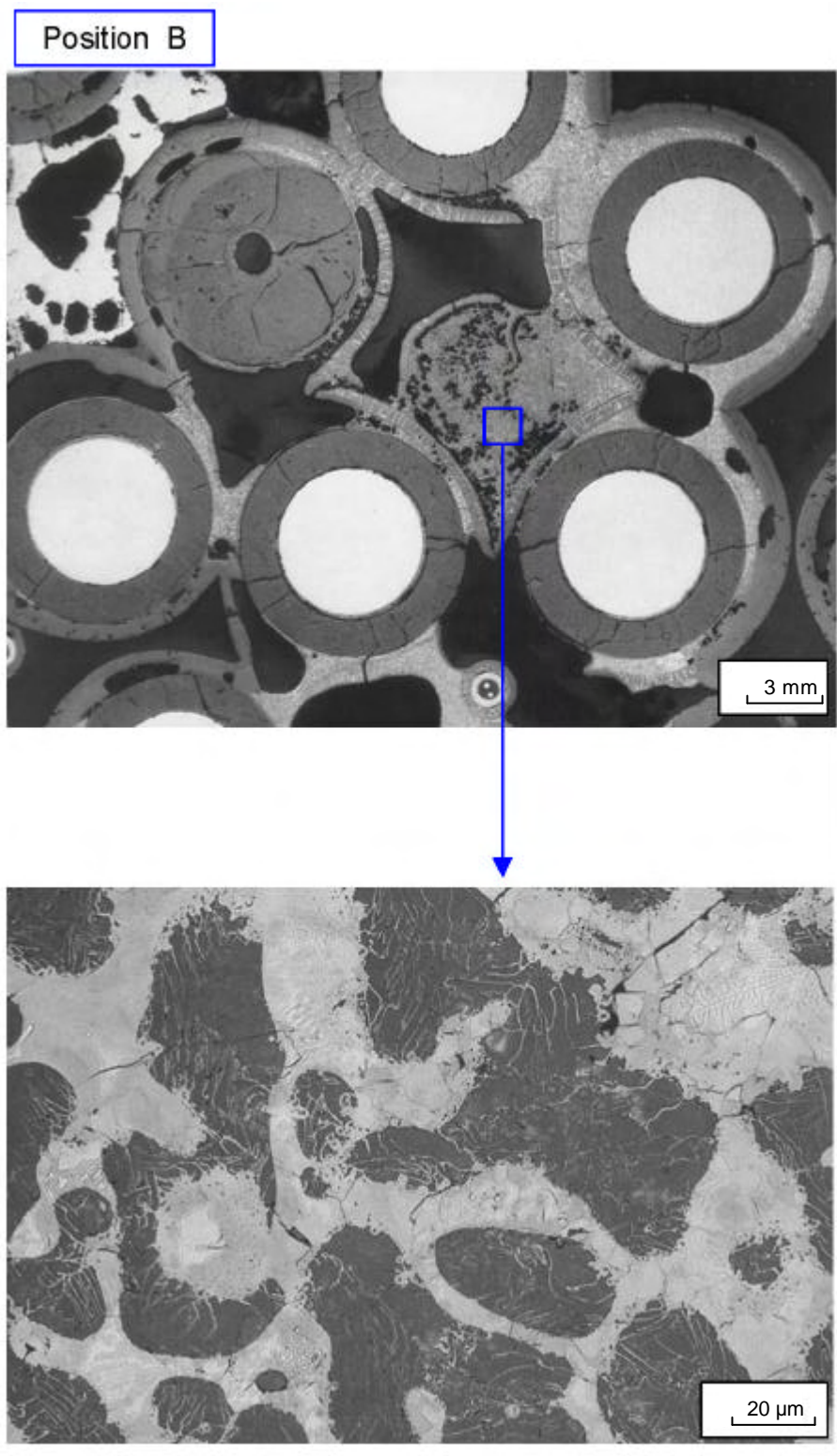
Fig. II-3c: Cross section Q-02-5 of QUENCH-02 test bundle. Position B
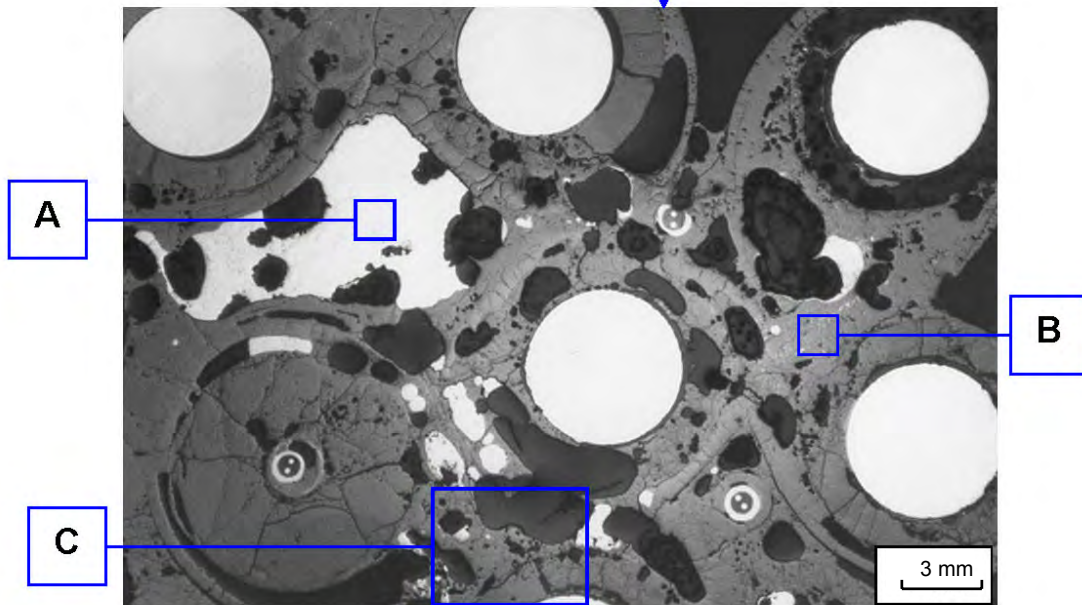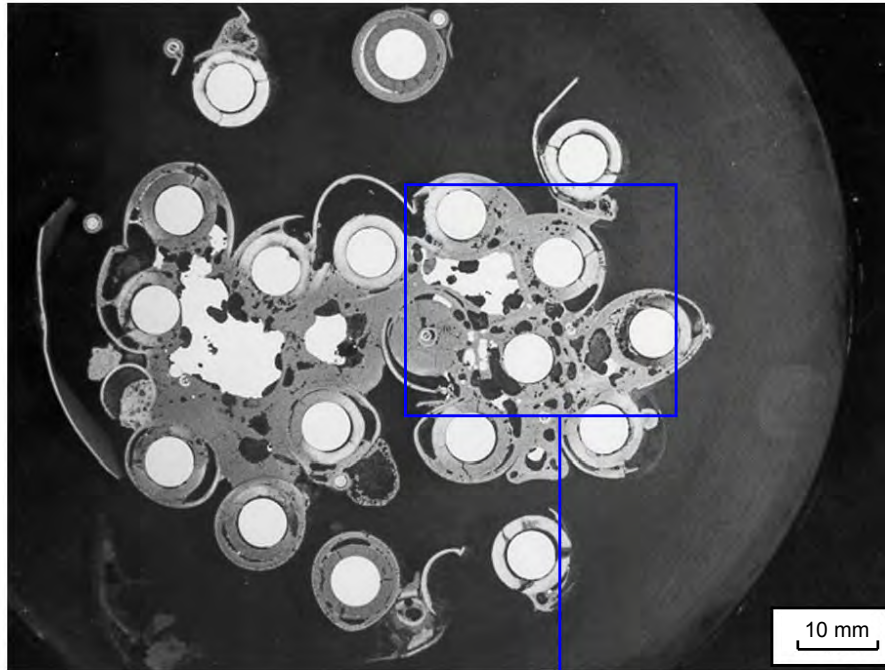
Fig. II-4a: Cross section Q-02-6 of QUENCH-02 test bundle (elevation 950 mm)
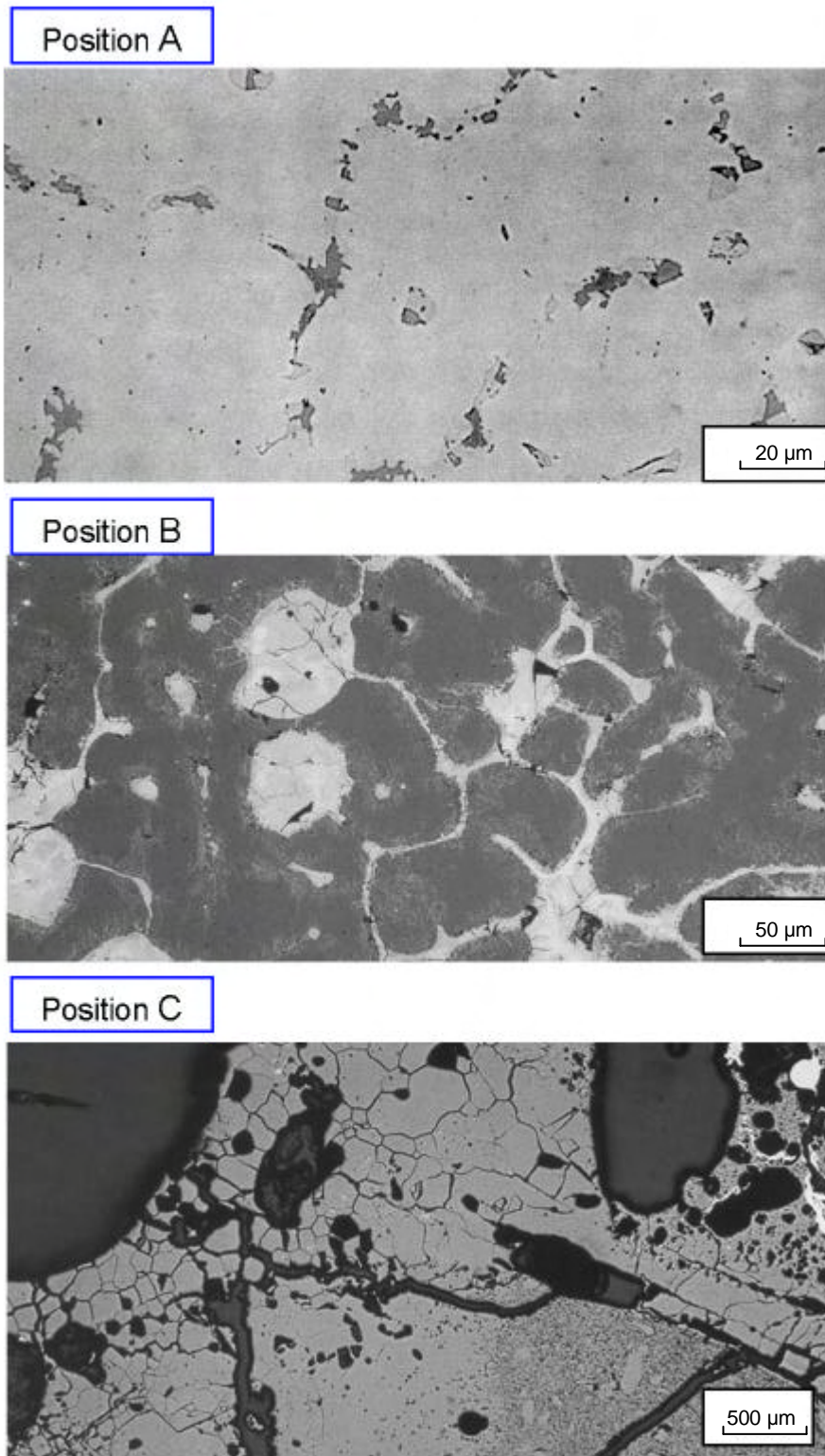
Fig. II-4b: Cross section Q-02-6 of QUENCH-02 test bundle. Positions A, B and C
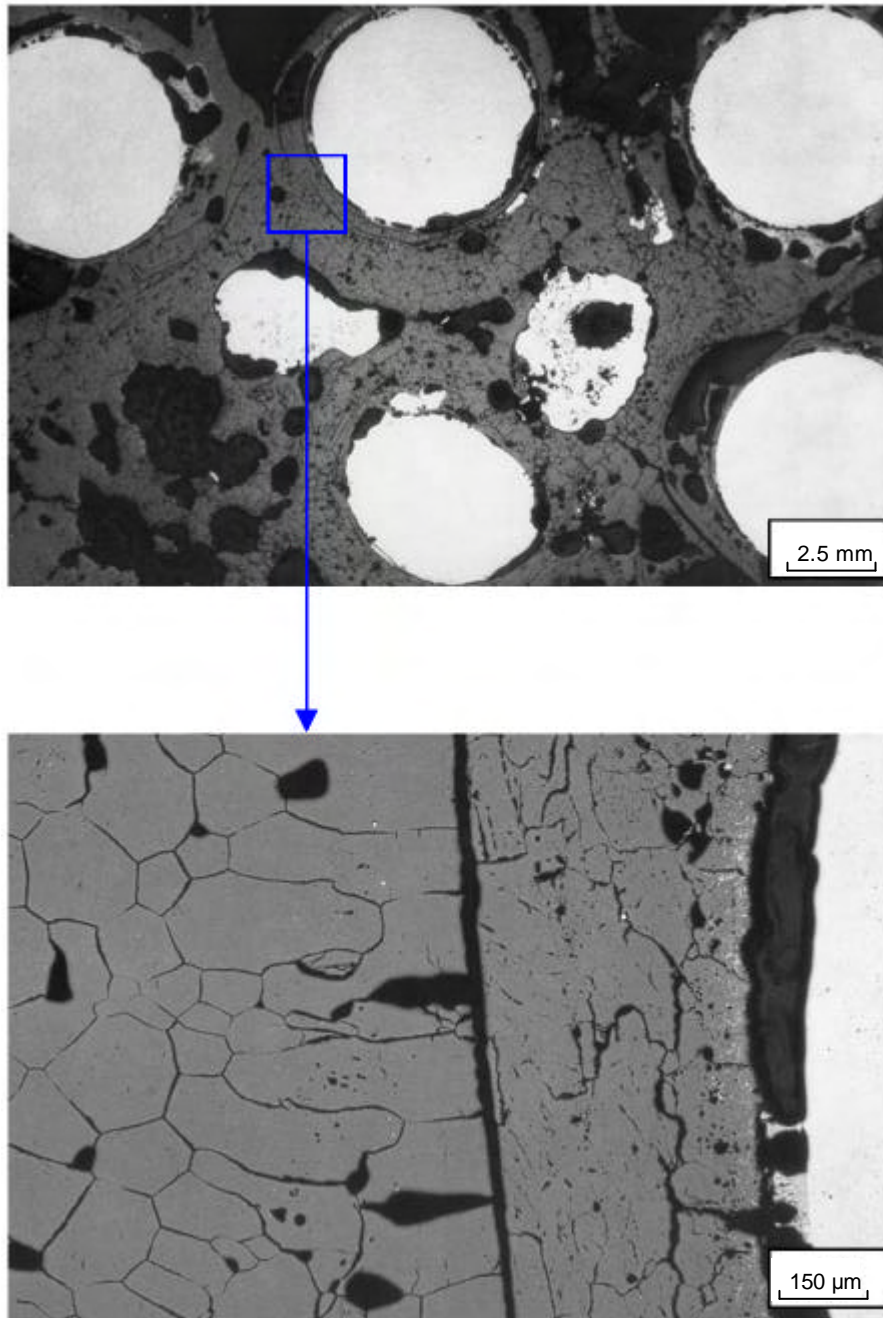
Fig. II-5: Cross section Q-02-7 of QUENCH-02 test bundle (elevation 1050 mm)
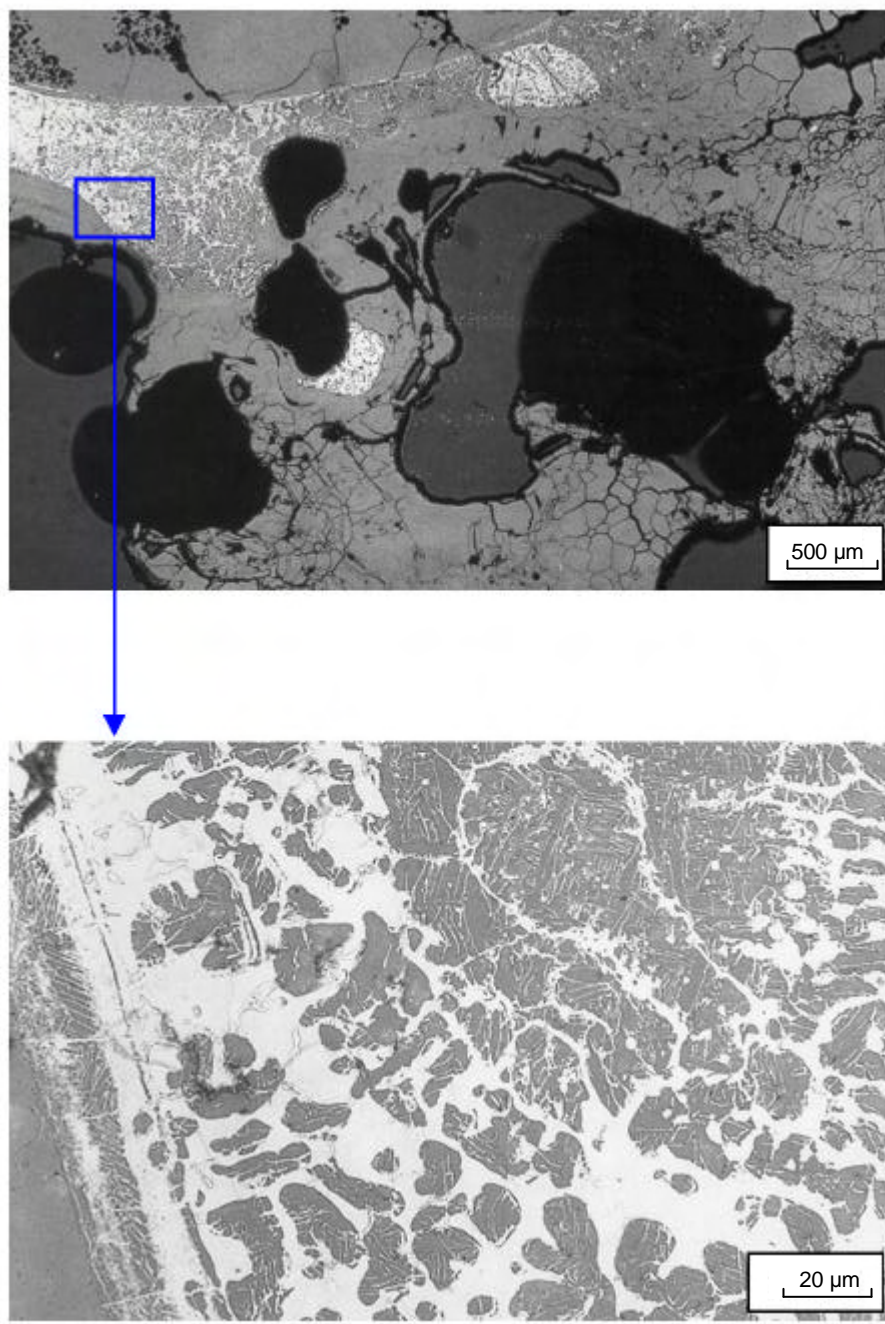
Fig. II-6: Cross section Q-03-5 of QUENCH-03 test bundle (elevation 750 mm)
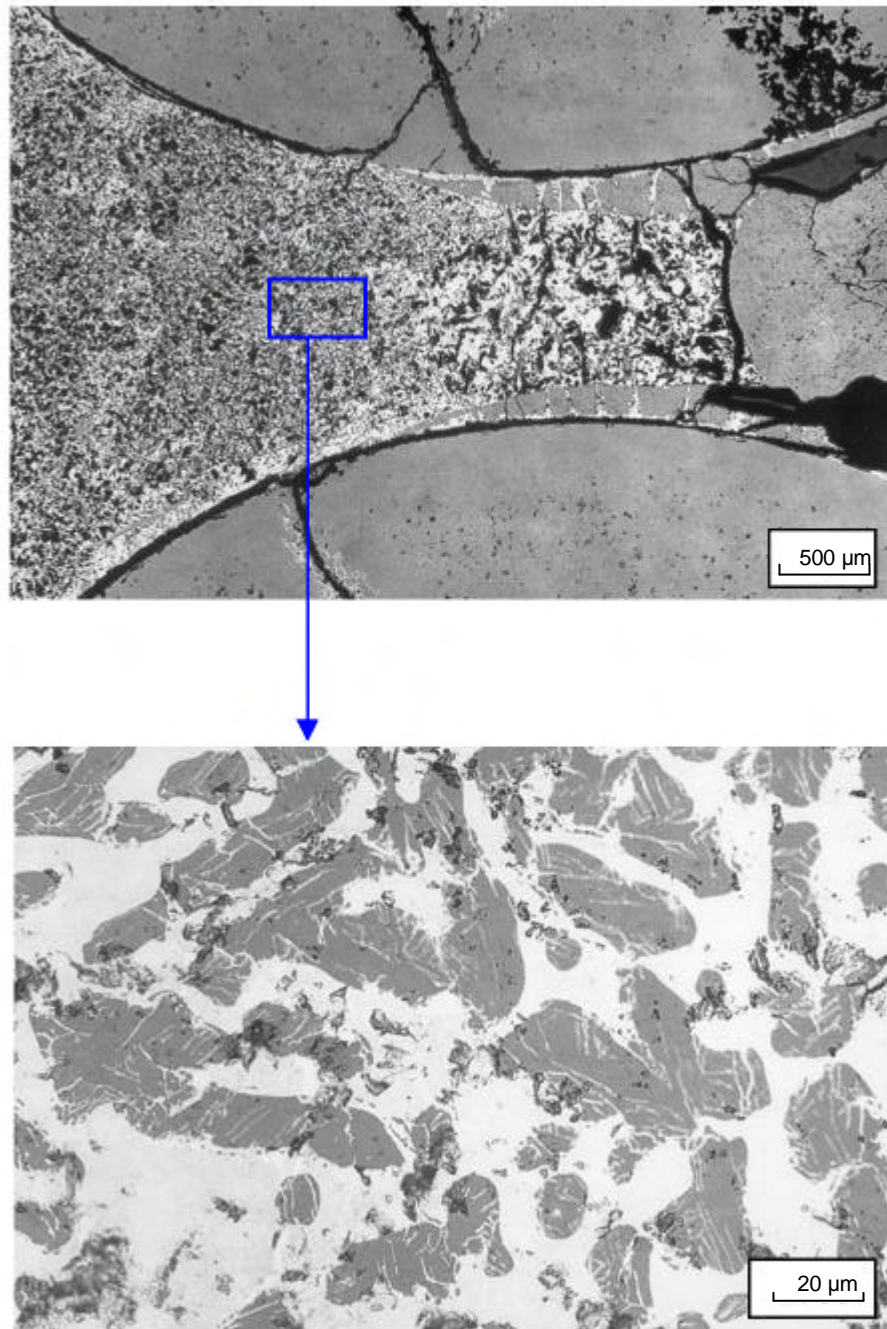
Fig. II-7a: Cross section Q-03-7 of QUENCH-03 test bundle (elevation 950 mm)
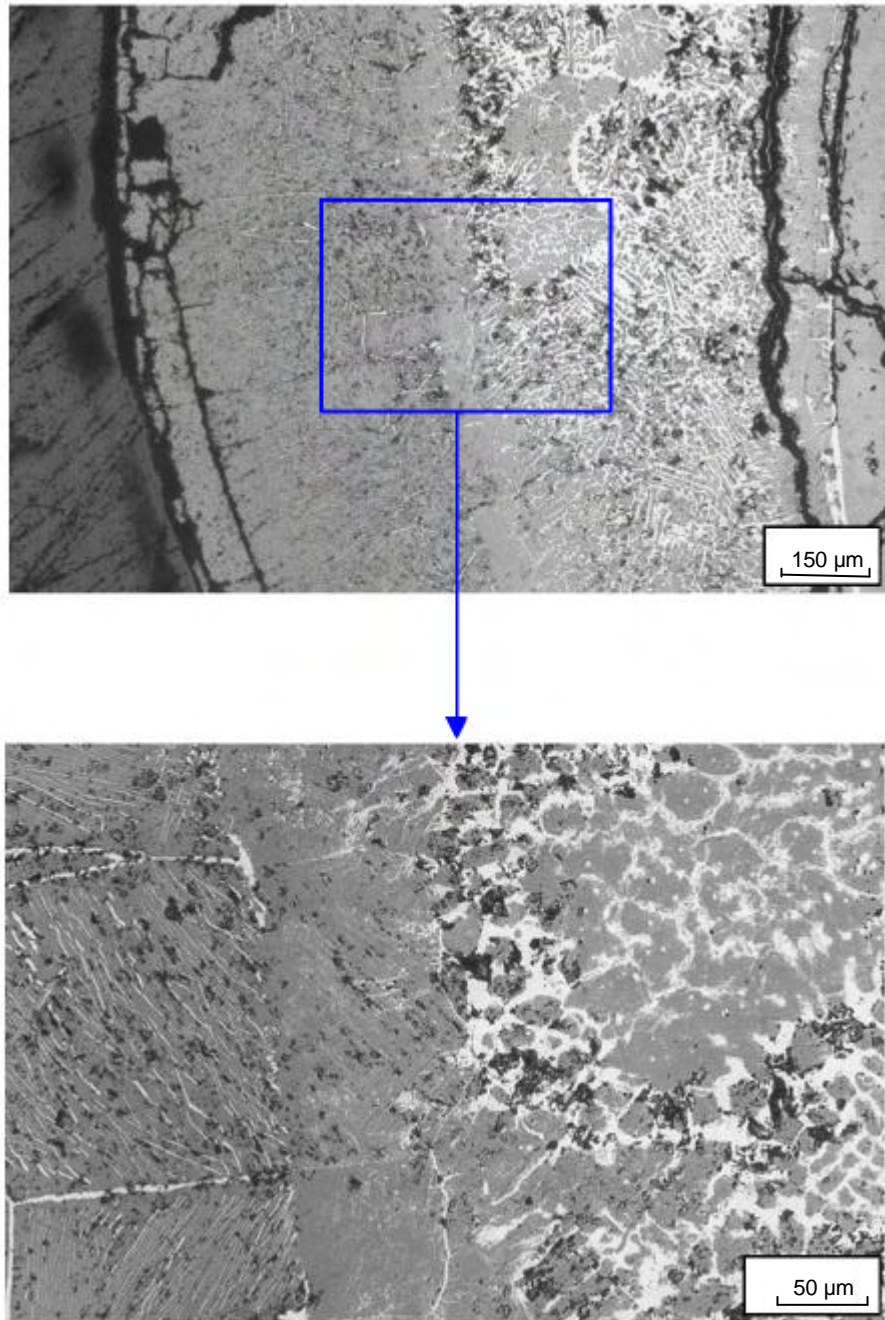
Fig. II-7b: Cross section Q-03-7 of QUENCH-03 test bundle (elevation 950 mm)
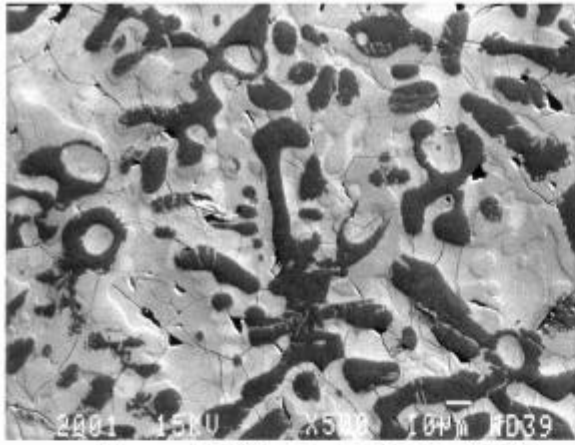
Integral EDX: **Zr:O=49:51 (at%)**
Image analysis: **Zr:O=54:46 (at%)**
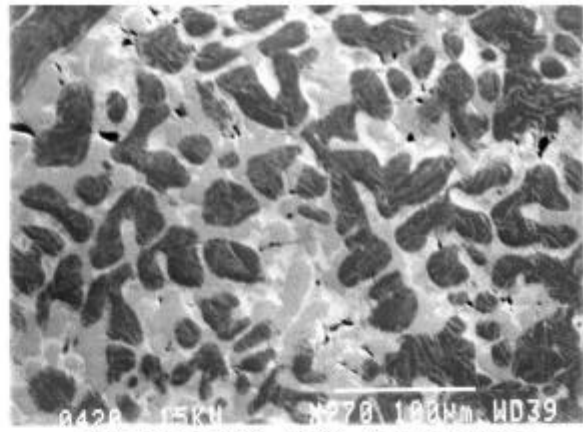
Integral EDX: **Zr:O=45:55 (at%)**
Image analysis: **Zr:O=48:52 (at%)**
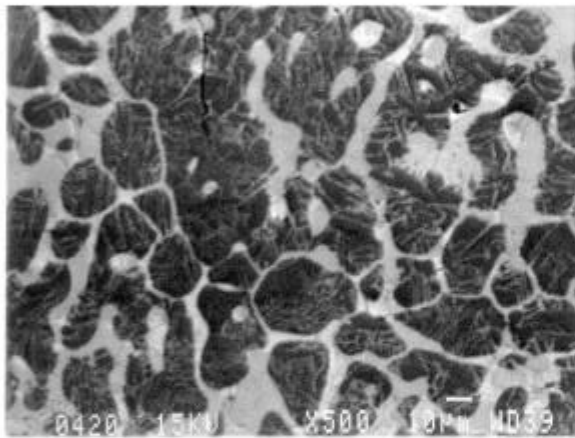
Integral EDX: **Zr:O=42:58 (at%)**
Image analysis: **Zr:O=43:57 (at%)**

Integral EDX: **Zr:O=36.5:63.5 (at%)**
Image analysis: **Zr:O=40:60 (at%)**
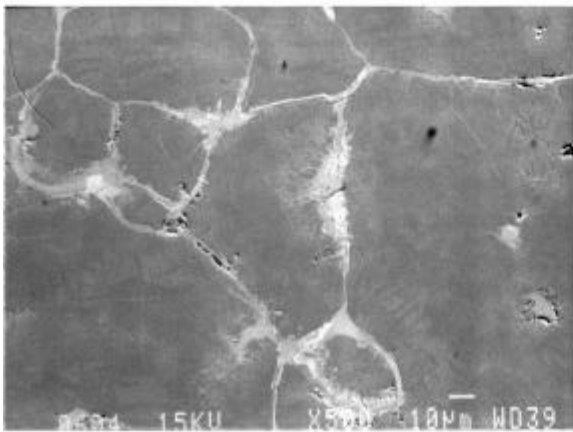
Integral EDX: **Zr:O=35:65 (at%)**
Image analysis: **Zr:O=36:64 (at%)**
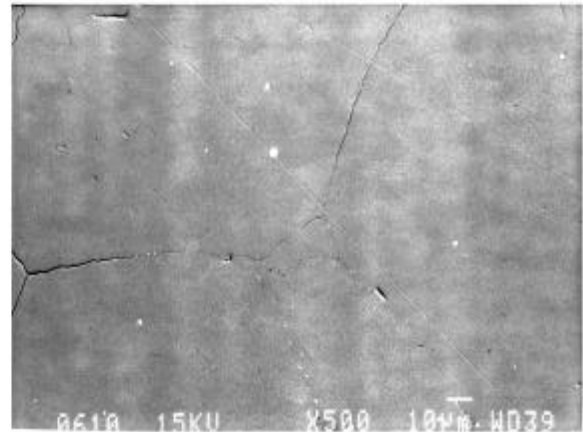
Integral EDX: **Zr:O=32:68 (at%)**

**Fig. II-8: EDX and image analyses of solidified melts at different positions of
QUENCH-02 test bundle cross sections**

70

5 mm

100 μm

Image analysis results

↓

Zr:O= **49.8:50.2** at%

KfK LV123; melt duration 600 s

Zr:O= **46.6:53.4** at%

KfK LV132; melt duration 3600 s

Zr:O= **41:59** at%

KfK LV134; melt duration 7200 s
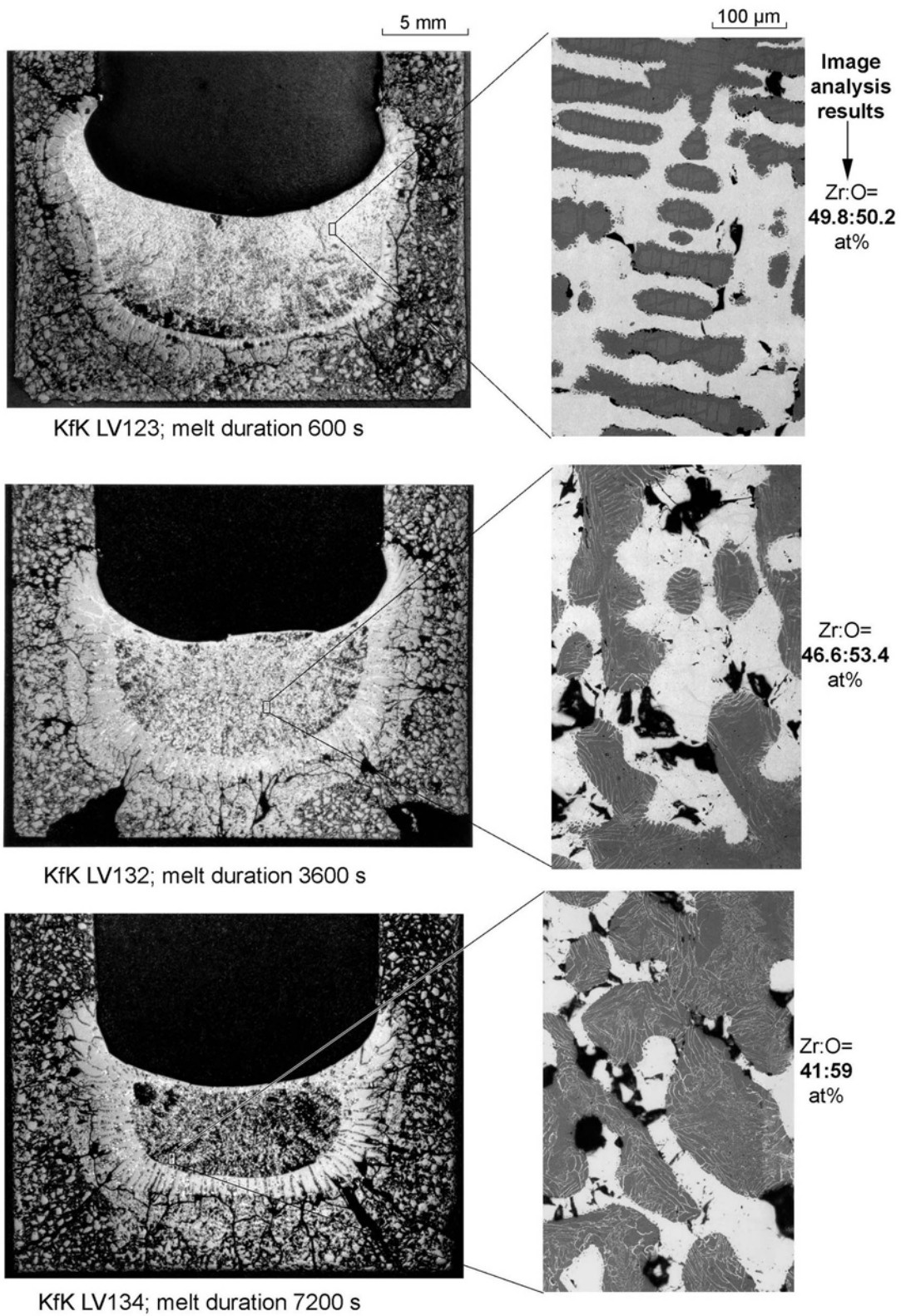
Fig. II-9: Cross sections of ZrO$_2$ crucibles with Zry charge in KfK dissolution tests at 2200°C
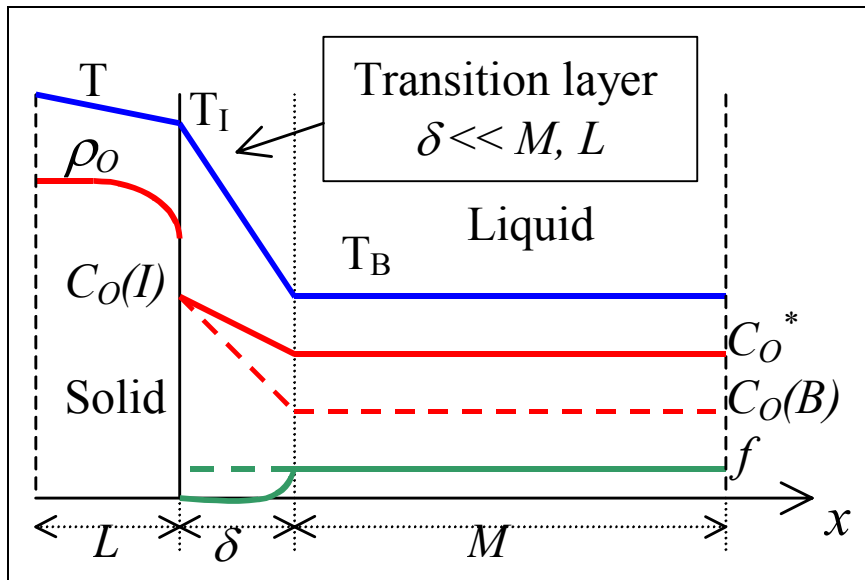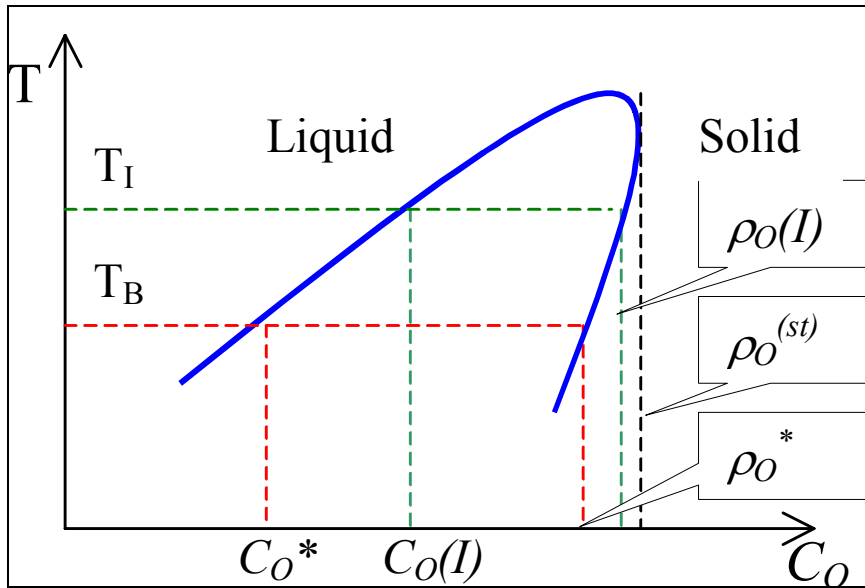
Fig. II-10: Schematic representation of the model
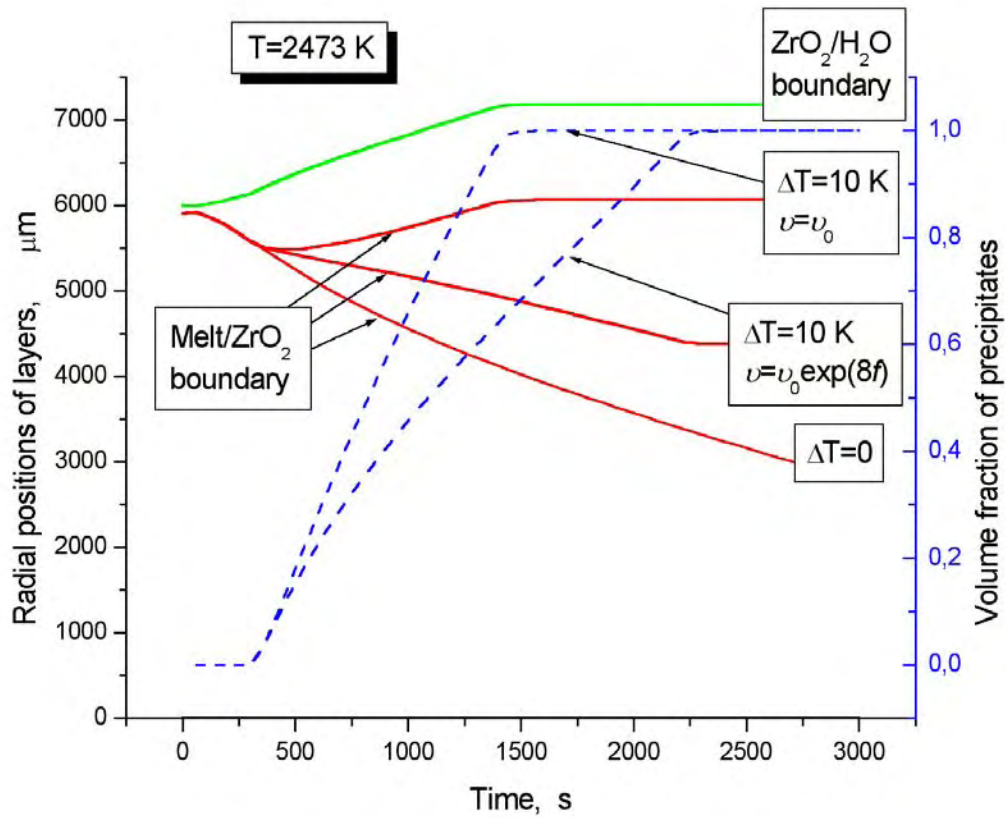
Fig. II-11: Growth of oxide layer and precipitates for different parameters of melt oxidising in steam at 2473 K

solid curves – dissolved wall thickness;
dashed curve – volume fraction of precipitates.
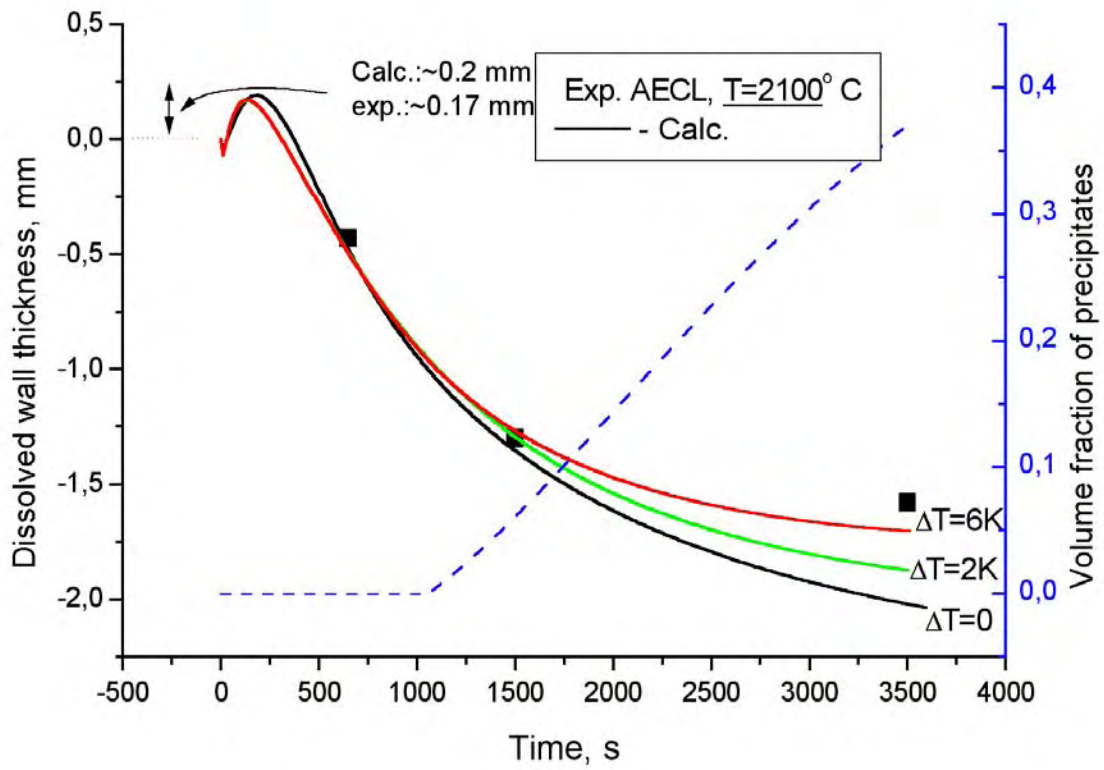
Fig. II-12: Simulations of AECL tests on ZrO$_2$ crucible dissolution by molten Zry at melt temperature 2373 K

solid curves – dissolved wall thickness;
*dashed curve* – volume fraction of precipitates (ΔT=6K).
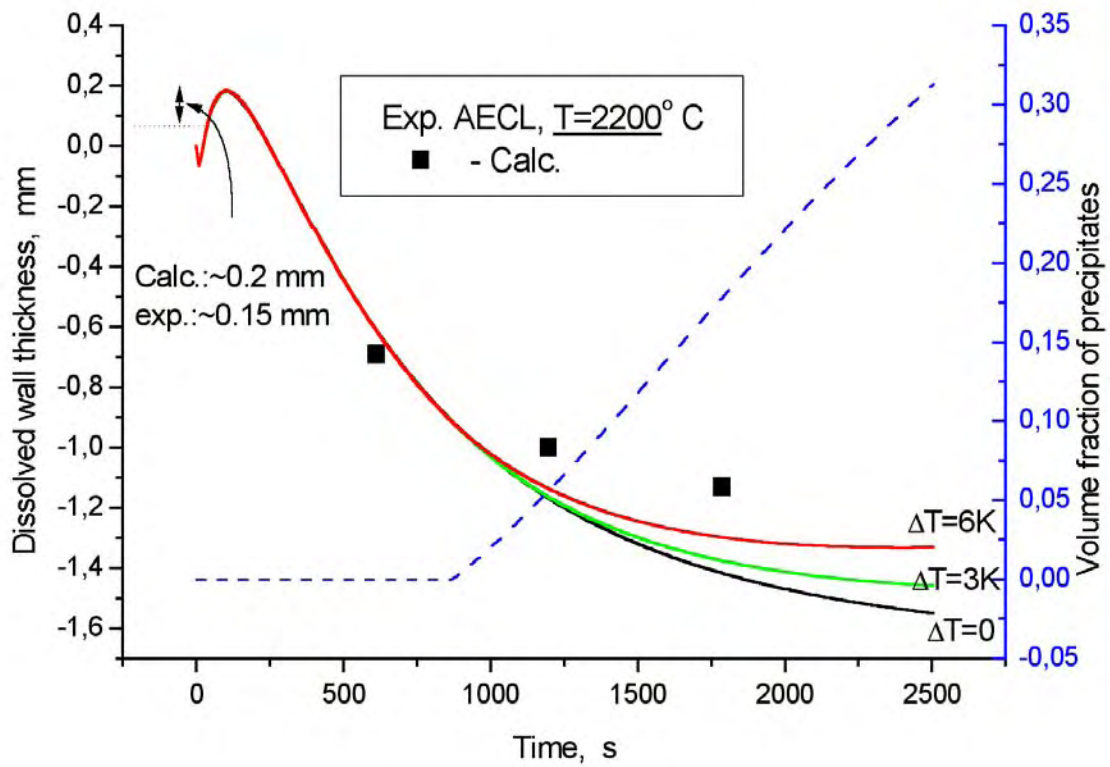
Fig. II-13: Simulations of AECL tests on ZrO$_2$ crucible dissolution by molten Zry at melt temperature 2473 K

solid curves – dissolved wall thickness;
dashed curve – volume fraction of precipitates (ΔT=6K)..
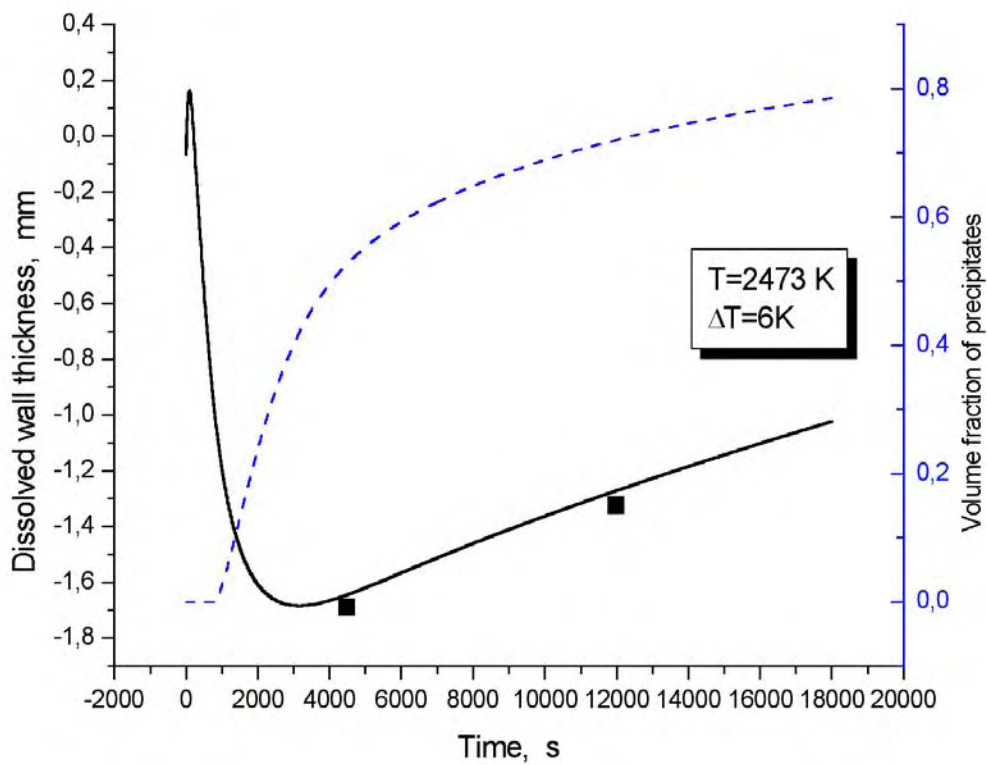
Fig. II-14: Simulations of FZK tests FA11 and FA12 on ZrO₂ crucible dissolution by molten Zry at melt temperature 2473 K

solid curves – dissolved wall thickness;
dashed curve – volume fraction of precipitates.
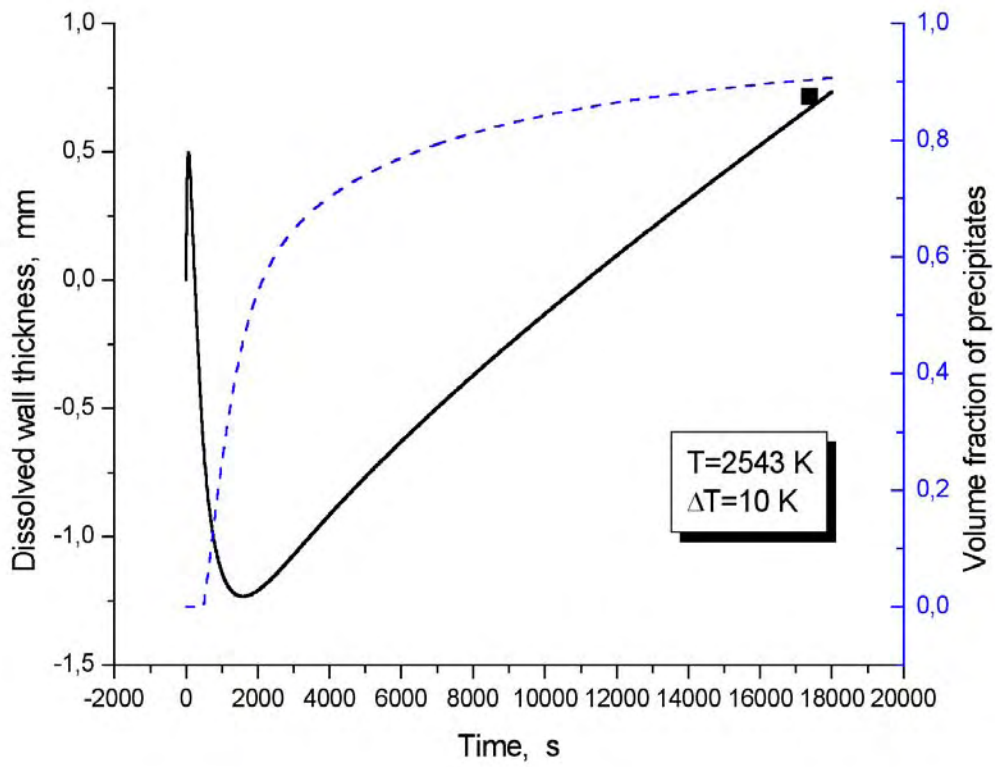
Fig. II-15: Simulations of FZK test FA10 on ZrO₂ crucible dissolution by molten Zry at melt temperature 2543 K

solid curves – dissolved wall thickness;
dashed curve – volume fraction of precipitates.
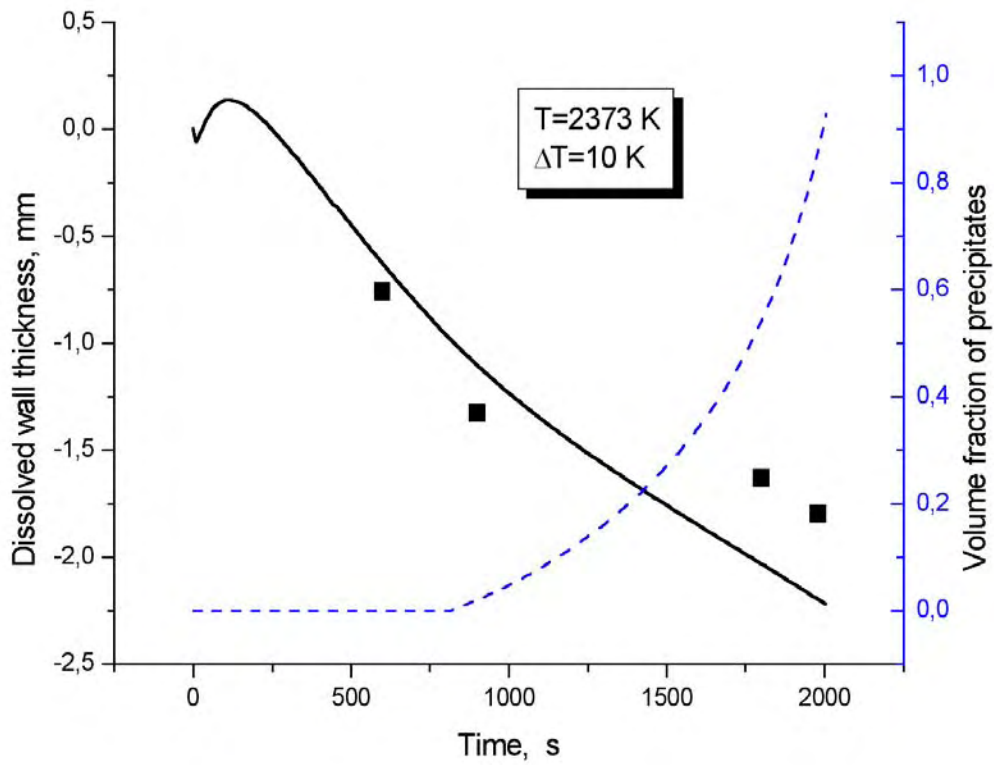
Fig. II-16: Simulations of FZK tests FA1, FA2, FA7 and FA8 on ZrO$_2$ crucible dissolution by molten Zry at melt temperature 2373 K

solid curves   – dissolved wall thickness;
dashed curve – volume fraction of precipitates.
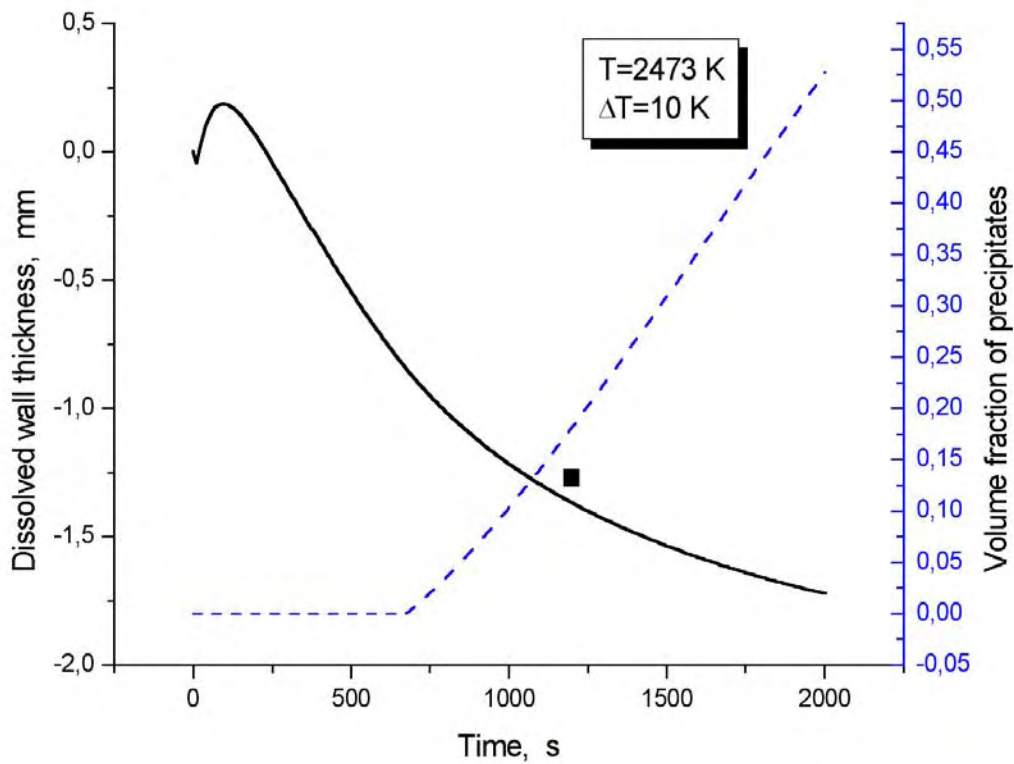
Fig. II-17: Simulations of FZK test FA3 on ZrO₂ crucible dissolution by molten Zry at melt temperature 2473 K

solid curves – dissolved wall thickness;
dashed curve – volume fraction of precipitates.
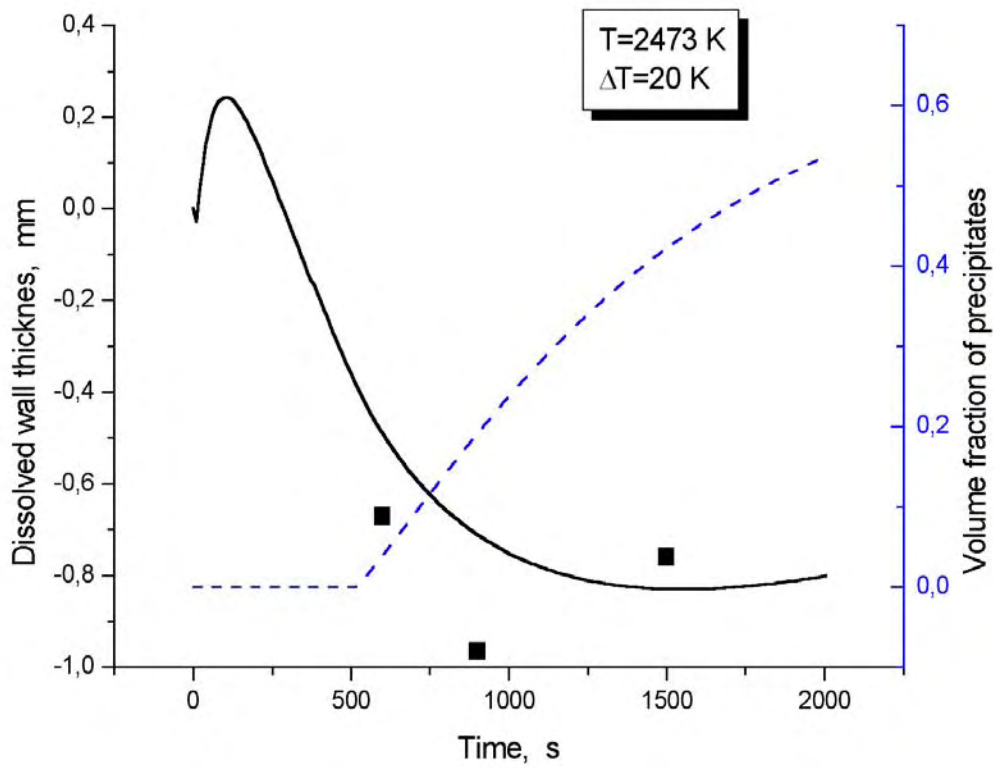
Fig. II-18: Simulations of FZK tests FA5, FA6 and FA9 on ZrO$_2$ crucible dissolution by molten Zry at melt temperature 2473 K

solid curves – dissolved wall thickness;
dashed curve – volume fraction of precipitates.
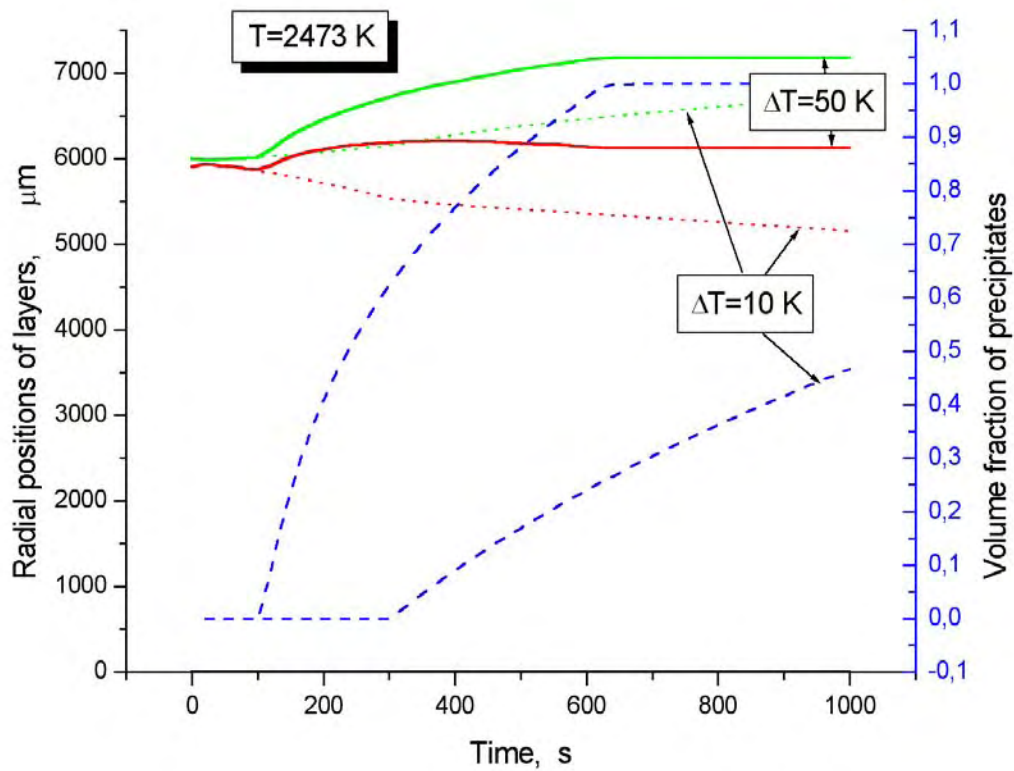
Fig. II-19: Simulation of Zr melt oxidation at melt temperature 2473 K and two values of temperature drop in the transition boundary layer ΔT = 10 K and 50 K for cylindrical molten pool with *R* = 6 μm

solid and dotted curves – radial positions of oxide layer boundaries;
dashed curves – volume fraction of precipitates.
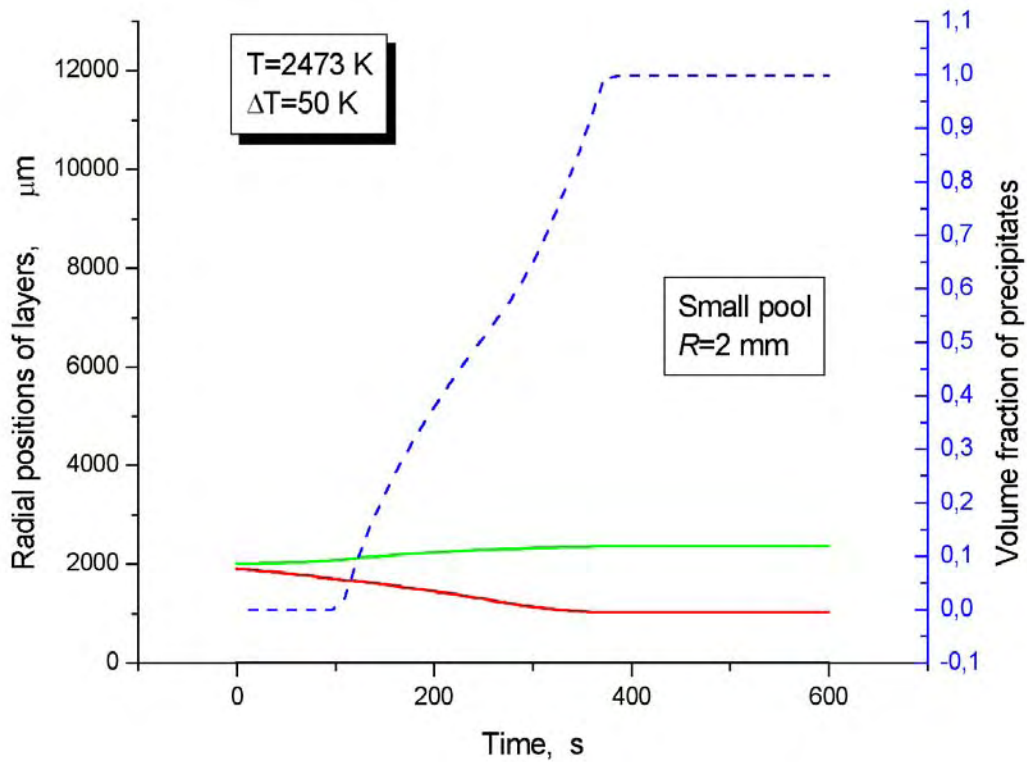
Fig. II-20: Simulation of Zr melt oxidation at melt temperature 2473 K and temperature drop in the transition boundary layer ΔT = 50 K for small cylindrical molten pool with R = 2 μm

solid curves – radial positions of oxide layer boundaries;
dashed curve – volume fraction of precipitates.
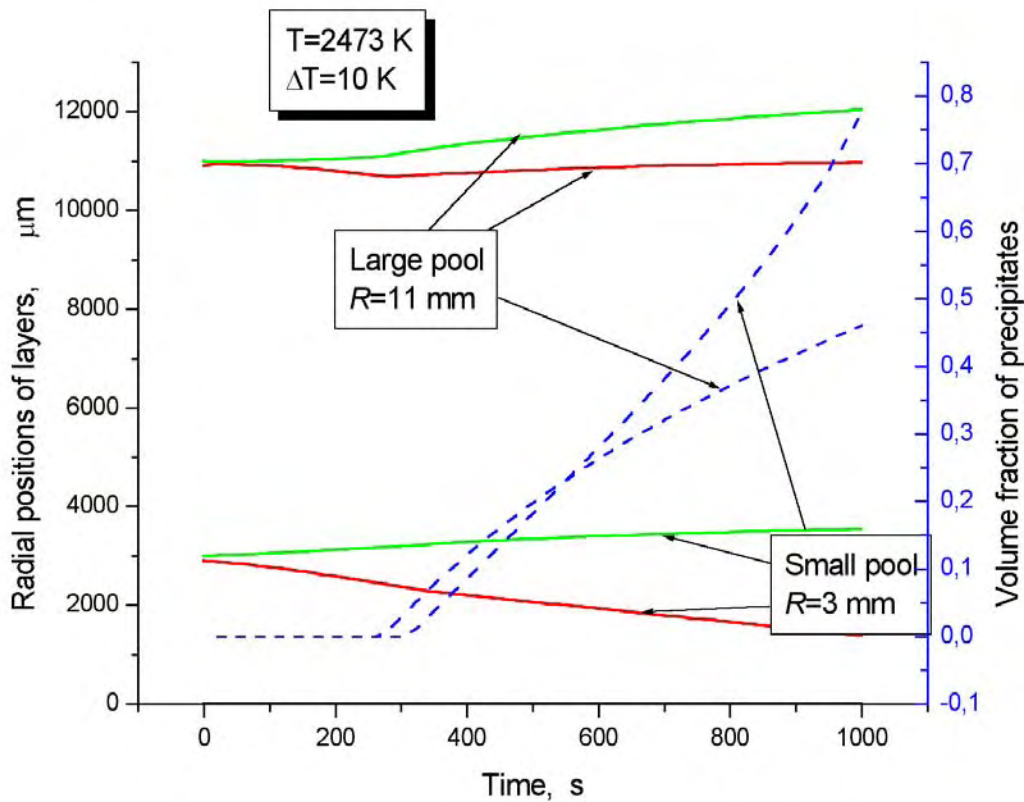
Fig. II-21: Simulation of Zr melt oxidation at melt temperature 2473 K and temperature drop in the transition boundary layer ΔT = 10 K for two cylindrical molten pool with *R* = 3 μm and 11 μm

solid curves – radial positions of oxide layer boundaries;
dashed curve – volume fraction of precipitates.
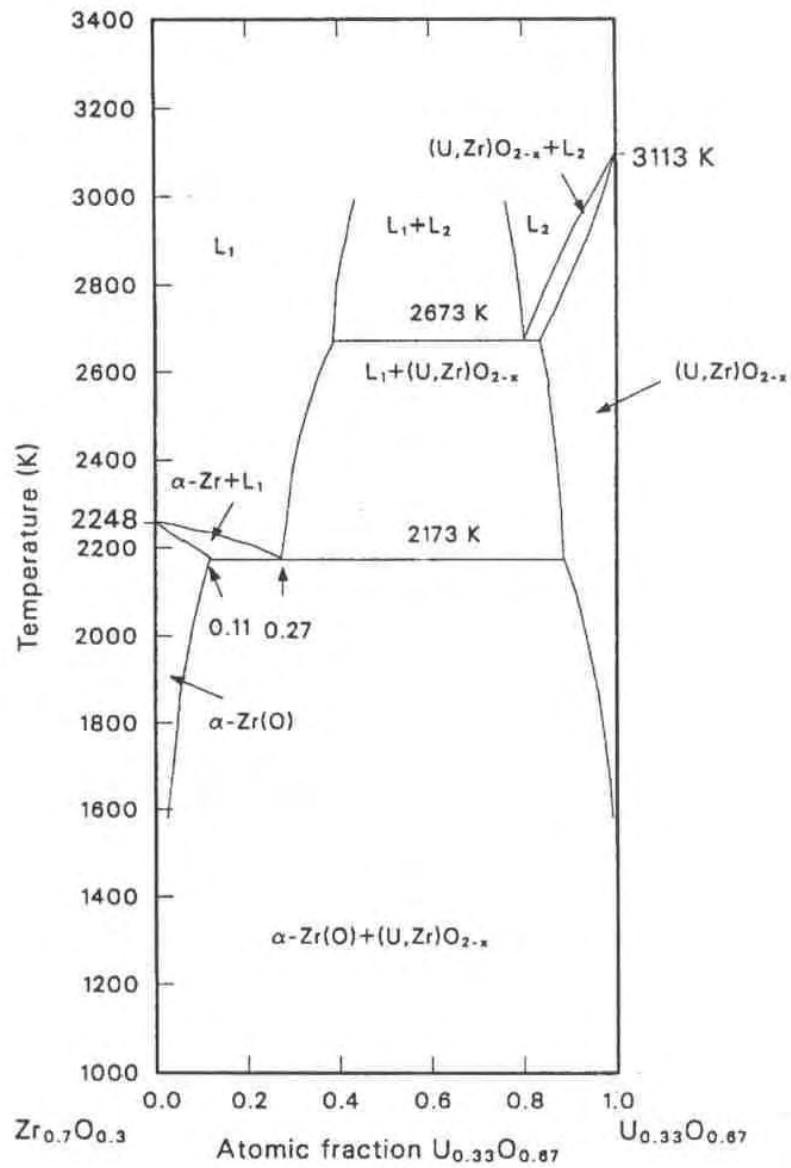
Fig. II-22: Quasi-binary U-Zr-O phase diagram

84
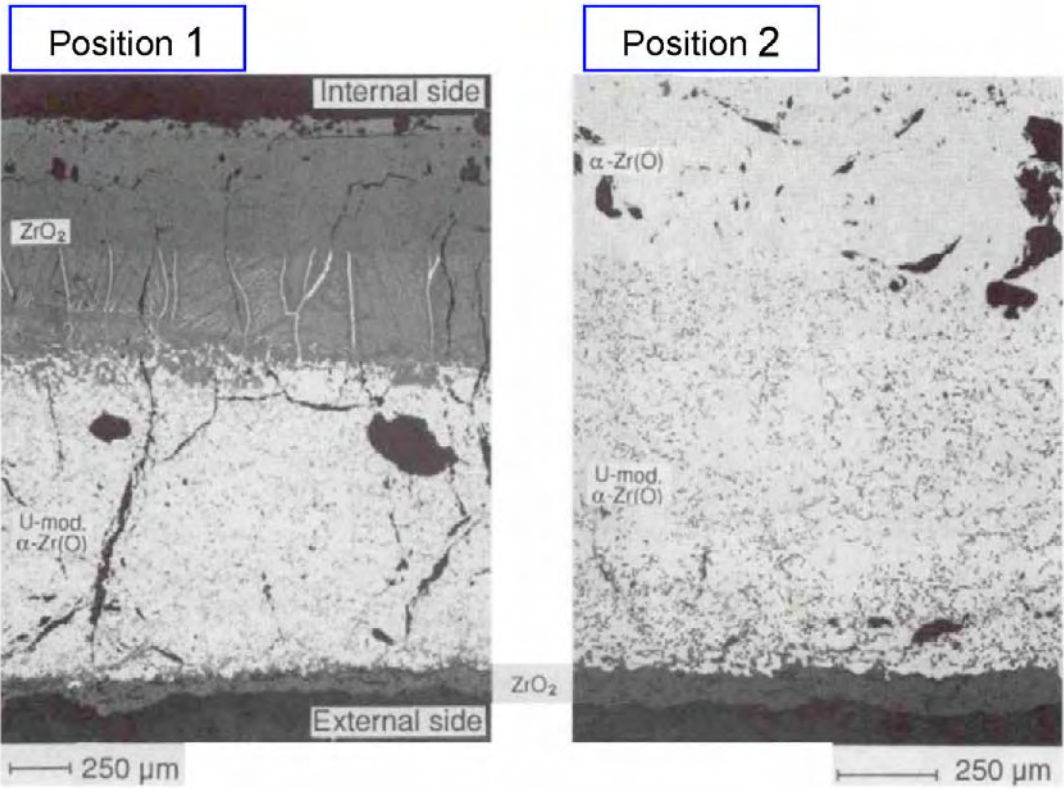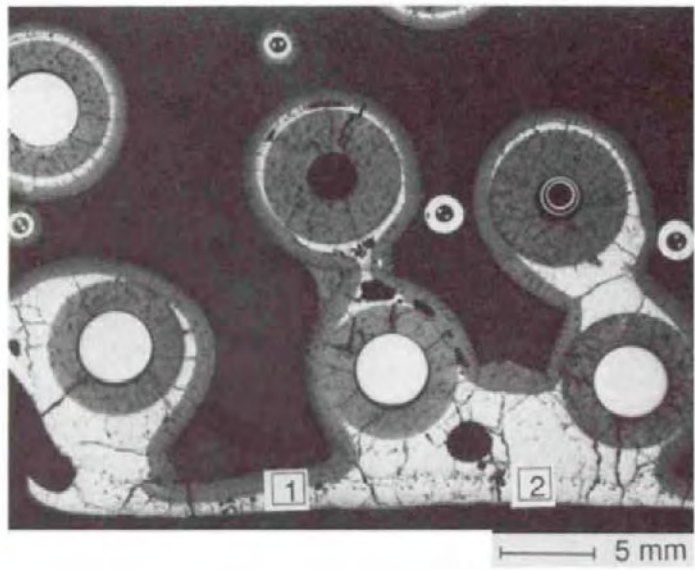
**Fig. II-23: Cross section W1-10 of CORA-W1 test bundle
(elevation 374 mm)**
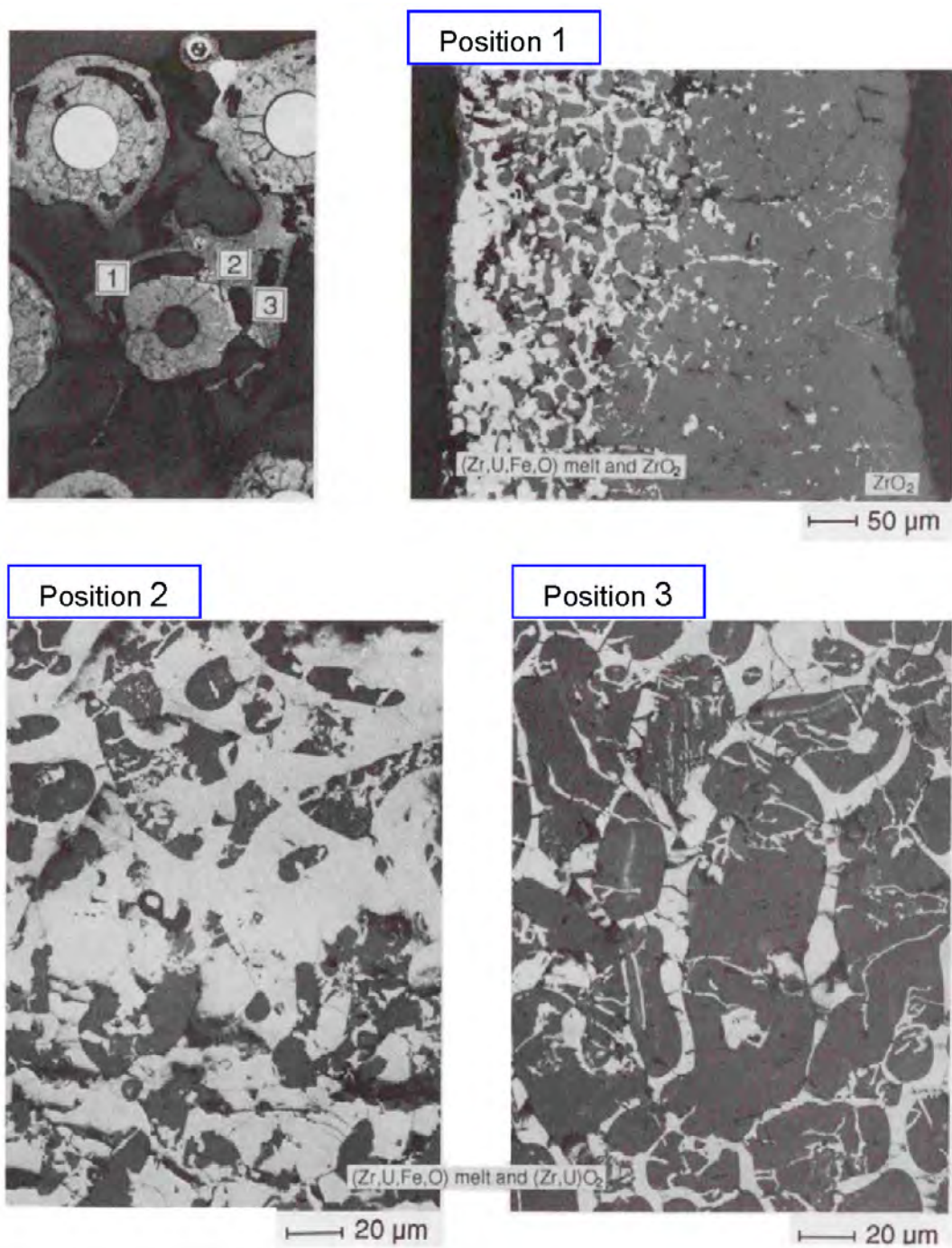
**Fig. II-24: Cross section W2-k of CORA-W2 test bundle
(elevation 605 mm)**
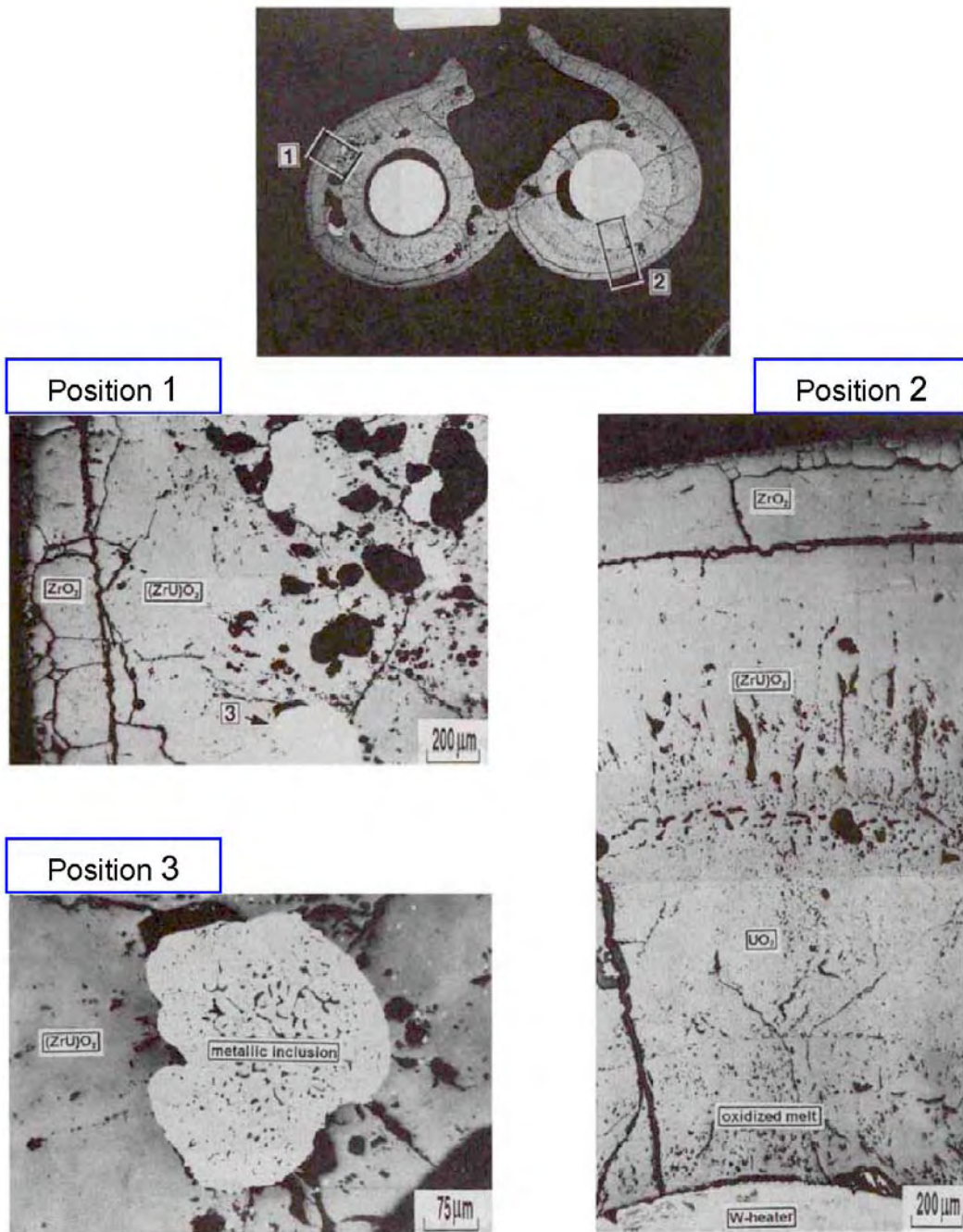
**Fig. II-25: Cross section W2-07 of CORA-W2 test bundle
(elevation 845 mm)**
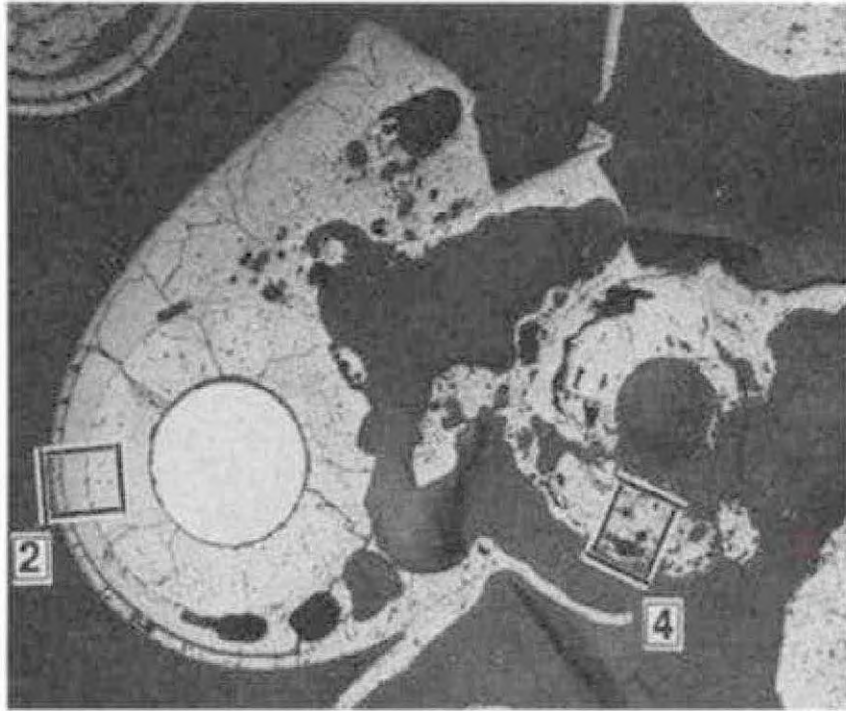
Position 2
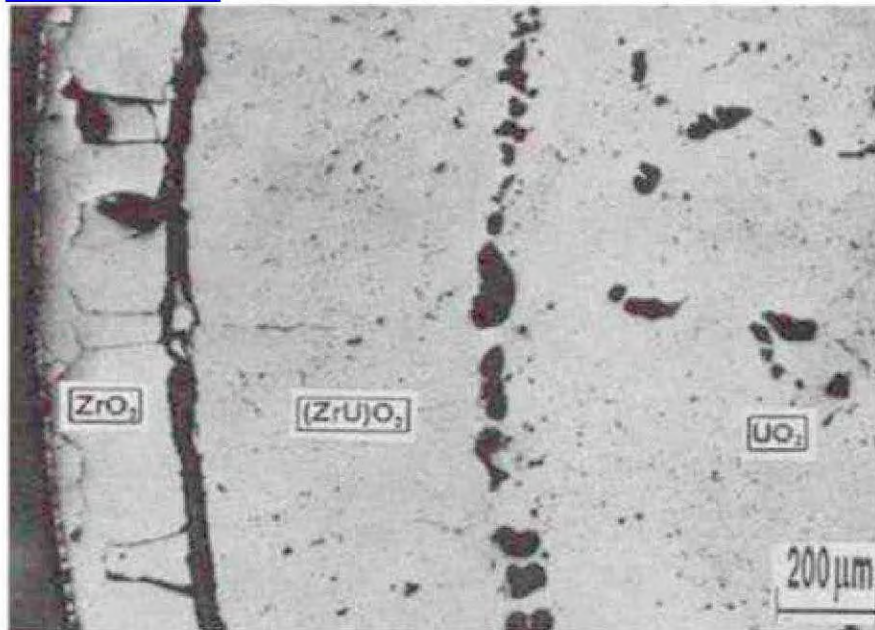
Fig. II-26: Cross section W2-03 of CORA-W2 test bundle
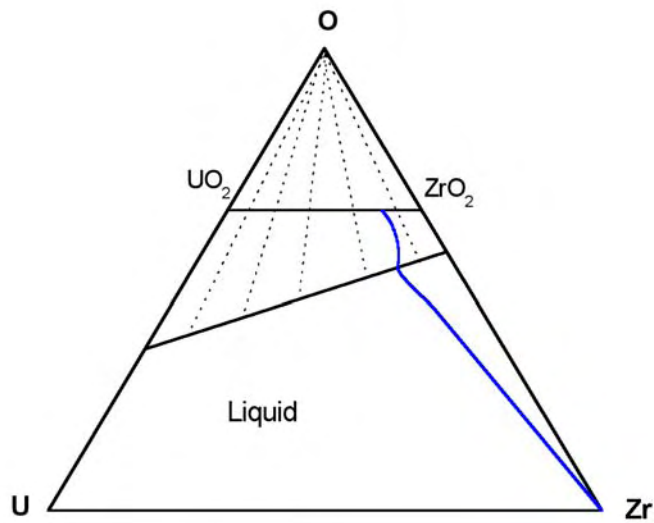**(elevation 950 mm)**

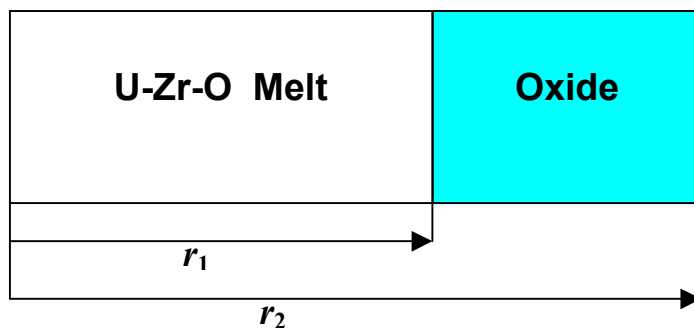**Fig. II-27: Schematic representation of the ternary U-Zr-O phase diagram with equilibrium tie-lines (*dotted lines*)**

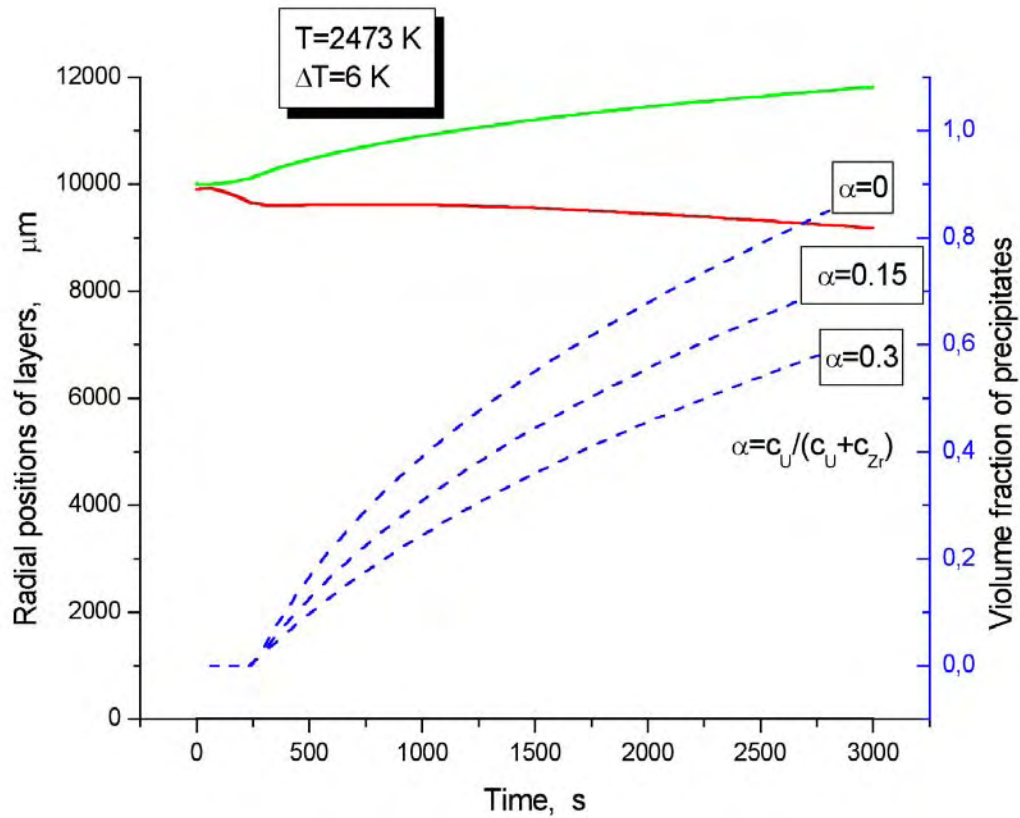**Fig. II-28: Schematic representation of the cylindrical model geometry**

Fig. II-29: Simulation of oxidation of U-Zr melt with three various compositions $\alpha = c_U/(c_U+c_{Zr})$ at melt temperature 2473 K and temperature drop in the transition boundary layer $\Delta T = 6$ K for large cylindrical molten pool with $R = 10\ \mu m$

solid curves   – radial positions of oxide layer boundaries;
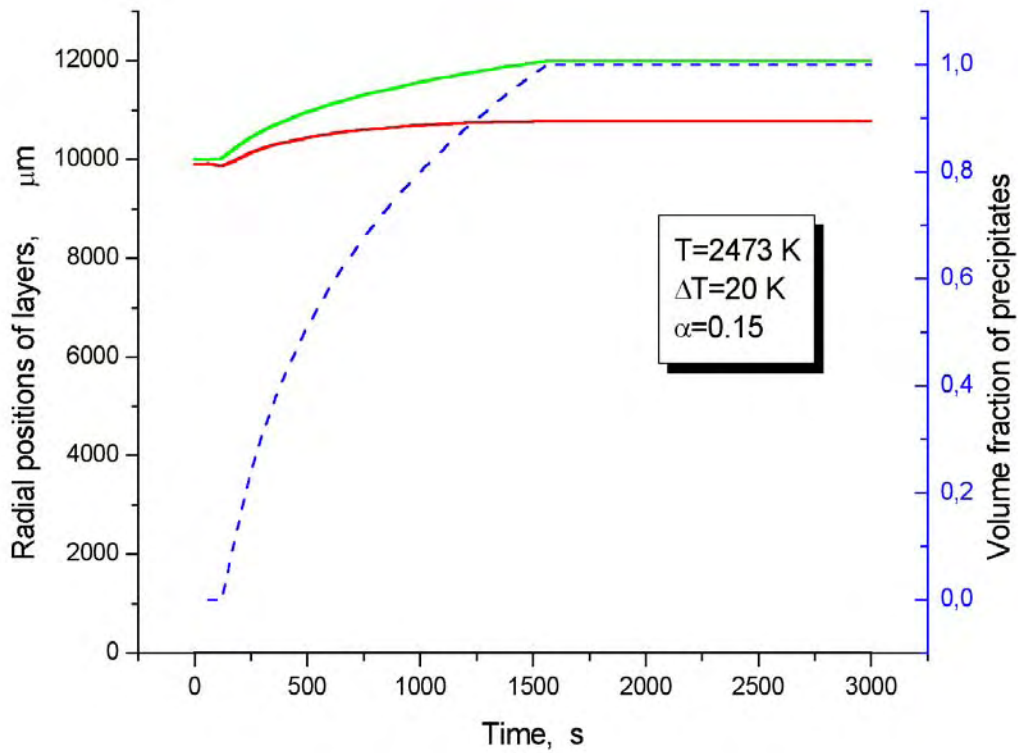dashed curve – volume fraction of precipitates.

Fig. II-30: Simulation of oxidation of U-Zr melt with composition
$\alpha = c_U/(c_U+c_{Zr}) = 0.15$ **at melt temperature 2473 K and temperature drop in the transition boundary layer** $\Delta T = 20$ K **for large cylindrical molten pool with** $R = 10\ \mu m$

solid curves   – radial positions of oxide layer boundaries;
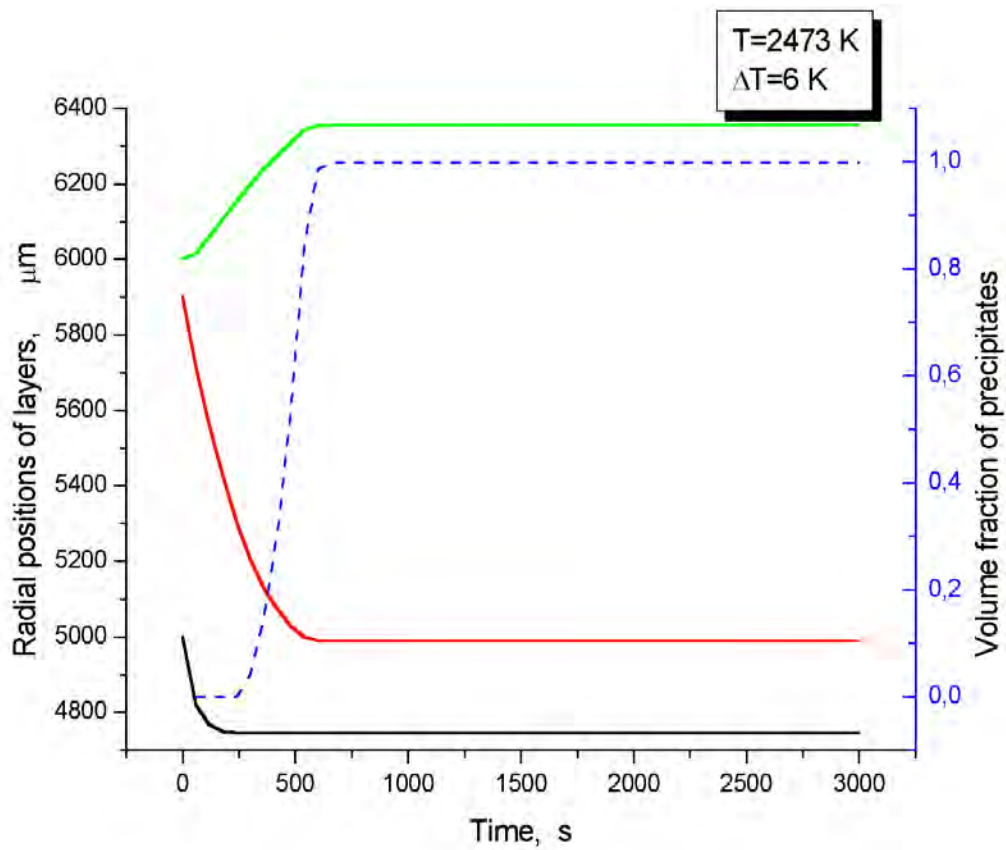*dashed curve* – volume fraction of precipitates.

Fig. II-31: Simulation of molten Zr cladding oxidation at melt temperature 2473 K and temperature drop in the transition boundary layer $\Delta T = 6$ K, with account for UO$_2$ pellet dissolution

solid curves – radial positions of ZrO$_2$ and UO$_2$ boundaries;
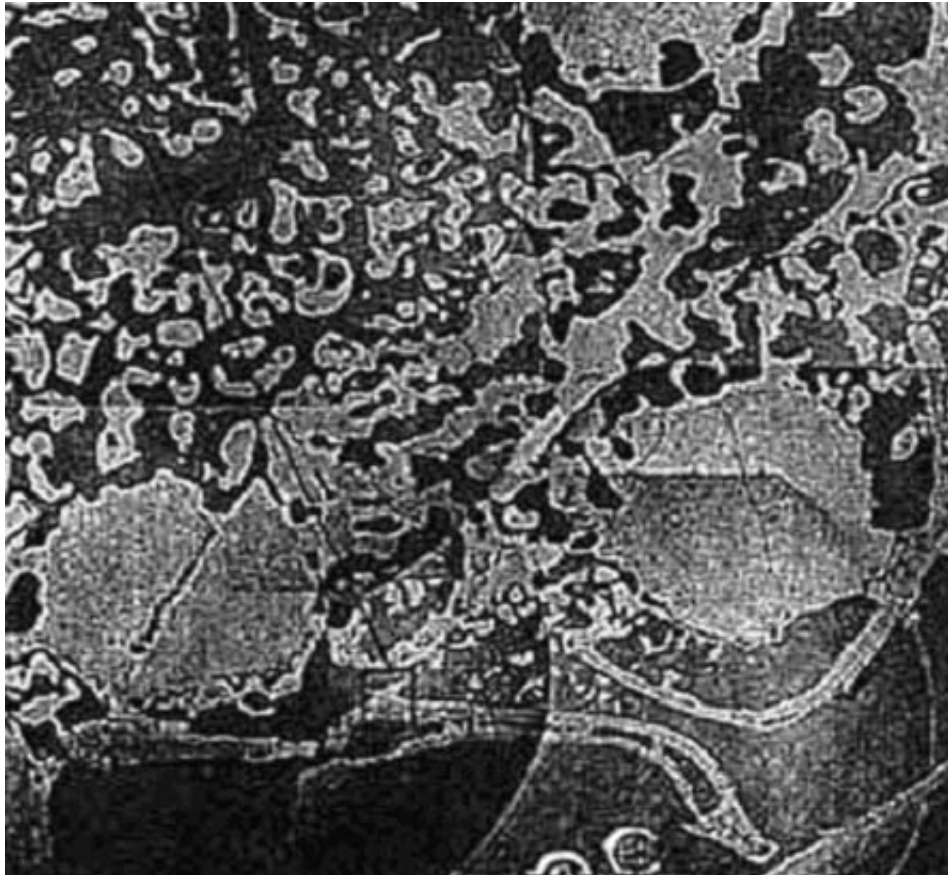*dashed curve* – volume fraction of precipitates.

Fig. II-32: Micrograph of Phebus FPT0 cross section at level +940 mm